

STRUCTURE PROPERTY RELATIONS IN FERROELECTRIC MATERIALS

BY

DAVID MICHAEL FANNING

B.S., Massachusetts Institute of Technology, 1993
M.S., University of Illinois at Urbana-Champaign, 1995

THESIS

Submitted in partial fulfillment of the requirements
for the degree of Doctor of Philosophy in Physics
in the Graduate College of the
University of Illinois at Urbana-Champaign, 2000

Urbana, Illinois

STRUCTURE PROPERTY RELATIONS IN FERROELECTRIC MATERIALS

David M. Fanning, Ph.D.
Department of Physics
University of Illinois at Urbana-Champaign, 2000
Ian K. Robinson, Advisor

A series of experiments using synchrotron x-ray radiation to study ferroelectrics are performed. Primarily, the ferroelectric relaxor lead magnesium niobate, $\text{Pb}(\text{Mg}_{1/3}\text{Nb}_{2/3})\text{O}_3$, and related systems are investigated. PMN is an important ferroelectric with a maximum dielectric constant of 30,000 and a broad dielectric transition near room temperature. Diffraction experiments reveal domains of chemical ordering of the Mg and Nb cations. These ordered domains are limited to about 50 Å in size and result in broad and weak superstructure reflections. Crystallographic measurements of superstructure peaks are used to find the structure of the ordered domains.

By doping PMN with lanthanum (La-PMN) to replace the lead, the ordered domain size is increased: up to 900 Å for 10% La content. Again, the structure of the ordered domains is studied and the chemical ordering is seen to change from complete chemical ordering between the Nb and Mg ions (space charge model) to chemical ordering between Nb and $(\text{Mg}_{2/3}\text{Nb}_{1/3})$ --random layer model. While some of the increase in ordered domain size may be due to the additional charge provided by La^{3+} , an alternative explanation based on internal strain arguments is provided.

The effect of the ordered domain size together with dielectric measurements are described in order to better understand the relaxor behavior. The relaxor behavior can be understood in terms of the interference of the chemically ordered domains with the ferroelectric polar domains. As the chemically ordered domain size increases, the La-PMN crystals become more relaxor like. Doping with titanium (PMN-PT) on the Mg/Nb

site leads to decreasing ordered domain size and an increase of the ferroelectrically active polar domains. Further evidence of the importance of strain to the degree of chemical ordering is provided by growing thin films of PMN on a substrate with a smaller lattice constant (SrRuO_3). The mismatch in lattice constant produces a compressive strain on the films and the degree of ordering is seen to increase compared to bulk PMN.

A diffraction anomalous fine structure (DAFS) experiment is also performed on PMN to independently confirm the structure found using crystallography. By sitting at a superstructure reflection, only the signal coming from the chemically ordered domains is collected, so the bond lengths from within the ordered domains can be determined.

Finally, experiments on thin films of anti-ferroelectric lead zirconate, PbZrO_3 , are performed. PZ undergoes a phase transition from anti-ferroelectric to paraelectric cubic at 230°C . The effect of the thin film PZ samples is to change its phase transition from first to higher order, as measured by the intensity of the superstructure peaks and the orthorhombic order parameter.

Acknowledgments

Foremost, I would like to thank my advisor, Prof. Ian Robinson. He has provided excellent guidance in my work while allowing me freedom to work on what I was interested in. He has been an excellent mentor and very supportive throughout. I will always be impressed by his vast and quick intellect, ability to manage several projects at once and his willingness to participate in all aspects of an experiment.

I have also received a great deal of support and been fortunate to work with Prof. David Payne. I have learned a lot from him and have also benefited from his suggestions for experiments and by participating in his electrical ceramics group meetings. Material support was also provided in the form of samples and access to his laboratories for crystal growth and dielectric measurements without which these experiments would not have been possible. I would also like to thank Prof. Dwight Viehland for suggesting the initial experiment on lead magnesium niobate and providing the crystals.

I have had the privilege of working with and learning from a number of visiting scientists and fellow graduate students from Prof. Payne and Viehland's research groups. Dr. Suntae Jung worked very closely with me on the growth of lanthanum doped PMN single crystals. Dr. Eugene Colla was instrumental in the dielectric measurements on those crystals. Xinliang Lu was very willing to help in the growth and dielectric measurements of the lead zinc niobate crystals. Many helpful discussions with these scientists as well as

Dr. Surya Gupta, Dr. Zhengkui Xu and Tan Qi increased my understanding of ferroelectrics and were helpful in planning the experiments.

At the National Synchrotron Light Source, Dr. Anatoly Frenkel has been a good friend and willing collaborator on the diffraction anomalous fine structure experiments, which were begun with the aid of Dr. David Adler. With the help of Bill Lehnert, they have also ensured that beamline X16C was always operating smoothly.

Support and encouragement in many forms also came from the other members of Prof. Robinson's group. Kevin Whiteaker, Yong Chu, Chinkyoo Kim, Don Walko, John Pitney, Jeff Libbert and Odile Robach have all been good friends and eager to lend a helping hand or brain when needed.

I would also like to thank my loving parents, John and Margaret Fanning, who in addition to their support and encouragement, instilled in me the value of education and provided me with a great one.

Finally, I would like to thank my wife, Cindy Castañeda, whose love, support and encouragement are without bounds. She has always been there for me through good times and bad and with her in my life, it's almost all good!

This work was supported by DOE under DEFG02-96ER45439 MRL. The data were taken at the National Synchrotron Light Source, supported by DOE under DEAC02-98CH10886 NSLS.

Table of Contents

Chapter

1	Introduction	1
2	X-ray Diffraction	7
2.1	Introduction	7
2.2	Overview	8
2.3	Size effect and mosaic	14
2.4	Experimental details	16
2.5	Resonant scattering	21
2.6	References	27
3	Ferroelectrics	28
3.1	Definition and properties	28
3.2	Perovskite structure	31
3.3	Normal and relaxor ferroelectrics	33
3.4	Relaxor theories	36
3.5	Thin films	38
3.6	References	41

4	Lead Magnesium Niobate	43
4.1	Introduction	43
4.2	Literature review	44
4.2.1	Chemical ordering--space charge	46
4.2.2	Chemical ordering--random layer.....	48
4.3	Crystal growth	50
4.4	Lanthanum doped PMN	53
4.4.1	Measurements	53
4.4.2	Analysis	58
4.4.3	Results	61
4.4.4	Charge imbalance models.....	66
4.4.5	Strain effect	69
4.5	Titanium doped PMN.....	73
4.6	Lead zinc niobate	75
4.7	Conclusion	78
4.8	References	79
5	PMN Thin Films	81
5.1	Introduction	81
5.2	Film growth	83
5.3	X-ray measurements	85
5.4	Results	87
5.5	Discussion	92

5.6	Conclusion	93
5.7	References	94
6	X-ray Resonance	95
6.1	Diffraction anomalous fine structure	95
6.1.1	Background	95
6.1.2	EXAFS on PMN	98
6.1.3	DAFS experiment	98
6.1.4	Data retrieval	102
6.1.5	EXAFS/DAFS analysis	104
6.2	Resonant scattering	106
6.2.1	Background	106
6.2.2	Space charge vs. random layer	109
6.2.3	Data collection	111
6.2.4	Results	116
6.3	References	118
7	Lead Zirconate Thin Films.....	119
7.1	Introduction	119
7.2	Lead zirconate background	122
7.3	Growth	124
7.4	Dielectric and polarization measurements	127
7.5	X-ray measurements	130
7.6	Temperature measurements	135

7.7	Electric field	140
7.8	Conclusion	140
7.9	References	141
	Curriculum Vitae.....	143

List of Tables

4.1	Summary of domain size and dielectric constant data measured for the samples with different La^{3+} doping concentrations	56
4.2	Ionic radii from Shannon	69
4.3	R_B is the measured ionic radius that would fit in the B' site	72
5.1	Measured lattice constants of each film	89
5.2	Bulk and ordered domain size of each film.....	91

List of Figures

2.1	Incoming, k_i , and outgoing, k_f , wavevectors define the scattering plane.....	10
2.2	Consider a photon scattering from one unit cell which has its origin at R_n and N_c atoms located at positions r_j within the unit cell.....	12
2.3	Schematic of a single crystal that is broken up into two mosaic blocks at a small angle to one another	17
2.4	Diagram of the Kappa geometry diffractometer.....	18
2.5	Atomic form factors, f_0 , for Nb and Mg.....	22
2.6	Anomalous scattering factors, $f'(E)$ and $f''(E)$, for Mg	23
2.7	Cross sections of the copper atom interacting with photons	24
3.1	Typical hysteretic behavior of ferroelectrics	29
3.2	Perovskite ABO_3 structure with the A and B cations on the corner and body center positions, respectively	32
3.3	Dielectric constant of barium titanate vs. temperature.....	33
3.4	Dielectric constant (left) and dielectric loss (right) of the relaxor lead magnesium niobate as a function of temperature	34
3.5	Phase diagram of the lead zirconate--lead titanate system.....	40
3.6	Dielectric constant (solid) and dielectric loss (circles) of bulk lead zirconate	

	on heating and cooling cycles	41
4.1	Two adjacent unit cells of PMN showing the 1:1 chemical ordering as in the space charge model	47
4.2	Powder x-ray diffraction scan of intensity vs. 2θ for pure PMN with the perovskite structure	52
4.3	Raw x-ray diffraction data showing the intensities of four adjacent superstructure peaks	55
4.4	Dielectric constant, ϵ' , and loss, ϵ'' , measured on the 3% and 10% La-PMN crystals as a function of temperature	57
4.5	Structure factors (after corrections) vs. momentum transfer for superstructure reflections of pure PMN.....	61
4.6	Improved fit using the $R\bar{3}m$ model and an oxygen displacement of 0.044 Å	63
4.7	Oxygen displacement and lattice constant as a function of La doping	64
4.8	Calculated bond lengths of B'-O and B''-O as a function of La doping.....	71
4.9	Dielectric behavior of PMN-PT for increasing amounts of lead titanate.....	74
4.10	Dielectric constant behavior of PZN and 10% La-PZN	75
5.1	Dielectric properties of the 1500 Å PMN thin film	84
5.2	Scan through the (111) peak of the PMN thin film in the $\langle 111 \rangle$ direction clearly shows the single crystalline MgO substrate and the SrRuO ₃ intermediate layer	85
5.3	Mosaic broadening	88

5.4	The (101) type peaks show mosaic broadening when measured in the transverse<010> direction but not in the radial <101> direction	89
5.5	Enhanced chemical ordering in the films led to superstructure peaks with widths almost as narrow as the bulk peaks in all films grown on the MgO/SrRuO ₃ substrate	91
6.1	The EXAFS signal oscillates about the smooth absorption cross-section background of the bare atom	96
6.2	Normalized DAFS signal (dashed) after correcting for absorption and fluorescence, and a smooth background (solid) from equation 9	103
6.3	Resulting $f'(E)$ and $f''(E)$ by iterative fit to Kramers-Kronig.....	103
6.4	Fit of equation 9 using FEFF6 theory (dash) to the data (solid) in a) k -space and b) r -space	105
6.5	Anomalous scattering factors, $f'(E)$ and $f''(E)$, for Nb	108
6.6	Scan through the (111) peak ON and OFF resonance	112
6.7	Data collection procedure for resonant scattering measurements	115
6.8	Resonant fraction measured at different points near the (001) Bragg peak..	117
6.9	Resonant fraction measured at different points near the (101) Bragg peak..	117
7.1	Scott et al found that in thin film form, ferroelectrics can have their phase transition behavior modified	121
7.2	Lead zirconate structure	123
7.3	Procedure for depositing thin films via the chemical solution deposition, or sol-gel, method	125
7.4	The substrates were platinized Si wafers	126

7.5	Polarization vs. electric field for preferred (100) and (111) thin films.....	128
7.6	Dielectric constant behavior for the (111) and (100) lead zirconate films....	129
7.7	The superstructure diffraction peaks are shown as dots with radii proportional to magnitude	131
7.8	Raw data of the (200) peak scanned in the h direction showing the tetragonal splitting caused by the shorter c -axis lattice constant (right peak).....	134
7.9	Integrated intensity of the (0.25, 0.75, 1) superstructure peak vs. temperature.....	136
7.10	Dependence of a and c lattice constants vs. temperature for the (100) type lead zirconate films.....	137
7.11	Dependence of a and c lattice constants vs. temperature for the (111) type lead zirconate films compared to bulk.....	138
7.12	Tetragonal splitting in the (111) film vs. temperature fit to a power law	139

Chapter 1

Introduction

In this thesis, x-ray diffraction is used to study ferroelectric materials. Although x-ray diffraction has been practiced for almost 90 years, it is still a valuable and versatile tool. Its original purpose of crystallography, or determining the atomic structure of solids, is a well developed science that is continually being used to solve larger and more complicated structures in a variety of fields. In solid state physics it is important to know the structure of new materials. In addition, x-ray diffraction can be used to study more subtle features of crystals such as small domains within a crystal, microstructural features, structural phase transitions and the properties of thin films. Understanding the relationship between structure and properties can lead to both physical insight and enhanced material properties.

With the advent of synchrotron sources, very intense x-ray beams can be produced. Synchrotron sources accelerate charged particles in a ring, providing x-ray beams to many experimental stations. The increased intensity has led to entirely new areas of investigation in addition to decreasing the time needed for standard x-ray diffraction experiments. For example, the scattering from a single atomic layer can now be easily observed with synchrotron radiation. The penetration of x-rays through thin films also allows the surface of a film and its interface with a substrate to be studied simultaneously.

An important advantage of x-ray diffraction is that it requires no special sample preparation and in most cases has no effect on the material under investigation. Hence, *in situ* experiments can be performed to study phase transitions or thin film growth processes.

Other x-ray measurements have been recently developed including the extended x-ray absorption fine structure (EXAFS) technique. EXAFS relies upon the ability of synchrotron sources to finely tune the incoming photon's energy. By scanning energy near an atomic excitation level, photoelectrons are ejected, and they interfere with neighboring atoms. The resulting interference pattern can be used to determine the neighboring atom's precise positions. A similar technique, diffraction anomalous fine structure (DAFS), combines EXAFS with x-ray diffraction to study specific regions within a larger crystal. While x-ray diffraction is a long range order technique, EXAFS and DAFS are short range order techniques, so the two complement each other. Since x-ray diffraction requires long range order, its response is related to the average crystal structure.

The interpretation of x-ray diffraction data is straightforward and does not rely on complicated analysis procedures. As described in Chapter 2, the diffraction pattern is a Fourier transform of the crystal's electronic density. A derivation of the scattering of x-rays by crystals is given as well as the techniques that are used to determine crystal structures based on intensity data. Other experimental details such as finite size effect, mosaic spread and resonant scattering are discussed. In addition, details about the experimental set up including the x-ray beamline, diffractometer and measurement techniques are described.

The goal in using x-ray diffraction to study crystal structure is not simply to measure the precise atomic positions of a variety of samples. Rather, crystal structures are

determined in order to better understand the material's properties. These structure property relationships can lend insight into a material's behavior and help one to understand what features of a crystal can be changed to enhance a particular parameter. For example, ferroelectrics are materials that can have a net spontaneous electrical polarization below a critical, or Curie, temperature. The polarization results from the lining up of electric dipoles created by displacements of ions within each unit cell. By measuring these atomic displacements, the ferroelectric behavior can be better understood. Chapter 3 serves as an introduction to ferroelectrics, specifically focusing on the ferroelectrics that are the subject of this thesis. By definition, ferroelectrics can have a net spontaneous polarization, and the polarization direction can be oriented via application of an electric field. This can be seen in the hysteretic behavior of the polarization versus electric field graph. The dipole moments line up with each other in "domains" that range in size from a few unit cells to the entire crystal. An anti-ferroelectric material contains dipole moments that are oppositely oriented in adjoining unit cells. Normal ferroelectrics exhibit sharp increases in their dielectric constant as temperature is varied through a phase transition at the Curie temperature. In contrast, relaxor ferroelectrics have a very gradual transition and usually have much higher dielectric constants. Ferroelectrics also commonly have a large piezoelectric effect, which is the strain produced in response to an applied external electric field. Both normal and relaxor ferroelectrics are used in many applications that take advantage of these phenomena.

Chapter 4 contains the main crystallographic results of this work and is mostly concerned with the relaxor ferroelectric lead magnesium niobate or PMN. PMN has the chemical formula $\text{Pb}(\text{Mg}_{1/3}\text{Nb}_{2/3})\text{O}_3$ and consists of unit cells of Pb atoms on the corners, O atoms on the faces and either a Mg or Nb ion in the body center of each unit cell.

Although there is twice as much Nb as Mg in the entire crystal, limited regions engage in 1:1 chemical ordering on the B-sites of adjacent unit cells. This additional ordering occurs only in very small regions ($\sim 50 \text{ \AA}$) and gives rise to additional “superstructure” peaks in the diffraction pattern. Understanding the cation heterogeneity within PMN and its relation to the ferroelectric response helps understand its behavior and the cause of the relaxor phenomena. Dopants of La on the A-site are seen to increase the ordered domain size while dopants of Ti on the B-site decrease it. The structure of these ordered regions in each crystal is determined via crystallographic analysis. In addition, dielectric measurements record the ferroelectric behavior of the various crystals, and an interpretation of the properties based on the crystal structure is given. In addition, crystals of lead zinc niobate (identical composition to PMN except for Zn replacing Mg) are studied to further develop the analysis.

While ferroelectrics have been researched and used in applications for about 50 years, a rapidly developing new field is thin film ferroelectrics. With a number of advanced deposition techniques developed recently, it is now possible to grow very small ferroelectric devices with material properties that approach their bulk counterparts. These advances have led to ever smaller and more robust applications as well as the incorporation of ferroelectrics as capacitors, sensors and actuators on silicon devices.

The effects of surfaces are investigated in Chapter 5, which looks at thin films of PMN to compare their behavior with the bulk crystals. By growing the films on a substrate with a smaller lattice constant, the effect of compressive strain on the ordering behavior of Mg and Nb was studied. This has important implications in determining the type of chemical ordering that is present in PMN. Using synchrotron radiation, films as small as 50 \AA are easily studied. In addition, structural information as well as interfacial

strain/mismatch are measured. The effect of the substrate causes important changes in the ferroelectric behavior of these films.

In Chapter 6, two techniques are used which rely on resonant scattering. In the first experiment, DAFS is used to measure an important bond length within the very small domains that are embedded in the rest of the crystal. By combining EXAFS with the superstructure diffraction condition, the Nb-O bond length only within the ordered regions is measured. In the second part, the resonant scattering of Nb is used to measure whether its concentration varies in different regions of the crystal. Resonant scattering scans the incoming photon energy through an atomic transition level of one of the atoms in the crystal. By measuring the change in diffracted intensity of different peaks, the amount of Nb that is participating in that diffraction can be estimated.

In Chapter 7, thin films of lead zirconate grown by the chemical solution deposition, or sol-gel, technique are investigated. Lead zirconate is actually an anti-ferroelectric that has an important phase transition at 230° C. It also has an interesting electric field response and both of these parameters were studied in an *in situ* experiment. Lead zirconate is an important material that finds applications ranging from piezoelectric effect to charge storage to actuation. As a parent material of the important actuator lead zirconate titanate, $\text{Pb}(\text{Zr}_x\text{Ti}_{1-x})\text{O}_3$, its behavior can lend insight to that widely studied system as well. One important consequence of the thin films of lead zirconate compared to the bulk was that the phase transition behavior changed from first to higher order. The effect of the substrate on the crystalline quality is also investigated, and the structure of the thin films differs significantly from bulk lead zirconate. The interaction with the substrate leads to the film breaking up into small crystalline grains which are allowed to orient with one degree of freedom. Usual crystallographic techniques can not be used, and intensities

are very weak. Using synchrotron radiation, the diffraction pattern is still observable and some structural information was derived. The change in the films' dielectric properties are interpreted in terms of the different crystalline structure.

Chapter 2

X-ray Diffraction

2.1 Introduction

X-ray diffraction is a non-invasive method for determining many types of structural features in both crystalline and amorphous materials. In the case of single crystals, detailed features of the atomic structure, orientation and domain size can be measured. X-ray diffraction is used in a variety of fields from identifying unknown materials in geology to solving the structures of large proteins in biology. It is a well established technique that has been around for most of this century. Recent advances in sources have opened up entirely new areas of research that previously had been unavailable. Synchrotron sources employ a ring of accelerated charged particles which emit intense x-ray radiation that is focused down beamlines into experimental stations. The National Synchrotron Light Source at Brookhaven National Laboratory can produce beams of x-rays with several orders of magnitude more intensity than conventional anode tube sources.

In the experiments described in this thesis, the increased intensity coming from the synchrotron radiation and the use of single crystals made it possible to study very small domains in lead magnesium niobate, $\text{Pb}(\text{Mg}_{1/3}\text{Nb}_{2/3})\text{O}_3$. Since synchrotron radiation occurs across a broad spectrum of energies, it was also possible to do energy dependent

scattering experiments. In contrast, an anode source gives appreciable intensity only at an energy that corresponds to an atomic level in the anode metal. By tuning the wavelength of the x-rays, experiments that exploit the resonant scattering of atoms within a crystal were also performed on PMN. When measuring thin films, x-ray diffraction gives important information about both the film and the substrate. Properties such as strain and other interfacial effects can be measured. Because of the semi-crystalline nature of the thin films of lead zirconate in this experiment, synchrotron radiation was needed for accurate structural analysis and to even observe some of the diffraction peaks. The intense synchrotron x-ray beams also allow the measurement of very small domains and the structure of films as thin as 50 Å.

2.2 Overview

X-ray diffraction involves scattering of incoming x-rays from planes of atoms within a crystal. X-rays are used to study crystalline structure because their wavelengths (~ 1 Å) tend to be on the same order or smaller as atomic spacings in crystals. To better understand the effect of a crystal on a beam of x-rays, it is helpful to start from the basics of electromagnetic radiation scattering from an atom and build up to scattering from an entire crystal. It is assumed initially that the energy of the x-rays is not near to an electronic level of one of the crystal's atoms. When that is the case, the x-ray beam may be absorbed by the atom with the subsequent ejection of electrons, and this case will be covered in Chapter 6.

Following classical theory, the incoming radiation has an electric field vector that is oscillating rapidly. Electrons within the atoms in the crystal are subjected to this field

and experience a corresponding force and acceleration. This acceleration in turn causes those atoms to radiate both at the same frequency (elastic scattering) and at smaller frequencies (Compton modified scattering). The Compton radiation contributes only a diffuse background which is incoherent and can be ignored here.

Assuming the dipole approximation, the Thomson formula [1] gives the scattered amplitude emitted from a single electron at position r as a function of the incoming amplitude:

$$A_e e^{-ik_f \cdot r} = A_o e^{-ik_i \cdot r} \frac{e^2}{mc^2 R} \quad (1)$$

where A_e and A_o are the emitted and incoming amplitudes, respectively. As is the case for the experiments described here, the assumption of polarization perpendicular to the scattering plane is made so that its effects need not be considered. The emitted and incoming wavenumbers, k_f and k_i , have magnitudes given by 2π over the wavelength and describe the direction of each beam. The electron mass and charge are m and e , speed of light is c , and R is the distance from the scattering electron to the detector. Since the factor e^2/mc^2 is of the order of 10^{-15} meters, scattering becomes appreciable only when many electrons are involved.

The momentum transfer q is defined as the difference between the incoming and outgoing wavevectors (Figure 2.1). Requiring elastic scattering gives $|k_i| = |k_f| = |k|$. By referring to Figure 2.1, one sees that Bragg' s law is obtained:

$$|q| = 2|k| \sin \frac{2\theta}{2} \quad (2)$$

where 2θ is the angle between the incoming and outgoing beams, and is known as the

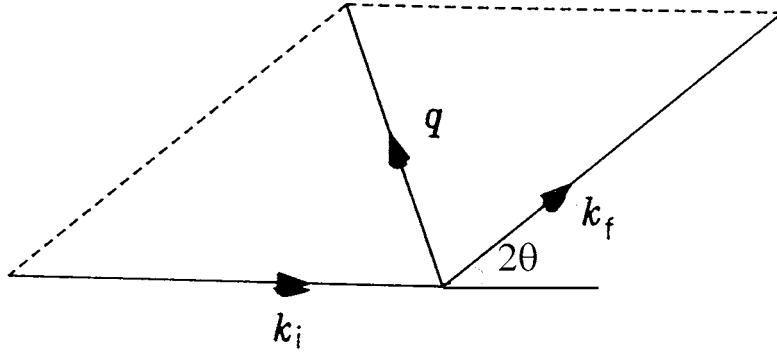


Figure 2.1. Incoming, k_i , and outgoing, k_f , wavevectors define the scattering plane [2]. The momentum transfer, q , is $k_f - k_i$ and 2θ is the Bragg angle.

Bragg angle. Since the momentum transfer q is $k_f - k_i$, equation 1 can be rewritten as:

$$A_e = A_0 \frac{e^2}{mc^2 R} \exp(iq \cdot r_e) \quad (3)$$

In observing this radiation, only the intensity can be measured which is proportional to the square of the amplitude. Using the kinematical approximation, the scattering amplitude from more than one electron can be found by summing the amplitudes of each electron.

Next, the scattering from one atom is considered, following the treatment given by Robinson and Tweet [2]. Because of the strong interaction between the electromagnetic radiation and the electrons, the effect of the atom's nucleus can be disregarded. The scattering from an atom is then simply the sum of the scattering from each electron within

the atom. Consider Z electrons at positions r' around an atom at r . Then the scattered amplitude is:

$$A_{atom} = A_0 \frac{e^2}{mc^2 R} \sum_z \exp[i\mathbf{q} \cdot (\mathbf{r} + \mathbf{r}')] \quad (4)$$

This can be converted to an integral over electronic density, $\psi\psi^* = \rho$:

$$A_{atom} = A_0 \frac{e^2}{mc^2 R} \int \exp[i\mathbf{q} \cdot (\mathbf{r} + \mathbf{r}')] \rho(\mathbf{r}') d^3\mathbf{r}' = A_0 \frac{e^2}{mc^2 R} f(q) e^{i\mathbf{q} \cdot \mathbf{r}} \quad (5)$$

and this expression defines the atomic form factor:

$$f(q) = \int \rho(r') \exp(i\mathbf{q} \cdot \mathbf{r}') d^3r' \quad (6)$$

In practice, atomic form factors are experimentally derived quantities which are either tabulated or fit to polynomials. They are equal to the atomic number when $q = 0$, and generally decrease as q increases. They are independent of the wavelength except near atomic transitions which will be discussed in Chapter 6.

To find the scattering from one unit cell one must sum the scattering from each atom within a unit cell. A unit cell contains all the necessary structural information about a crystal including the number, type and relative position of each atom. The ideal crystal is composed of these space filling unit cells that occupy every point on the crystal lattice. The positions of the unit cells can be described by $\mathbf{R}_n = n_1\mathbf{a}_1 + n_2\mathbf{a}_2 + n_3\mathbf{a}_3$ where the a 's are the crystal axes. Considering just one unit cell at position \mathbf{R}_n which has N_c atoms at positions \mathbf{r}_j within the unit cell (Figure 2.2), the sum of the scattering amplitudes is given by:

$$A = A_0 \frac{e^2}{mc^2} \frac{1}{R_0} \sum_{j=1}^{N_c} f_j(q) \exp(i\mathbf{q} \cdot (\mathbf{R}_n + \mathbf{r}_j)) \quad (7)$$

$$= A_0 \frac{e^2}{mc^2} \frac{1}{R_0} F(q) \exp(i\mathbf{q} \cdot \mathbf{R}_n)$$

which defines the structure factor:

$$F(\mathbf{q}) = \sum_{j=1}^{N_c} f_j(q) \exp(i\mathbf{q} \cdot \mathbf{r}_j) \quad (8)$$

This complex function contains all the structural information about the crystal. One of the objectives of x-ray diffraction is to measure enough structure factors of a crystal to

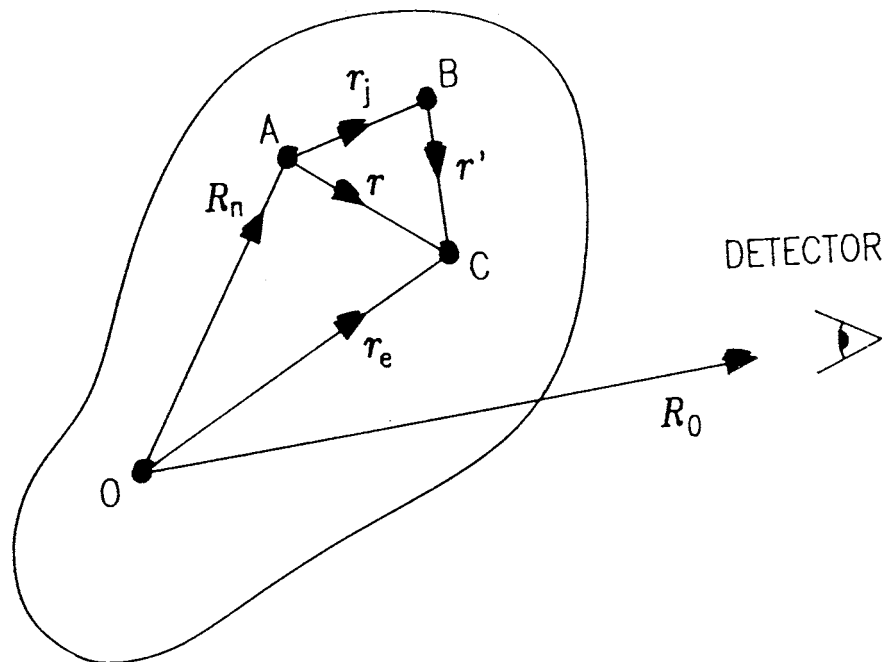


Figure 2.2. Consider a photon scattering from one unit cell which has its origin at \mathbf{R}_n and N_c atoms located at positions \mathbf{r}_j within the unit cell [2]. Detector is much farther than the crystal size at position \mathbf{R}_0 .

determine its structure within a certain allowable error.

The final step in finding the scattered amplitude from a crystal is to sum the previous expression over every unit cell. Consider an atom with $N_1 \times N_2 \times N_3$ unit cells along the crystal axes $\mathbf{a}_1, \mathbf{a}_2, \mathbf{a}_3$. Each unit cell is at a position $\mathbf{R}_n = n_1 \mathbf{a}_1 + n_2 \mathbf{a}_2 + n_3 \mathbf{a}_3$, so the net amplitude is:

$$A_{xtal} = A_0 \frac{e^2}{mc^2} \frac{1}{R_0} F(\mathbf{q}) \sum_{n_1=0}^{N_1} \sum_{n_2=0}^{N_2} \sum_{n_3=0}^{N_3} \exp(i\mathbf{q} \cdot (n_1 \mathbf{a}_1 + n_2 \mathbf{a}_2 + n_3 \mathbf{a}_3)) \quad (9)$$

$F(\mathbf{q})$ can be pulled out of the sum and contains all the structural information. The number of unit cells is typically of the order $N \sim 10^8$, and each sum evaluates to:

$$S_N(\mathbf{q} \cdot \mathbf{a}) = \frac{\exp(i\mathbf{q} \cdot N\mathbf{a}) - 1}{\exp(i\mathbf{q} \cdot \mathbf{a}) - 1} \quad (10)$$

Since squared amplitudes are measured, this expression must be squared to find the diffracted intensity:

$$|S_N(\mathbf{q} \cdot \mathbf{a})|^2 = \frac{\sin^2 N\mathbf{q} \cdot \mathbf{a}/2}{\sin^2 \mathbf{q} \cdot \mathbf{a}/2} \quad (11)$$

which is the well known slit function from optics. Because N is so large, the slit function is very sharply peaked with a height of N^2 when the denominator evaluates to zero (i.e. $\mathbf{q} \cdot \mathbf{a} = 2\pi$). Everywhere else, it evaluates to nearly zero.

Putting together all expressions, the total diffracted amplitude is:

$$A_{tot} = A_0 \frac{e^2}{mc^2 R_0} F(\mathbf{q}) S_{N_1}(\mathbf{q} \cdot \mathbf{a}_1) S_{N_2}(\mathbf{q} \cdot \mathbf{a}_2) S_{N_3}(\mathbf{q} \cdot \mathbf{a}_3) \quad (12)$$

In order for there to be any appreciable intensity, each slit function must simultaneously be at or very near a maximum. These three Laue conditions can be written as:

$$\begin{aligned} \mathbf{q} \cdot \mathbf{a}_1 &= 2\pi h \\ \mathbf{q} \cdot \mathbf{a}_2 &= 2\pi k \\ \mathbf{q} \cdot \mathbf{a}_3 &= 2\pi l \end{aligned} \tag{13}$$

The vector \mathbf{q} that satisfies all three of these equations is:

$$\mathbf{q} = h\mathbf{b}_1 + k\mathbf{b}_2 + l\mathbf{b}_3 \tag{14}$$

The \mathbf{b} 's themselves define another lattice--the reciprocal lattice--and they are known as 'reciprocal lattice vectors.' They are derived from the original lattice vectors that described the crystal:

$$\mathbf{b}_1 = 2\pi \frac{\mathbf{a}_2 \times \mathbf{a}_3}{\mathbf{a}_1 \cdot \mathbf{a}_2 \times \mathbf{a}_3} \tag{15}$$

and similarly for \mathbf{b}_2 and \mathbf{b}_3 . The reciprocal lattice is a more convenient space to work in when describing and performing diffraction experiments. The diffraction condition is met when the momentum transfer vector, \mathbf{q} , connects the origin with one of the points on the reciprocal lattice. In practice, the measured intensities are reduced by the Debye-Waller factor which accounts for the thermal vibrations of each atom about its equilibrium position.

2.3 Size effect and mosaic

Considering equation 11 above, the effect of crystalline size can be determined. The slit function $S(\mathbf{q})$ can be approximated as a Gaussian because it is basically a sharp,

symmetrical peak:

$$\frac{\sin^2(N\mathbf{q} \cdot \mathbf{a} / 2)}{\sin^2(\mathbf{q} \cdot \mathbf{a} / 2)} \rightarrow N^2 \exp[-(N\mathbf{q} \cdot \mathbf{a} / 2)^2 / \pi] \quad (16)$$

This Gaussian has the same width and total area under the curve as the slit function. The width of the peak at half its maximum is then easily found:

$$\frac{1}{2} = \exp[-N^2 q^2 a^2 / 4\pi] \quad (17)$$

The solution of this gives the ‘‘Scherrer’’ formula:

$$\Delta q_{FWHM} = 2 \left(\frac{4\pi}{N^2 a^2} \ln 2 \right)^{1/2} = 0.94 \frac{2\pi}{Na} = 0.94 \frac{2\pi}{L} \quad (18)$$

where L is the crystal size along one direction and Δq is the width of the diffraction peak measured in reciprocal lattice units. Hence, the inverse of peak width is related to the size of the crystal causing the diffraction. In most diffraction experiments, L is very large and the measured width is due to instrumental effects and is considered ‘‘resolution limited.’’ However, special regions or domains within the crystal may give rise to additional diffraction peaks, and if their size is small enough, then the width of these peaks will give an estimate of the volume of the special regions.

When measuring peak widths, it is important to distinguish between the size effect and mosaic broadening. As discussed above, the size effect causes a peak to be broadened as a consequence of the finite size of the scattering medium. Hence, long-range-order features result in very sharp diffraction peaks, while shorter range order in the crystal result in broad peaks in the diffraction. Mosaic broadening is due to poor crystal quality and occurs when a sample is not single crystalline but is broken up into mosaic blocks that do not align with one another. Then the broadened peak is due to intensity coming from

the different blocks, or grains, that are at small angles to one another. If the broadening is due to the size effect, then peaks of different orders (e.g. (111) vs. (222)) will have roughly constant widths in reciprocal lattice units. In Chapter 4, the widths of superstructure peaks are used to measure the size of the domains that cause those additional peaks. These domains are embedded in the single crystal, but they have a special ordering pattern which allows one to distinguish them from the rest of the crystal. However, if the broadening is mosaic in nature, then the diffraction pattern will “fan out” as higher orders are measured and the peaks will have fixed widths in the theta angle. A schematic diagram in Figure 2.3 illustrates this mosaic effect. If the crystal quality is poor, then the mosaic broadening will mask any domain size broadening and the peak widths can not be used to measure domain size. In that case, the peak width is simply a measure of the mosaic blocks’ angular distribution.

2.4 Experimental details

In order to study the diffraction intensity from a given set of planes, the sample must be oriented properly with respect to the incoming beam and the detector. This is accomplished using a diffractometer. In these experiments, a Kappa geometry diffractometer was used (Figure 2.4). It consists of four motors: one controls the two-theta arm which positions the detector at the proper Bragg angle but does not change the sample position. The theta, kappa and phi motors combine to orient the crystal at the proper Euler angles of theta, chi and phi. This is a variation on the standard four circle diffractometer which would have separate theta, phi and chi motors. The role of the

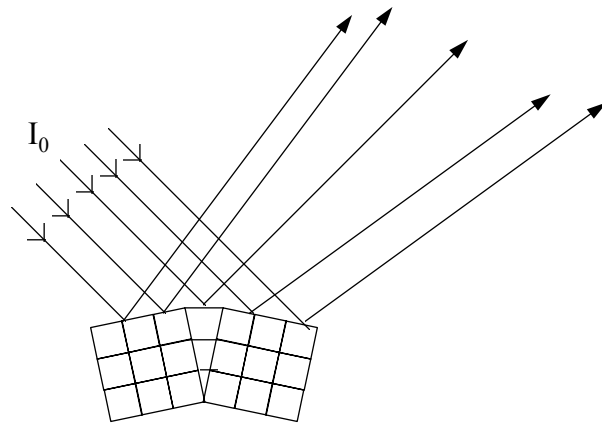


Figure 2.3. Schematic of a single crystal that is broken up into two mosaic blocks at a small angle to one another. The diffracted radiation is “mosaic broadened” resulting in a peak that has a width that is constant in theta even as higher order peaks are measured.

diffractometer is simply to hold the sample at a fixed position in space, while rotating it so that the required planes are meeting the diffraction condition. Since there are four motors, but only three degrees of freedom, there is more than one solution. The convention most commonly used in these experiments was to fix the theta angle to be one half of the two theta angle. This symmetric geometry gives the best access to the bulk of a flat plate sample because the incident and exit beams are kept far away from grazing.

The first step in a diffraction experiment is to determine how the sample has been mounted with respect to the diffractometer. One needs to locate a few diffraction peaks,

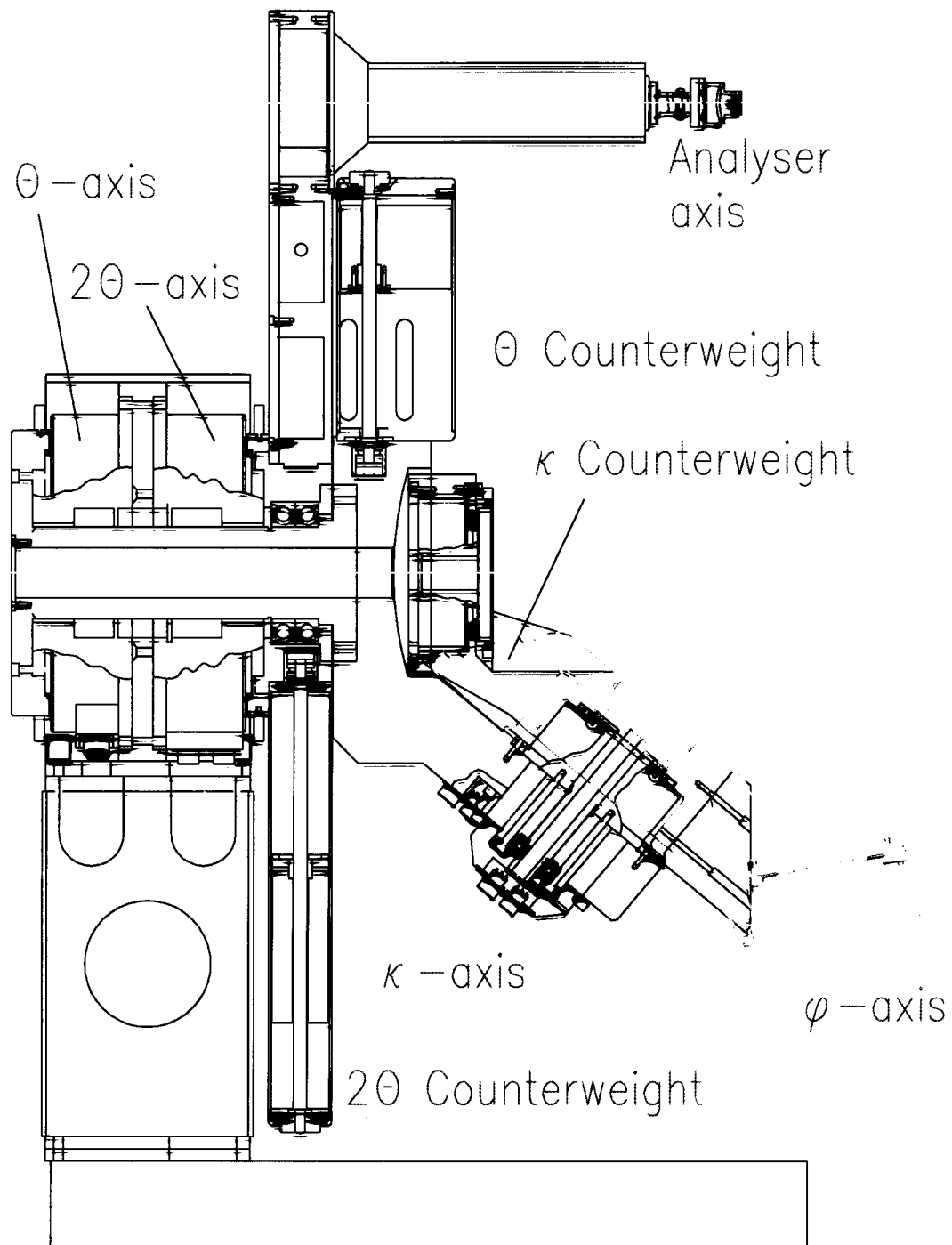


Figure 2.4. Diagram of the Kappa geometry diffractometer. The detector arm “analyzer axis” sets the 2θ or Bragg angle. The θ , κ , and ϕ arms position the sample at the proper orientation in the beam which is coming out of the page.

and precisely measure the angles where they occur. By knowing the lattice constant of the sample, the two-theta angle is easily determined using Bragg's law. (The lattice constant can be determined by powder diffraction if it is not known.) It is necessary to then hunt around in phi and chi space until a peak is found, the position of which can be used to help find a second peak. By knowing the position of two peaks and the lattice constant and symmetry of the crystal, the orientation is, in theory, determined. However, a more accurate orientation measurement is possible when several Bragg peaks are found, usually around six. With three or more Bragg peaks, the lattice constant, symmetry and orientation of the crystal are uniquely determined. Additional Bragg peaks are then found and a best fit is used to reduce measurement error. These sets of Bragg peaks give the orientation matrix, which is simply a transformation matrix from the known coordinate system of the diffractometer to the unknown coordinate system of the crystal. The results of an accurate orientation matrix are determination of the lattice constants and the face of the crystal that the beam is penetrating.

For a crystallographic study, the complex structure factors, F , need to be measured. As seen in equation 12, the intensity of a given peak is proportional to the square modulus of the structure factor, so that the complex phases can not be directly measured. It is thus necessary to have some idea of what structure you are measuring which is then refined to match the measured data. Intensities are measured by scanning the crystal through the diffraction peak and integrating the resulting peak. This must be corrected for absorption effects as described in Chapter 4 before the square root can be taken to give a quantity that is proportional to $|F|$.

With a measured set of magnitudes for the structure factors within a given range of momentum transfer, it is possible to fit the data to a model. Because of the lack of phase

information, it is necessary to assume models which provide initial positions for each atom within the unit cell. The overall symmetry of the crystal can restrict the atomic displacements to certain planes. The positions of various atoms as well as Debye-Waller factors can then be varied until a satisfactory fit is obtained. The Debye-Waller factors are tabulated for each element and represent the magnitude of thermal atomic vibrations. It is important to emphasize that because x-ray diffraction collects data from a large region of a crystal, the result is the *average* crystal structure, hence diffraction is considered a long range order technique.

All x-ray diffraction data presented in this thesis were collected at beamline X16C of the National Synchrotron Light Source (NSLS) which is part of Brookhaven National Laboratory. The NSLS is a user facility that supports about 60 x-ray beamlines. The synchrotron source produces a broad spectrum of x-ray energies, from about 0.5 to 50 keV. Typically, the accelerator storage ring is operated at an energy of 2.5 GeV.

X16C is a multi-purpose beamline that can be used for standard diffraction experiments, as well as EXAFS and micro-beam experiments. A vertical slit at the beginning of the beamline helps define the beam and reduce the thermal load on the monochromator. A double crystal Si monochromator is used to define the energy of the beam. The Si single crystals are cut with $\{111\}$ orientation and can be rotated together to continuously vary the energy. Since the (222) reflection is forbidden in silicon's diamond structure, second order harmonics are eliminated. The beam diffracts from the first crystal and into the second crystal which also diffracts the beam so that the beam propagation direction is not changed. The second crystal is also curved to help focus the beam at the center of the diffractometer. A set of motors fine tunes the bending of the second crystal to improve the focusing. A typical beam profile at the sample position is 1.0 mm in the

vertical direction and 0.5 mm or less in the horizontal. The focusing greatly reduces the horizontal profile and increases the photon flux by more than an order of magnitude. Third order harmonics can either be discriminated against by the detectors, or can be largely eliminated by de-tuning the second crystal slightly.

In the experimental hutch, I_0 slits further define the beam and eliminate any stray beams. On the detector arm, 2 sets of vertical and horizontal slits are present. The first “guard” slits eliminate stray radiation while the “detector” slits (positioned immediately before the detector) ensure that only diffracted radiation at the desired Bragg angle reaches the detector. The width of these slits is usually about 2 mm and is set so that each slit just cuts into the actual beam; the beam is then well-defined by the slits but not too much radiation is lost. For the experiments described here, a Kappa geometry four-circle diffractometer was installed inside the experimental hutch, and Bicron scintillators were used to detect the photons.

2.5 Resonant scattering

The atomic form factor, f_0 , as described above, does not consider the possibility of electronic excitations within the atom. Each atom scatters according to the number and distribution of electrons that it contains as reflected by f_0 , which is simply the Fourier transform of the electronic density. For conventional x-ray diffraction experiments, the wavelength is chosen such that no atomic excitations occur. The atomic form factors are

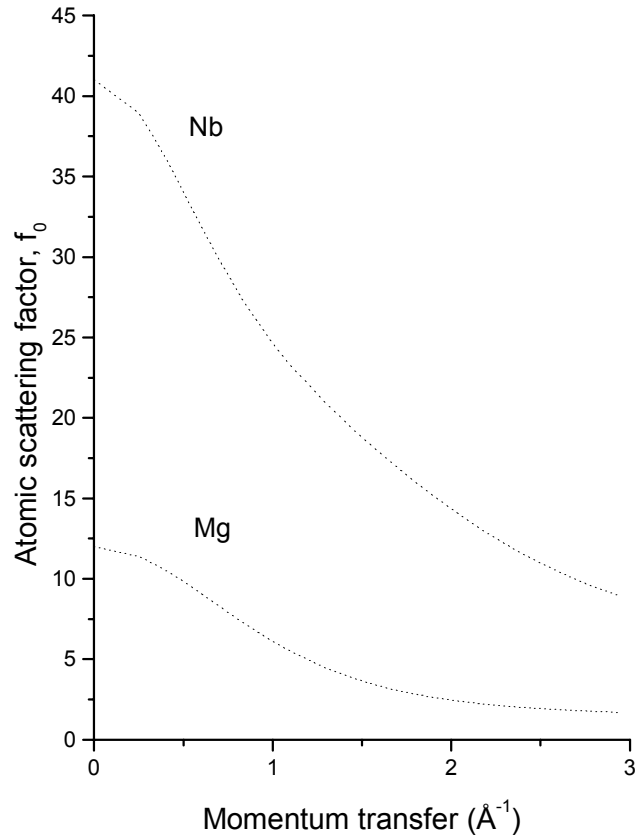


Figure 2.5. Atomic form factors, f_0 , for Nb and Mg [2]. At zero momentum transfer, they evaluate to Z . Atomic excitations are included in the anomalous corrections, f' and f'' .

then smoothly varying functions with momentum transfer, $|q|$, (Figure 2.5) which can be closely approximated as polynomials as tabulated in the International Tables for Crystallography [3].

The complete expression for atomic form factors, however, includes terms that account for the atomic excitations and is written as:

$$f(\mathbf{q}) = f_0(\mathbf{q}) + f'(E) + if''(E)$$

where f_0 is the smoothly varying form factor, and $f'(E)$ and $f''(E)$ represent the anomalous scattering corrections. As an example, the $f'(E)$ and $f''(E)$ of Mg are shown in Figure 2.6

[4]. The K-shell atomic excitation level for Mg is at 1.25 keV, and the effect on f' and f'' are clearly seen as the sharp and narrow dip in f' and the jump in f'' at the absorption edge. When the incoming photon's energy, E , is near an atom's atomic absorption edge, that photon can be absorbed by an electron (usually K or L shell) which is then expelled

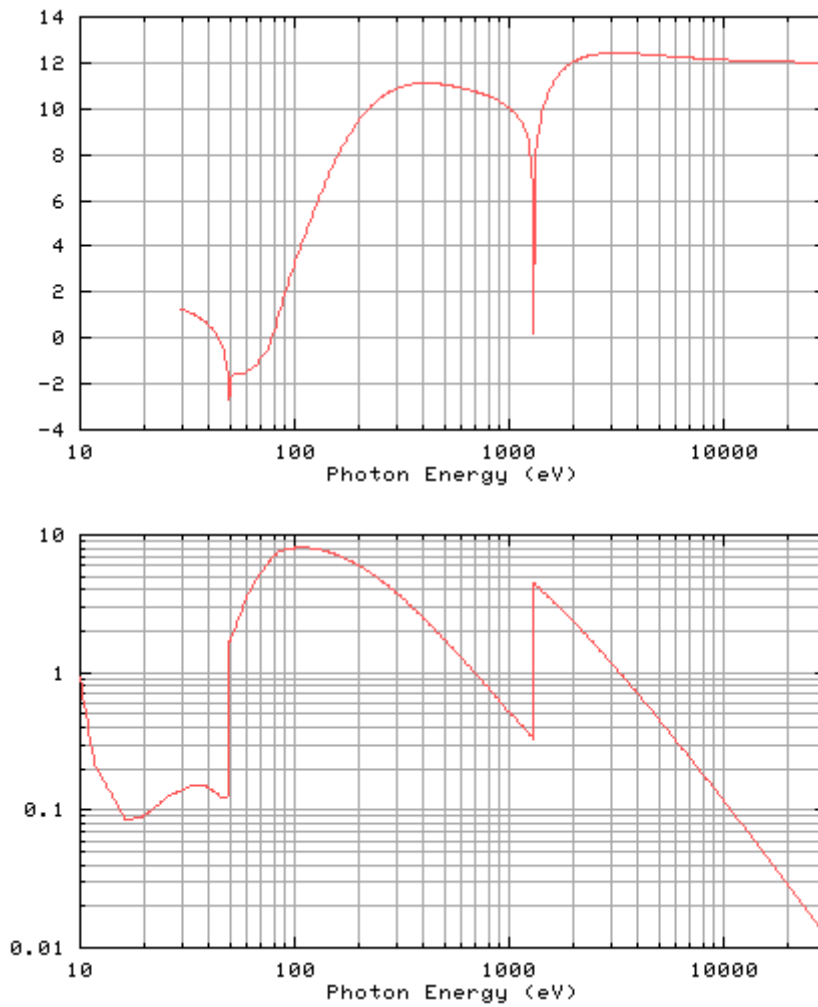


Figure 2.6 Anomalous scattering factors, $f'(E)$ and $f''(E)$, for Mg [4].

from the atom with energy $E - E_{\text{binding}}$. The empty shell is then filled by an electron from a higher shell which causes fluorescent radiation at the atom's characteristic energy. The effect of photoelectric absorption is to produce jumps in each atom's scattering power. It is the most probable interaction between photons and matter. As seen in Figure 2.7 [5], it is about 3 orders of magnitude more likely than Thomson scattering in the x-ray energy range.

This process is used in “conventional” x-ray sources where energetic electrons bombard a metallic target which then radiates x-rays at its characteristic atomic levels. The K lines of copper and molybdenum are the most commonly used sources. The problem with these sources compared with synchrotron radiation (without even

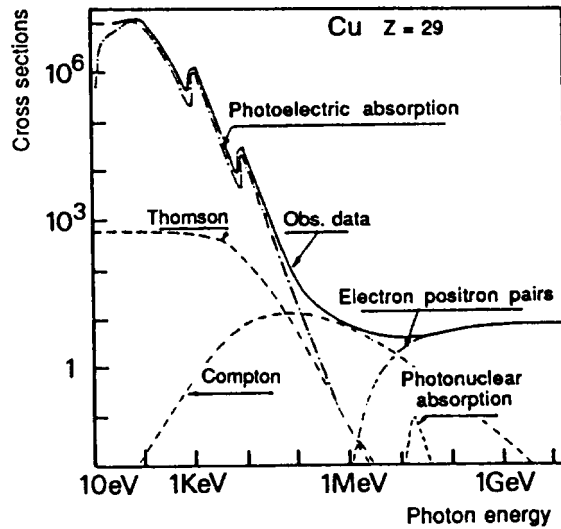


Figure 2.7. Cross sections of the copper atom interacting with photons [5]. The solid line represents the total cross section. Photoelectric absorption is most significant in the x-ray range, but Thomson scattering dominates in the diffraction condition.

considering their lower intensity) is that one is limited to performing experiments at specific energies pre-determined by nature. With the advent of synchrotron sources, not only has the intensity of x-rays improved by 2 to 4 orders of magnitude, but the ‘white’ radiation coming from the synchrotron is passed through a monochromator crystal that can be easily tilted to provide any energy within a broad range. For example, at beamline X16C of the NSLS, incoming x-ray energy can be varied from about 5-25 keV with a resolution of a few eV.

When detecting radiation that is passed straight through a crystal, one observes primarily the absorption cross section. This is the common procedure for Extended X-ray Absorption Fine Structure (EXAFS) measurements, discussed in Chapter 6. However, for x-ray measurements, the detector is at some angle to the incoming radiation (the Bragg angle). In these cases, the Thomson scattering is predominant in the typical x-ray range. At higher energies ($> 50\text{keV}$), the incoherent Compton scattering actually becomes more likely than Thomson scattering. Although Thomson scattering from an individual electron has a very small cross section, at the proper Bragg angle enough electrons scatter coherently to produce the sharp and intense diffraction peaks. When not situated at a Bragg angle, a certain amount of background radiation from both Thomson and Compton scattering is detected. This background is flat and featureless except when near an absorption edge. As the incoming photon is given enough energy to cause photoemission, the filling of the empty state causes fluorescent radiation which is given off in all directions. This causes a decrease in the amount of the beam that is passed through the sample (at zero degrees) due to the jump in absorption at the edge. This is reflected in the increase of f'' which is proportional to μ , the absorption coefficient. The effect of f'' is to

reduce the scattering of the atom very close to the absorption edge due to resonance effects.

In experiments, by tuning the wavelength through an absorption edge, the f' can effectively be turned off and on while f'' is accounted for by a known absorption correction. Thus it is possible to determine the phase and how much of a given atom is contributing to a diffraction peak by measuring intensities as the energy is tuned through the resonance condition. In principle, this is possible even without exploiting the resonance condition because each atom has a unique f_0 as well. However, the f_0 's are generally featureless away from atomic transitions and their smoothly varying shape does not provide enough contrast to perform such an experiment. Measurements of absolute intensity are not precise enough to give reliable information in all cases, so the anomalous scattering signature is used to identify specific atoms and their scattering phases.

In Chapter 6, further effects of anomalous scattering will be used to determine short range order. Techniques such as EXAFS and diffraction anomalous fine structure (DAFS) will be described and used to study lead magnesium niobate (PMN). These techniques measure the intensity of photons just above an absorption edge. The ejected photoelectrons interact with the neighboring atoms resulting in an interference pattern of oscillations of intensity. This pattern can be fit to a standard equation to determine the local structural environment out to a few nearest neighbors. Used together with conventional x-ray diffraction, which is a long range order technique, EXAFS and DAFS can give short range complementary information on the detailed structure of a crystal. In addition, resonant scattering will be used to determine the relative Nb composition in different regions of PMN in the second part of Chapter 6.

2.6 References

- [1] B E Warren, *X-ray Diffraction*, (Addison-Wesley, Massachusetts, 1969).
- [2] I K Robinson, D J Tweet, *Rep. Prog. Phys.*, **55** 599 (1992).
- [3] *International Tables for X-ray Crystallography*, 2nd ed. edited by C H MacGillavry and G D Rieck (Reidel, Dordrecht, 1983), Vol. III.
- [4] B L Henke, E M Gullickson, J C Davis, *Atomic Data and Nuclear Data Tables*, **54** [2] (1993).
- [5] A. Fontaine, *Neutron and Synchrotron Radiation for Condensed Matter Studies*, **1**, 323 (1996).

Chapter 3

Ferroelectrics

3.1 Definition and properties

Ferroelectric materials contain one or more polar axes along which a spontaneous polarization can be developed below the material's Curie temperature. The application of a strong enough electric field can force the polarization direction to be changed. The arrangement of cations and anions within a ferroelectric gives rise to dipole moments within each unit cell, and the resulting polarization can be measured via the material's surface current. One distinctive characteristic of ferroelectrics is the hysteretic behavior in the polarization vs. electric field curve. As shown in Figure 3.1, a net spontaneous polarization exists even after the electric field is turned off. Above the Curie temperature is known as the paraelectric phase where the material has higher symmetry and behaves like a normal dielectric with no hysteresis. Some ferroelectrics have additional ferroelectric-ferroelectric transitions (usually to lower symmetry) below the Curie temperature and some even undergo a transition back to a paraelectric state. Rochelle salt (sodium potassium tartrate tetrahydrate) exhibits upper and lower Curie temperatures and was the material in which ferroelectricity was first observed [1].

Eleven of the 32 possible crystal classes are centro-symmetric and hence have no unique polar axis and cannot exhibit ferroelectricity. The remaining 21 crystal classes

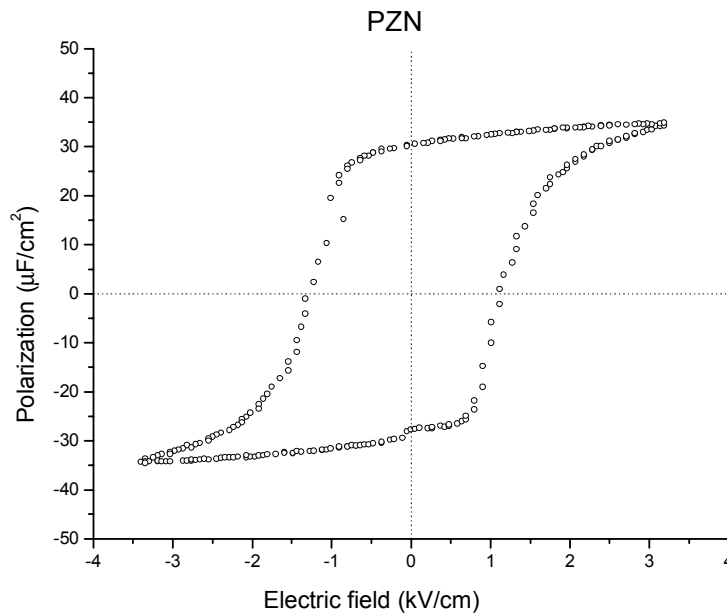


Figure 3.1. Typical hysteretic behavior of ferroelectrics. Application of a field aligns the dipoles along the field direction and the net polarization is maintained even after removing the field.

exhibit the pyroelectric effect, which is a change in polarization when the temperature is varied, and all but one of these are piezoelectric. The direct piezoelectric effect is the development of strain in a crystal when an electric field is applied. The inverse effect, development of polarization when a strain is applied, also occurs. The phenomenon of electrostriction is a second order piezoelectric effect in which the developed strain is proportional to the square of the applied electric field. Piezoelectric and electrostrictive tensors describe a material's behavior under electric field in many important applications. Typically, the piezoelectric effect is much larger, but in certain materials the

electrostrictive effect dominates and is preferred because the strain direction is independent of field direction and the hysteresis effects are reduced. Applications range from simple acoustical devices such as microphones to advanced positioning devices for scanning microscopes. One of the most commonly used electrostrictive materials is lead magnesium niobate with the chemical formula $\text{Pb}(\text{Mg}_{1/3}\text{Nb}_{2/3})\text{O}_3$, or PMN, and solid solutions of PMN with lead titanate, PbTiO_3 .

The ability of ferroelectrics to change their atomic structure under the influence of electric fields gives rise, in some cases, to extremely high values of permittivity, and hence dielectric constant. For example, lead magnesium niobate in single crystal form has a dielectric constant just over 30,000 with the actual maximum depending on measurement frequency and temperature. The discovery of barium titanate and related ferroelectrics in the late 1940's marked the beginning of intense ferroelectric research. These materials were widely developed as thin layer capacitors for use in integrated circuits for charge storage, bypass and coupling functions. The piezoelectric effect is the most common useful property of ferroelectrics. Lead zirconate titanate, $\text{Pb}(\text{Zr}_x\text{Ti}_{1-x})\text{O}_3$ or PZT, dominates this field today, but new applications and materials are always being developed. Two of the most significant recent applications involve incorporating ferroelectrics into silicon devices. The high dielectric constant materials are being developed for increased charge storage in a smaller area in memory chips. The ability of ferroelectrics to exist in two different polarizations in the absence of a field is being used for non-volatile ferroelectric memories.

Another characteristic feature of ferroelectrics is remanent polarization. Applying a variable electric field to a ferroelectric results in the hysteretic behavior as seen in Figure 3.1. At high fields, a saturation value of polarization is reached. As the electric field

returns to zero the system is left with a spontaneous polarization which can be flipped by applying a large enough field in the opposite direction. In contrast, a normal dielectric has no spontaneous polarization and its P-E curve is simply a straight line with a slope of $\chi_e \epsilon_0$ where χ_e is the electric susceptibility or one less than the relative dielectric constant.

3.2 Perovskite structure

The most commonly studied ferroelectrics have the cubic perovskite structure (in the paraelectric state) with chemical formula ABO_3 (Figure 3.2). As conventionally drawn, A-site cations occupy the corners of a cube, while B-site cations sit in the body center. Three oxygen atoms per unit cell rest on the faces. The lattice constant of these perovskites is always close to 4 Å due to the rigidity of the oxygen octahedra network and the well defined oxygen ionic radius of 1.35 Å. All materials in this study have structures based on the perovskite structure, with displacements which are important because they result in polarization and can also lead to crystal symmetry changes. Another common ferroelectric structure is the layered perovskite structure which consists of a varying number of perovskite unit cells separated by an oxide layer. This structure is also found in many high T_C superconductors.

A practical advantage of the perovskite structure is that many different cations can

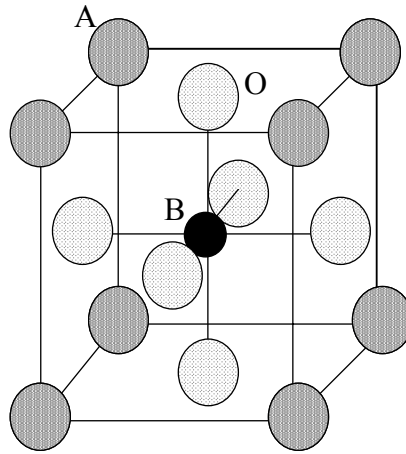


Figure 3.2. Perovskite ABO_3 structure with the A and B cations on the corner and body center positions, respectively. Three oxygen anions per unit cell occupy the faces and form octahedra surrounding the B-site.

be substituted on both the A and B sites without drastically changing the overall structure. Complete solid solutions are easily formed between many cations, often across the entire range of composition. Even though two cations are compatible in solution, their behavior can be radically different when apart from each other. Thus, it is possible to manipulate a material's properties such as Curie temperature or piezoelectric constant with only a small substitution of a given cation. Also, it is possible to combine materials that would otherwise have different symmetries; this can have the effect of radically altering the piezoelectric behavior. More recently, this compatibility within the perovskite system has made it possible to tailor a material's lattice constant for matching with a substrate in thin film applications.

3.3 Normal and relaxor ferroelectrics

Barium titanate, BaTiO₃ or BT, is the most commonly studied “normal” ferroelectric. Normal ferroelectrics are characterized by a sharp phase transition from the paraelectric to ferroelectric state as seen in the permittivity as a function of temperature (Figure 3.3). In BT, the ferroelectric transition occurs at 120° C, which roughly corresponds to the peak in permittivity. Below the Curie temperature, the cubic structure changes to lower symmetry and there is a sharp decrease in dielectric constant. Above the Curie temperature, T_C, the relative permittivity follows the Curie-Weiss law:

$$\epsilon_r = \frac{A}{T - T_C} \quad (1)$$

In contrast, relaxor ferroelectrics have permittivity peaks that are more gradual and often

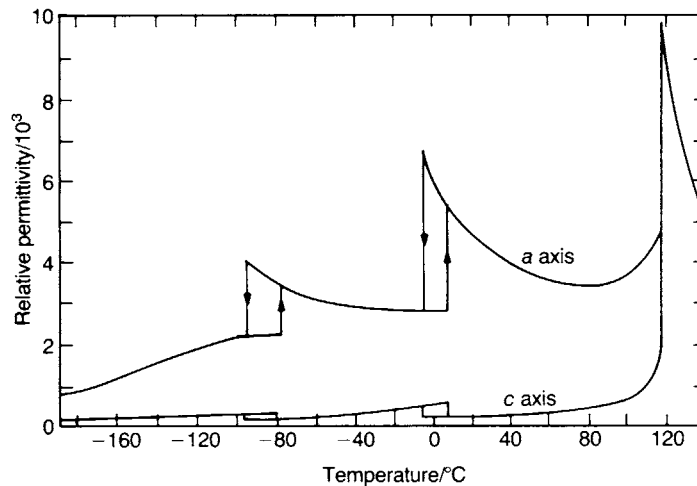


Figure 3.3. Dielectric constant of barium titanate vs. temperature [1]. At 120° C there is a first order phase transition from the paraelectric to ferroelectric state and a sharp increase in dielectric constant. Transitions to lower symmetry occur as the temperature is lowered.

contain more than 2 cations. Lead magnesium niobate, $\text{Pb}(\text{Mg}_{1/3}\text{Nb}_{2/3})\text{O}_3$, is the prototypical relaxor ferroelectric and consists of a mixed B-site: Pb occupies the corner A-site and the B-site can be either Mg or Nb. Its very large maximum in permittivity (Figure 3.4) exhibits a broad transition and is also measurement frequency dependent which are the characteristics of relaxors. As the measurement frequency is increased, the maximum of the permittivity decreases while the temperature of that maximum increases. In normal ferroelectrics, the sharp transition in permittivity also indicates a phase transition as the symmetry of the crystal changes. For relaxors, however, the broad peak in ϵ does not always correspond to a structural phase transition, so the temperature of the maximum permittivity is designated T_M instead of T_C . In the case of PMN, there are local polar

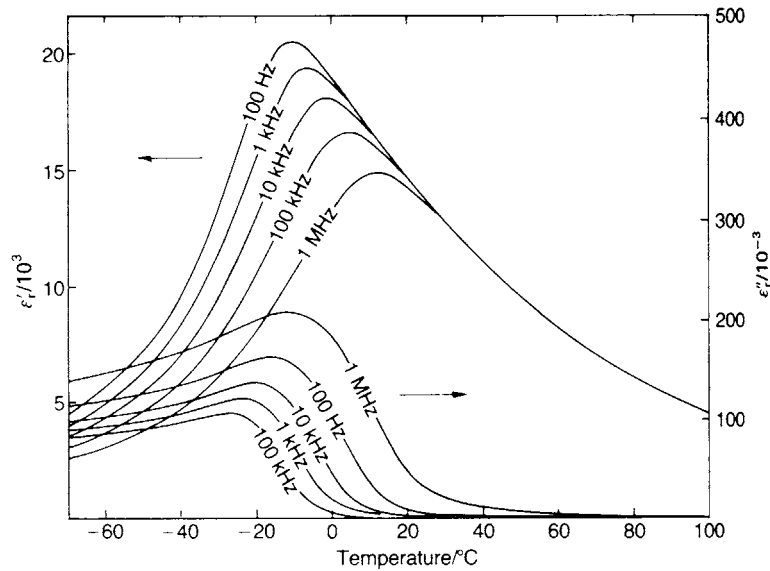


Figure 3.4. Dielectric constant (left) and dielectric loss (right) of the relaxor lead magnesium niobate as a function of temperature [1]. Note the gradual transition and the dependence on measurement frequency.

regions that exist well above T_M , and flipping of polar domains continues below it.

However, no overall transition to a ferroelectric state occurs even down to 4 K [2]. Small micro domains on the order of 100 Å [3] have rhombohedral symmetry, but the average structure remains cubic. By combining PMN with lead titanate, $PbTiO_3$, solid solutions may be formed. Lead titanate is a normal ferroelectric with large polar domains and an abrupt transition from the paraelectric to ferroelectric phase at 490° C. Combining PMN with small amounts of PT can cause PMN to behave more like a normal ferroelectric, and at 30% concentration of PT and above, PMN-PT is a normal ferroelectric.

The frequency dispersion and more gradual dependence of the permittivity on temperature have encouraged the development of PMN and other relaxors in many applications. Both the high dielectric constant and impressive electrostrictive coefficients have been exploited. Currently, applications of PMN are wide-ranging. The high dielectric constants are used in ever smaller multi-layer ceramic capacitors. Relaxors are especially useful in this regard not only because of their very high dielectric constants, but because those high values occur near room temperature and have a gradual temperature dependence. In contrast, a normal ferroelectric will typically have its maximum occur at around 500° C, and the sharp temperature dependence makes it unsuitable for applications. Piezoelectric effects are exploited in a large number of applications, and the electrostrictive effect in materials like PMN allows for very precise control. Thus, they are employed in such applications as micropositioners, biomedical instruments and surface deformable mirrors [4]. PMN also has good electro-optic properties, so its index of refraction can be changed by applying a field. Optical shutters and switches take advantage of this effect [5].

3.4 Relaxor theories

Ferroelectrics provide a convenient system to study the general properties of phase transitions. Normal ferroelectrics undergo a sharp phase transition at the Curie temperature. Above T_C , each atom within the unit cell is located on a high symmetry position with no net dipole moment. Atoms are free to vibrate about these equilibrium positions, exciting the various acoustic and optical phonon modes. The frequency of some of these modes is temperature dependent, and as temperature is lowered, the force constant of a given mode approaches zero at the phase transition. This is known as ‘softening’ of the mode and allows the atoms to shift without hindrance along that mode’s direction. Spontaneous polarization allows for any symmetrically equivalent direction to be chosen initially and then cooperative effects encourage the other unit cells to also align in that direction and can result in a change of symmetry. In the presence of an external electric field, the polarization direction is determined by the field direction. Domain boundaries can exist in which different grains have different dipole orientations.

In relaxor ferroelectrics, such as PMN, the situation is more complicated. There is not a uniform atomic shift throughout the entire crystal, so that the net polarization remains zero, but microscopic polar domains develop. Various theoretical models have been proposed to explain relaxor behavior and have been reviewed by Ye[6]. Smolenskii [7] initially proposed that PMN’s relaxor behavior was due to varying local Curie temperatures. Due to the randomness that exists on the B-site, each unit cell is subjected to a different net field, so there are a range of possible Curie temperatures, resulting in the broadened transition of permittivity versus temperature. This simple model has been

widely cited since its introduction, but now there are efforts to more formally describe the relaxor behavior.

Cross proposed the superparaelectric model for relaxors[8]. Similar to the superparamagnetic state, it involves polar micro regions that are dynamically disordered above T_m , the mean Curie temperature of the different regions. Cations continuously flip between equivalent directions (for example $\langle 111 \rangle$), activated by thermal energy. The heterogeneity caused by the mixed B-site creates locally favorable directions, so the local symmetry is lower than the global. However, the energy barrier separating the different directions is small, so macroscopic polar domains never form as in normal ferroelectrics.

Dipolar glass-like behavior is another possible model. Viehland et al [9] showed evidence for glassy behavior by analyzing the dielectric response using the Vogel-Fulcher relationship [10] which also implies activated dynamics. The glassy nature was believed to be due to the randomly oriented dipolar fields, and the evidence was seen in the very slow dynamics. Contrary to the superparaelectric model, cations are frozen along a particular $\langle 111 \rangle$ direction. Fitting to the Vogel-Fulcher relationship gave a freezing temperature of 217 K. This is well below the maximum of the dielectric response, and is the temperature below which the micro domains can no longer change their polarization direction. Another recent theory invokes the contributions from a quenched random field which is again due to the compositional heterogeneity. Kleemann et al [11] proposed that PMN's broad phase transition is due to random field interactions which also cause freezing into nanometric domains.

The charge heterogeneity within PMN and its relation to the ferroelectric domains should help to understand the behavior of this relaxor, and is the subject of Chapter 4. Generally, chemical heterogeneity (on the B-site) is believed to play an important role in

the diffuse phase transition behavior. By adding dopants to the A and B-sites in PMN, the amount of chemical order on the B-site can be changed providing a measure of how that order affects PMN's relaxor behavior and structure. Additional experiments will be presented on the similar relaxor lead zinc niobate. In Chapter 5, the effect of strain on PMN's ordering will be investigated by studying thin films. Chapter 6 presents experiments using diffraction anomalous fine structure and atomic resonance which are techniques for measuring the local order and compositional variations. These methods serve as complements to the x-ray diffraction measurements.

3.5 Thin films

The most common form of ferroelectrics for both research and applications is ceramic. Ceramics are easy to form and can be pressed into whatever shape is necessary. Single crystals are more difficult to grow and are generally too expensive for applications, but they are used in research as their material properties tend to be better and orientational effects can be studied. In the past decade or so, however, there has been a surge of interest in ferroelectric thin films in both research and application. Thin films can have material properties that approach those of the bulk in the limit of thick samples, but often have higher breakdown voltages. Other advantages include the ability to make very small devices which can be densely packed. By incorporating ferroelectric elements with silicon based integrated circuits, "smart" devices can be developed. Such devices would use the ferroelectrics to act as sensors which would send information to a feedback unit. The device could then respond to its environment using the actuation properties. Thin films

provide a means of studying both surface and interfacial effects which may affect a material's properties and phase transition behavior.

Advances in deposition techniques have helped drive this growth in developing thin films. The two general classes for depositing ferroelectrics onto substrates are vapor phase deposition and liquid phase chemical processing techniques. The former allows for careful control of film thickness, orientation and stoichiometry but is often more costly and time consuming. Liquid phase techniques are cheaper and faster and often produce films with better properties, even though the crystalline quality of the film is inferior. Typically, thin film growth occurs at lower temperatures than single crystal or ceramic sintering temperatures which is important for compatibility with a given substrate.

One of the most important thin film ferroelectrics is lead zirconate titanate, $\text{Pb}(\text{Zr}_x\text{Ti}_{1-x})\text{O}_3$. PZT is the most commonly used material for piezoelectric applications in both bulk and thin film form. Complete solid solutions of the parent compounds--lead zirconate and lead titanate--are formed across the entire composition range, and the best piezoelectric properties are found near the morphotropic phase boundary at $x = 0.47$ as seen in the chemical phase diagram (Figure 3.5). This is a chemical compositional transition from rhombohedral to tetragonal phases, and materials on this "morphotropic phase boundary" exhibit the highest piezoelectric coefficients. Although PZT is ferroelectric, and lead titanate is also ferroelectric, lead zirconate is actually anti-ferroelectric and has a transition to the paraelectric cubic state at 230°C [12]. In lead zirconate, displacements of Pb atoms in adjacent unit cells are in equal but opposite directions, thus making it anti-ferroelectric. Its permittivity versus temperature behavior

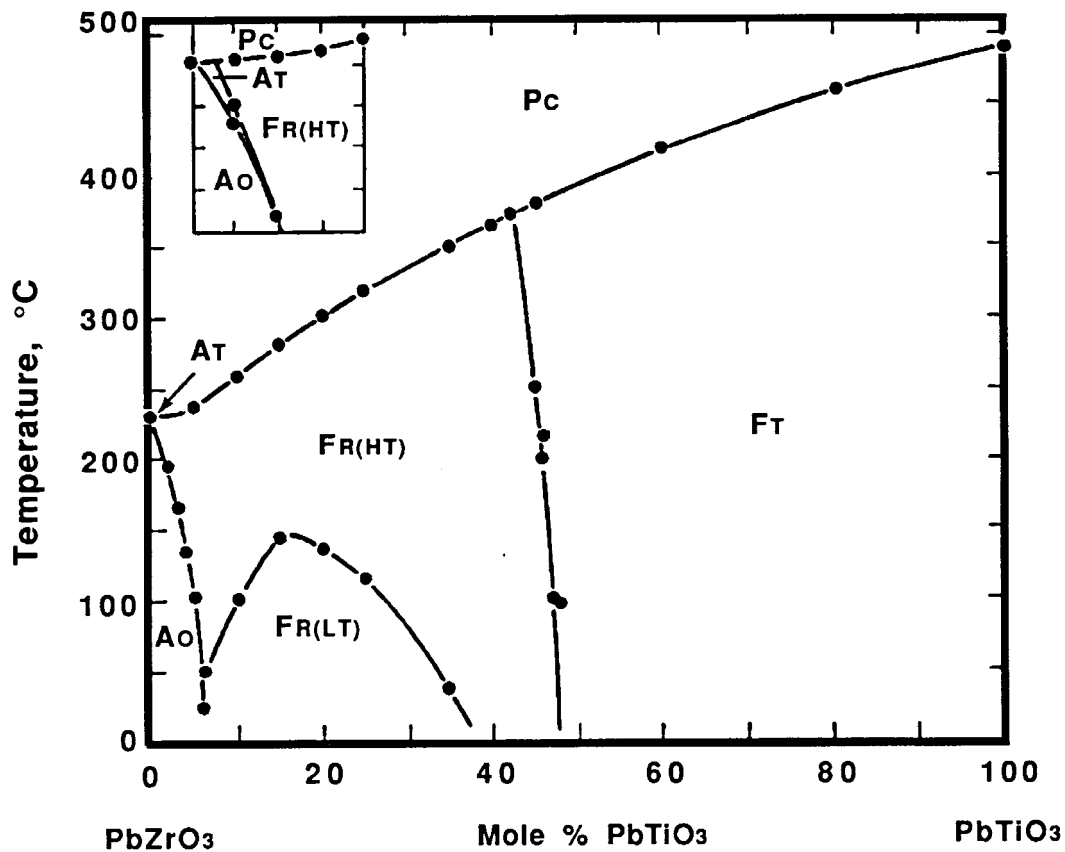


Figure 3.5. Phase diagram of the lead zirconate--lead titanate system [1].
 'F' = ferroelectric, 'A' = anti-ferroelectric, 'P' = paraelectric
 'O' = orthorhombic, 'R' = rhombohedral, 'T' = tetragonal, 'C' = cubic
 The "morphotropic phase boundary" between the R and T phases gives rise to the largest piezoelectric constant materials.

(Figure 3.6) resembles a normal ferroelectric, and it is believed that the anti-ferroelectric state is only slightly more stable than the ferroelectric. However, there is no dielectric hysteresis for the anti-ferroelectric phase. By applying an electric field, lead zirconate can be forced into the ferroelectric state. In Chapter 7, experiments on lead zirconate thin films will be discussed.

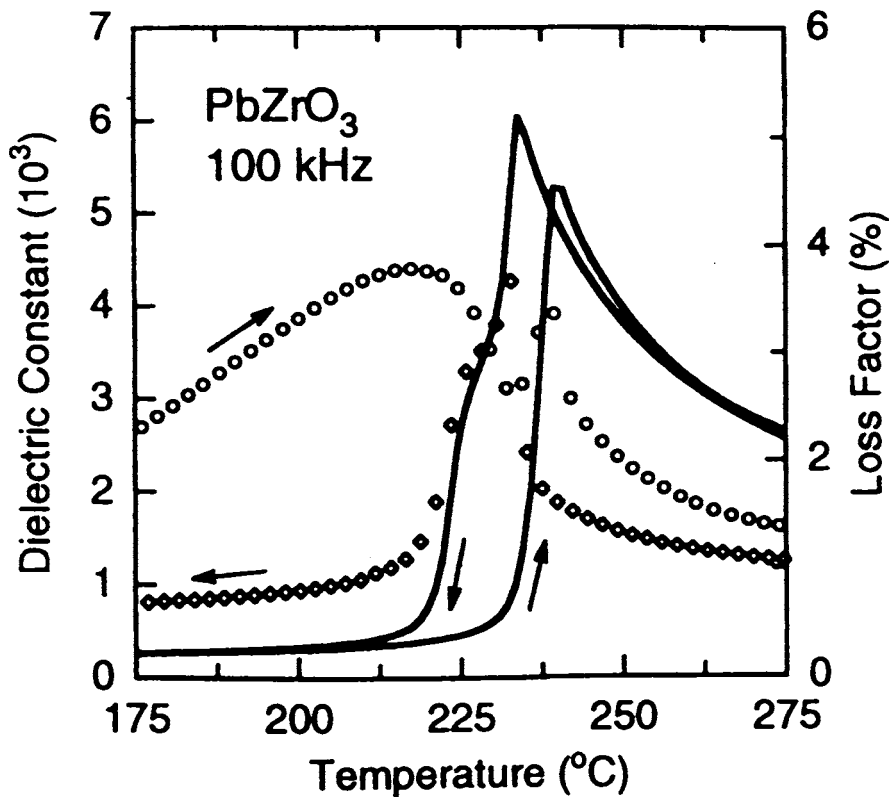


Figure 3.6. Dielectric constant (solid) and dielectric loss (circles) of bulk lead zirconate on heating and cooling cycles [13].

3.6 References

- [1] A J Moulson and J M Herbert, *Electroceramics: Materials, Properties, Applications*, (Chapman and Hall, London, 1990).
- [2] N de Mathan, E Husson, G Calvarin, J R Gavarris, A W Hewat, A Morell, *J. Phys.: Condens. Matter* **3**, 8159 (1991).
- [3] V A Isupov, *Ferroelectrics* **90**, 113 (1989).
- [4] K Uchino, *Ferroelectrics* **151**, 321 (1994).

- [5] L E Cross, S J Jang, R E Newnham, S Nomura and K Uchino, *Ferroelectrics* **23**, 178 (1990).
- [6] Z-G Ye, *Ferroelectrics* **184**, 193 (1996).
- [7] G A Smolenskii, A I Agranovskaya, *Sov. Phys. -- Tech. Phys.*, **3** [7] 1380 (1958).
- [8] L E Cross, *Ferroelectrics* **76**, 241 (1987).
- [9] D Viehland, S J Jang, L E Cross and M Wuttig, *J. Appl. Phys.* **68**, 2916 (1990).
- [10] G Fulcher, *J. Am. Cer. Soc.*, **8**, 339 (1925).
- [11] W Kleemann and A Klossner, *Ferroelectrics* **150**, 35 (1993).
- [12] M E Lines, *Principles and Applications of Ferroelectrics and Related Materials*, (Oxford University Press, Oxford, 1977).
- [13] X Dai, Z Xu, D Viehland, *J. Appl. Phys.* **77** [10] 5086 (1995).

Chapter 4

Lead Magnesium Niobate

4.1 Introduction

Relaxor ferroelectrics are characterized by a frequency dependent dielectric response which has a broad maximum as a function of temperature. In addition, relaxors possess a local polarization at temperatures above their dielectric maximum. In contrast, “normal” ferroelectrics have a sharp phase transition peak in dielectric constant at their Curie point, and no polarization exists above that temperature. The origin and explanation of relaxor behavior is an ongoing research problem. The prototypical relaxor is lead magnesium niobate, or $\text{Pb}(\text{Mg}_{1/3}\text{Nb}_{2/3})\text{O}_3$, which was first synthesized by Smolenskii and Agranovskaya in 1958 [1]. Its dielectric behavior is shown in Figure 3.4. PMN has found applications in a variety of devices where its unique properties have been exploited, even if they are not perfectly understood. Of greatest interest is PMN’s very high dielectric constant ($\sim 30,000$) over a wide temperature range near room temperature.

Lead zinc niobate, or $\text{Pb}(\text{Zn}_{1/3}\text{Nb}_{2/3})\text{O}_3$, also has a very high dielectric constant with similar relaxor behavior, but its Curie temperature is 140°C versus -7°C for PMN. PZN has excellent dielectric and piezoelectric properties, especially in solid solutions with lead titanate [2]. Whereas PMN remains cubic down to 5 K [3], PZN undergoes a symmetry change from cubic to rhombohedral at its Curie temperature and is able to

sustain the growth of polar macrodomains[4]. PZN is a somewhat ‘new’ material, but since the discovery of its very high electromechanical coupling coefficients it has received a lot of attention[2]. Single crystals of PZN and La-doped PZN crystals were grown for this work to compare their behavior to PMN. This chapter focuses on the superstructures found in PMN and PZN, and their relation to the relaxor behavior. Historically, PMN is the more important and widely studied material and will be used in the background discussion. Data collection and analysis procedures were identical for both materials, and the PZN results are included at the end of this chapter.

4.2 Literature review

Both PMN and PZN have the common ABO_3 cubic perovskite structure with a mixed B-site. However, the finer points such as the size and direction of ion displacements within the perovskite model have not been easy to deduce [5,6,7]. This is important because it determines the overall symmetry of the crystal and therefore its ferroelectric behavior. There has been a growing interest in understanding the ordering that occurs at the B-sites. Initially, these compositional fluctuations within nanodomains were believed to create different regions having varying Curie temperatures [8], thus giving PMN its broad relaxor response. Smolenskii [9] proposed that local inhomogeneities in chemistry and/or structure result in microdomains having a distribution of Curie temperatures, leading to a diffuse peak in dielectric constant. However, the situation appears more complicated as La-doped PMN retains its relaxor properties even when micron sized chemically ordered domains form [10] and experiments by Davies, et al, have found relaxor behavior in highly ordered $Pb(Mg_{1/3}Ta_{2/3})O_3$ and similar

systems[11]. As discussed in Chapter 3, theoretical interpretations of relaxors have been offered using various models. A clearer understanding of the charge heterogeneity within PMN and its relation to the ferroelectric domains should help to understand the behavior of this relaxor. Specifically, since the compositional fluctuations on the B-site are believed to be responsible for the relaxor behavior, the effects of both increased and decreased chemical order on the B-site will be studied.

As will be shown, there are two distinct types of domains within PMN, both on the nanometer scale. The ferroelectric nanodomains have local rhombohedral (polar) symmetry and grow only to a maximum of 100 Å [3]. These are the domains that give PMN its ferroelectric behavior, but unlike normal ferroelectrics, they never coarsen into large domains. The limited extent of the polar domains does not allow micron sized domains to form as in normal ferroelectrics. In this work, attention is focused on the second type of nanodomains in PMN which will be shown to be chemically ordered domains. There is an ordering of the B-sites of adjacent unit cells, giving rise to additional superstructure peaks in the diffraction pattern at the $(h+1/2, k+1/2, l+1/2)$ positions. The size of the chemically ordered domains can be varied by doping: substituting La on the Pb site (La-PMN) causes the ordered domain size to be increased. Doping with Ti on the B-site (PMN-PT) causes the ordered domain size to be decreased. The effects of both on the materials' structure and dielectric behavior will be measured.

The existence of a superstructure in PMN was first observed in selected area electron diffraction experiments [12]. Using a transmission electron microscope, superstructure spots were imaged at the $(h+1/2, k+1/2, l+1/2)$ positions. The peaks were relatively weak and broad, suggesting that they originated from limited domain sizes. Because the half-integer peaks are at the body centered positions in the reciprocal lattice,

the symmetry of the superstructure must have a face centered cubic arrangement within a doubled unit cell in real space (space group Fm3m). This work focuses on understanding the structural origin of the superstructure spots in PMN and PZN which could not be deduced from the electron diffraction measurements.

First, the cause of the superstructure peaks must be determined. One type of model that would give superstructure peaks at the $(h+1/2, k+1/2, l+1/2)$ positions is displacement ordering. In this class of models, atoms in adjacent unit cells are displaced in opposite directions, producing a doubled unit cell. If the displacement is Δd , and adjacent atoms are displaced in opposite $\langle 111 \rangle$ directions, then the structure factors will have the form:

$$F_{hkl} \propto f \sin(q \cdot \Delta d) \quad (\text{when } h,k,l \text{ are integers} + 1/2) \quad (1)$$

The graph of structure factor, $|F|$, of the superstructure peaks versus momentum transfer, $|q|$, would initially increase, passing a maximum when $q=\pi/(2\Delta d)$, and then decrease. This was the observation for PMN in the study by Zhang et al [13], and hence they concluded that an ordering in the displacement of ions was producing the superstructure.

4.2.1 Chemical ordering--space charge

Another model that could account for these superstructure peaks involves small regions of 1:1 chemical ordering of the B-site magnesium and niobium ions (Figure 4.1). This was first proposed in TEM studies [14], but could not be verified. The 1:1 ordering found in PMN is somewhat unexpected given the Mg:Nb stoichiometry of 1:2, but it was suggested that this non-stoichiometric ordering may actually help stabilize the perovskite

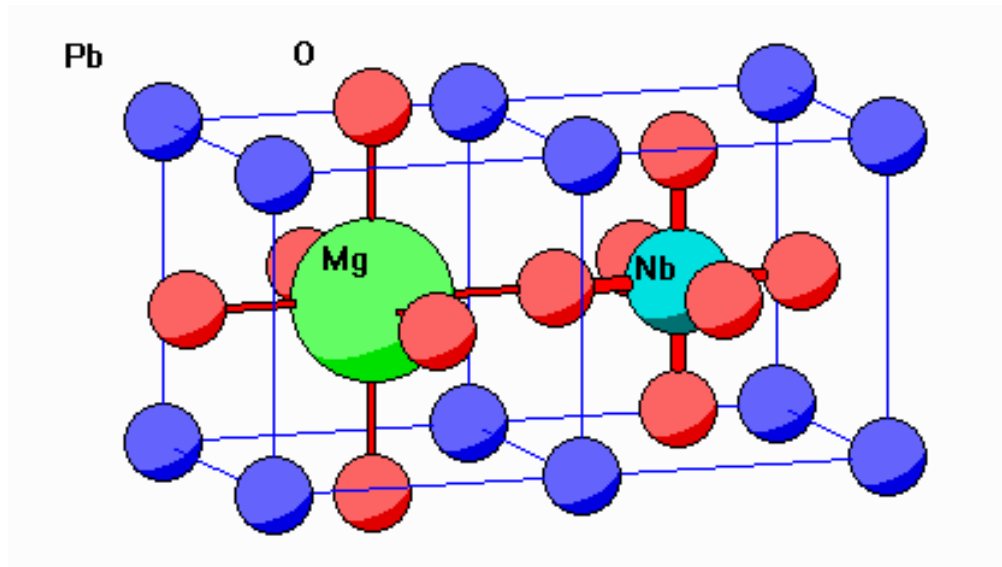


Figure 4.1. Two adjacent unit cells of PMN showing the 1:1 chemical ordering as in the space charge model. In addition, the oxygen displacements in the $R\bar{3}m$ model are shown.

over the pyrochlore structure in PMN[15]. The non-stoichiometric domains would then be embedded in a sea of Nb rich domains. The ordered domains have a net negative charge which, it was proposed, restricts their size since these domains did not coarsen after annealing at 970°C for extended periods [16]. Chen, Chan and Harmer provided evidence for this model in their study [10]. By doping with La^{3+} , they showed that the size of the ordered domains can be dramatically increased. The La^{3+} ion contributes an extra positive charge compared with the Mg^{2+} thus lessening the charge restriction so the negatively charged ordered domain can increase in size. The opposite effect was seen when doping with Na^{1+} . Because of the net charge per unit cell, this model is termed “space charge.”

4.2.2 Chemical ordering--random layer

A variation of the complete chemical ordering model that maintains charge balance is the “random layer” model [10], in which the 1:1 ordering is between two chemical species, B' and B''. The “random layer” model also involves 1:1 chemical ordering, but not a simple Mg-Nb-Mg-Nb ordering. In this model, B' contains a random occupation of Mg and Nb ions in a 2:1 ratio, while B'' is always Nb. Thus the B' site is disordered, while B'' is ordered, so the superstructure is well-defined. In this extreme case, there would be no charge imbalance and the entire crystal volume could be composed of these ordered domains with the chemical formula: $\text{Pb}[(\text{Mg}_{2/3}\text{Nb}_{1/3})_{1/2}\text{Nb}_{1/2}]\text{O}_3$. Intermediate situations between the full 1:1 Mg:Nb chemically ordered model and the B' - B'' model can exist, with different volume fraction of the ordered domains.

The above descriptions result when adjacent unit cells have sites either occupied by different ions or with a preference for different types of ions. Effectively, this doubles the size of the unit cell, producing a superstructure that exists over small domains. A diffraction experiment is a good way to probe the degree of ordering through crystallographic analysis of structure factor measurements. If the two B-site ions have effective atomic form factors f_I and f_{II} , then a simple derivation gives the form of the structure factors as a function of momentum transfer magnitude, $|q|$:

$$F_{hkl} \propto f_I - f_{II} \quad (\text{when } h,k,l \text{ are all half-integers}) \quad (2)$$

So, for chemical ordering models, the intensity of the superstructure reflections depends on the difference in form factor of the two chemical species, and hence gradually decreases as a function of momentum transfer, $|q|$, according to the shape of atomic form factors. In the complete chemical ordering model, this results in F_{hkl} being proportional to

$f_{\text{Nb}} - f_{\text{Mg}}$. In the random layer model, B' is an average ion of $(\text{Mg}_{2/3}\text{Nb}_{1/3})$ and B'' is Nb, so the resulting structure factor is identical except for a factor of 2/3:

$$F_{\text{hkl}} \propto f_{\text{Nb}} - \left(\frac{2}{3}f_{\text{Mg}} + \frac{1}{3}f_{\text{Nb}}\right) = \frac{2}{3}(f_{\text{Nb}} - f_{\text{Mg}}) \quad (3)$$

which makes the two chemically ordered models indistinguishable in the diffraction pattern, unless measurements are made on an absolute scale. Compared with the displacement ordering model, however, the behavior is quite different.

Evidence for the “random layer” model in $A(\text{B}'_{1/3}\text{B}''_{2/3})\text{O}_3$ systems was recently reported by Akbas and Davies [11] who found greatly increased ordered domains in $\text{Pb}(\text{Mg}_{1/3}\text{Ta}_{2/3})\text{O}_3$ and similar ceramics by annealing to very high temperature ($\sim 1325^\circ\text{C}$). This is strong evidence that the “random layer” model applies to that system because the excess electrostatic energy in such highly ordered systems would make the “space charge” model impossible (discussed in Section 4.4.4 below). However, similar annealing experiments for extended periods have failed to coarsen the ordered domains of PMN.

By comparing the superstructure and bulk intensities, Lin and Wu [17] found in powder diffraction experiments that for La concentrations greater than 10%, there is maximum ordering on the B-sites. However, at 10% La content and below the superstructure peaks were very weak. Their plot of lattice constant vs. La content (x) fits a straight line for $x > 10\%$, suggesting complete solid solutions are formed between the La and Pb atoms. For $x < 10\%$ the lattice constant deviates from the fit, suggesting a more complicated structure. This work focuses attention on the La concentration range below 10%, where the powder diffraction could not give reliable results on ordering. Single crystal X-ray diffraction also can determine the structure of the ordered domain, so atomic displacements can be measured. By doping with La, the effect of increased ordered

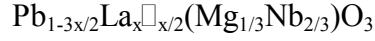
domain size on the atomic structure and dielectric behavior can be studied. By doping with Ti, the opposite effect of decreased domain size will be examined.

The organization of this chapter is as follows. First, the crystal growth procedure is described. Then, the crystallographic analysis and refinement of the structures for PMN and La-PMN allow the size and structure of the ordered domain to be determined for each sample. Next, the electrostatic energies involved with the various models are estimated and it is seen that the space charge model can not explain the doping trends. An alternative analysis shows that internal strain effects may be driving the chemical ordering. In addition, it is found that the random layer model must be present in the La-doped samples. An interpretation of the relationship between ordered domain size and relaxor behavior is given. Experiments on Ti doped crystals demonstrate the opposite effect of La-PMN and provide further evidence of the interplay between chemically ordered and polar domains. Finally, similar experiments on the PZN system are described to back up the conclusions drawn from the PMN experiments.

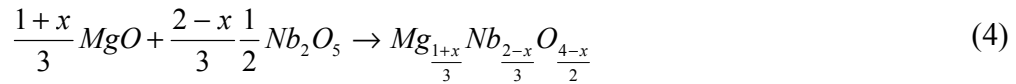
4.3 Crystal growth

Crystals of pure PMN and PMN-PT of roughly 2 mm per side were used. These crystals were grown using the Czochralski method [18]. One PMN crystal was as grown, with well formed $\langle 100 \rangle$ faces on three sides. The other PMN crystal and the PMN-PT crystal were cut from larger crystals and polished so that the largest face was $\langle 100 \rangle$. Lanthanum doped crystals were grown for this experiment using high temperature solution growth. First, La-PMN powder was prepared using the columbite method described by Swartz and Shrout [19]. Powders of PbO, MgO, Nb₂O₅, and La₂O₃ with purities

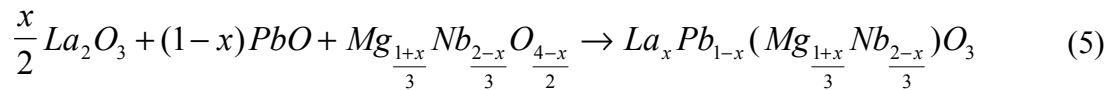
exceeding 99.7% were used. When doping with La^{3+} for Pb^{2+} , it is necessary to account for the charge imbalance in one of two ways. By keeping the ratio of Mg:Nb concentration fixed, A-site vacancies can be introduced:



where □ represents a vacancy. For this work, however, the Mg:Nb ratio was increased to prevent A-site vacancies, as seen in equations 4 and 5. The columbite phase was produced by heating the magnesium and niobium oxides to 1000°C for 6 hours:



This was then combined with appropriate amounts of La_2O_3 and PbO :



The La-PMN powder was then formed by firing to 850 °C for 6 hours. X-ray powder diffraction confirmed the resulting perovskite structure (Figure 4.2). The most common problem with growing PMN is obtaining the pyrochlore structure instead of perovskite. Pyrochlore is a non-cubic, isometric structure with excess oxygen and niobium and its material properties are nothing like perovskite PMN.

Single crystal growth involved combining La-PMN powder with a lead oxide flux. The amount of flux ranged from one to one and a half times the weight of the PMN powder. The mixture was placed in a tightly covered platinum crucible, and placed in a

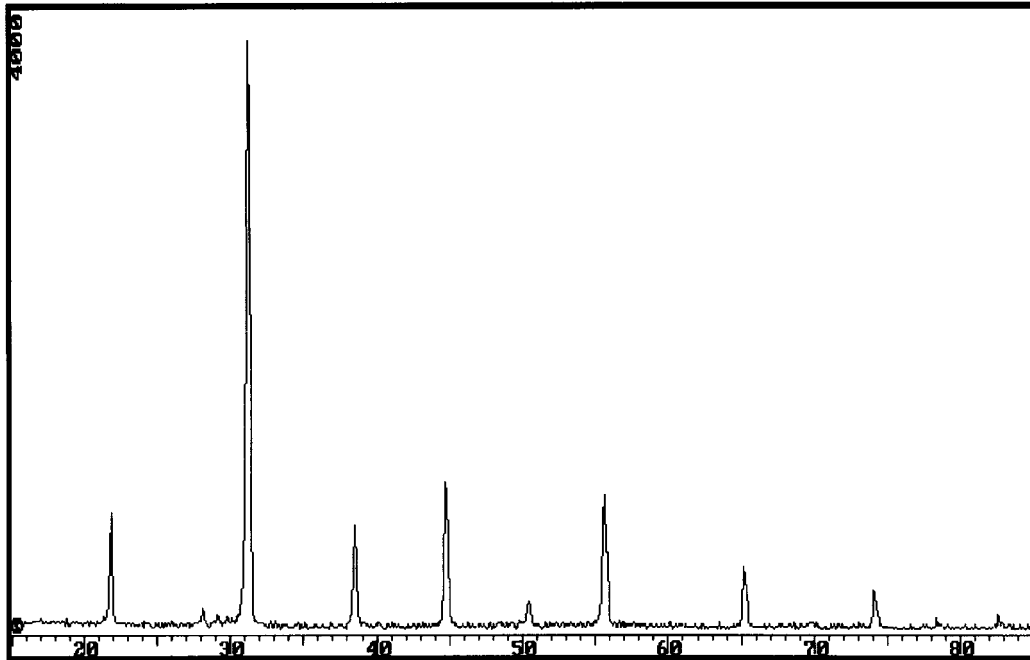


Figure 4.2. Powder x-ray diffraction scan of intensity vs. 2θ for pure PMN with the perovskite structure. After confirming the perovskite structure is present, single crystal growth can be attempted.

larger crucible. Alumina powder surrounded the platinum crucible to help prevent lead loss upon firing. A typical firing schedule involved rapid heating to 1250°C , soaking for 12 hours, then slow cooling at 2° per hour to 1000°C . Cooling continued at 5° per hour to 800°C , and then the mixture was brought to room temperature at 50° per hour. These temperatures were based on the PbO-PMN phase diagram published by Ye et al [20]. The residue was partially dissolved with boiling nitric acid, and single crystals were extracted. In all trials, only small crystals were found. The largest 3% La-PMN crystals were approximately 1 mm per side, while the 10% La-PMN crystals were only about 0.5 mm per side and some were black in color which may have been due to Pt contamination from

the crucible. It was helpful to polish these crystals to give them a well defined, flat face for the X-ray diffraction measurements.

The growth of PZN and La-PZN was easier, as the columbite step was not needed. Appropriate amounts of powder were ball milled and ground, and a PbO flux of one and a half times the La-PZN powder weight was used. The mixture was placed inside a Pt crucible (sealed as above), rapidly heated to 1300°C and then soaked at 1250°C for 12 hours. Single crystal growth occurred under slow cooling at 2° per hour to 800°C. The resulting crystals were on the order of 1.0-1.5 mm per side for both pure PZN and 10% La-PZN, and powder diffraction confirmed the perovskite phase. The irregularly shaped crystals were polished to a flat face for the X-ray and dielectric measurements.

4.4 Lanthanum doped PMN

4.4.1 Measurements

Each crystal was oriented in the diffractometer with one of its flat faces aligned nearly perpendicular to the phi axis [21]. This made it easier to estimate, and hence correct for, the beam's penetration through the crystal at any angle. This face was always close to a $\langle 100 \rangle$ orientation, which was designated (001). Measurements were taken at Brookhaven National Laboratory's National Synchrotron Light Source on Beamline X16C. The incoming X-ray beam was tuned to 8.5 keV and focused onto a flat face of the crystal. The beam size was defined by slits to be 1×1 mm. The linear absorption coefficient for PMN at 8.5keV is approximately 1150 cm^{-1} , giving a characteristic penetration depth of 8.7 microns along the beam direction. The detector arm's slits were set at 2x2 mm to define the resolution function. The orientation matrix of the crystal was determined by

measuring several bulk Bragg reflections. The refined lattice parameters were $4.048(2) \text{ \AA}$ for pure PMN, in agreement with published values [22]. The lattice constants steadily decrease with increasing La concentration, due to the smaller ionic radius of La compared to Pb.

Scans were made to measure the integrated intensities of the $(h+1/2, k+1/2, l+1/2)$ superstructure peaks. Because of the big differences in domain size, and hence peak profile, two different methods were needed. The well-ordered crystals (10% La doping) used conventional rocking curves in theta. The less well-ordered samples were measured by reciprocal lattice scans varying one of the indices (Figure 4.3). These peaks were much broader than the resolution function, so it was necessary to integrate them in three dimensions. Initially, separate measurements along the h , k and l directions were made, but since the widths (in reciprocal lattice units) for each direction were approximately constant and independent of the direction scanned, it was sufficient to scan in only one direction. The integrated intensity was measured as the area under the peak minus the interpolated background. After adjusting for the counting time and the step size in h , the intensities were corrected for absorption as described in the following section. Taking the square root gave a measurement that was proportional to the absolute value of the structure factor, $|F|$.

Dielectric data were also measured for the La-PMN crystals. The dielectric response was recorded using a Hewlett-Packard (HP) 4284A inductance-capacitance-resistance (LCR) bridge, which can cover a frequency range between 20 and 10^6 Hz. For low temperature measurements, the samples were placed in a Delta Design 9023 test

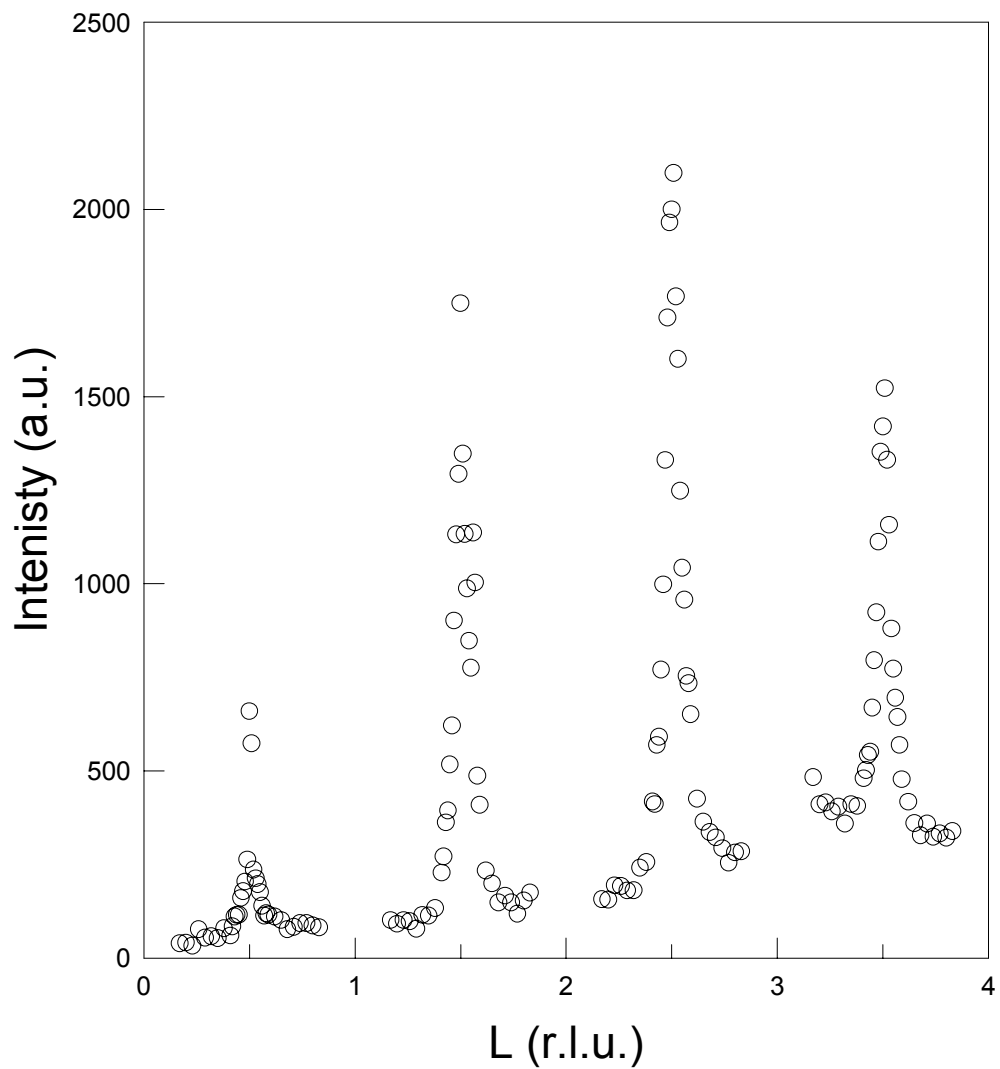


Figure 4.3. Raw x-ray diffraction data showing the intensities of four adjacent superstructure peaks. Scanned in the Miller index l , with $h = k = 0.5$.

chamber. The temperature was measured using a HP 34401A multimeter, via a platinum resistance thermometer mounted directly on the ground electrode of the sample fixture. The complex dielectric constant function is written as: $\epsilon = \epsilon' + i \epsilon''$ where ϵ' is the DC dielectric constant, and ϵ'' is the dielectric loss. Measurements were performed on cooling, using a rate of 2° per minute at different frequencies. The results for the La-doped samples are presented in Figure 4.4, with measurement frequencies from 1 to 500 kHz. By doping with La^{3+} , the dielectric constant $\epsilon'(T)$ peak becomes broader and its maximum value decreases dramatically compared to pure PMN (Table 4.1). Doping with La causes the peak in the dielectric constant to move to lower temperatures. Typical of relaxors, as the measurement frequency increased, the peak decreased and shifted to higher temperatures with dispersion in ϵ' and ϵ'' . ϵ' decreased with increasing frequency on the low temperature side of the peak, whereas ϵ'' increased with increasing frequency on the high temperature side of the peak, characteristic of relaxor behavior. At higher temperatures, (~ 350 K) the decrease in ϵ'' observed with increasing frequency can be attributed to thermally stimulated conductivity effects, i.e. charge transport rather than local charge displacements, possibly due to the small size of the crystals. The frequency dependence shows a larger frequency dispersion than pure PMN, indicative of more relaxor like behavior.

Table 4.1. Summary of domain size and dielectric constant data measured for the samples with different La^{3+} doping concentrations. Increases in La^{3+} led to much larger ordered domains and smaller dielectric constants.

Sample	avg. FWHM (\AA^{-1})	Domain size (\AA)	ϵ' max. at 1 kHz	Temp. (C) of ϵ' max.
PMN I	0.124	47		
PMN II	0.118	50	30,000	-5.0
3% La-PMN	0.0746	130	7,600	-45.0
10% La-PMN	0.00647	910	1,200	-63.0

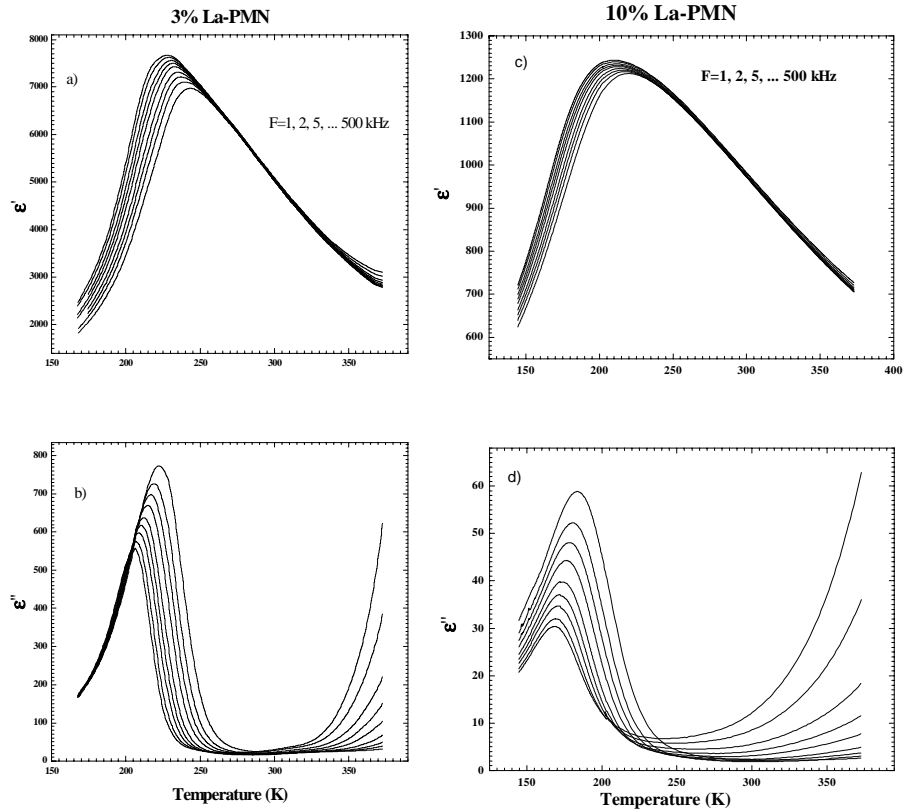


Figure 4.4. Dielectric constant, ϵ' , (a,c) and loss, ϵ'' (b,d) measured on the 3% (a,b) and 10% (c,d) La-PMN crystals as a function of temperature. Measurement frequencies range from 1 to 500 kHz and increase from left to right in each graph.

4.4.2 Analysis

The symmetry and structure of the parent crystal is assumed to be ideal cubic perovskite. By crystallographic analysis of peaks of the form $(h+1/2, k+1/2, l+1/2)$, the nature of the superstructure can be determined and hence the mechanism of ordering. Approximately 150 superstructure reflections were measured for each crystal. For each reflection, at least four symmetrically equivalent peaks were measured (e.g. $\pm 0.5, \pm 0.5, 0.5$). Only peaks with $\chi > 30^\circ$ [21] were measured to keep the entrance and exit beams passing through the alignment face. By averaging over the symmetrically equivalent scans, the 150 measured peaks were reduced to 19 crystallographically distinct reflections (of a possible 21 below the two-theta limit). This was a sufficient number to determine the structure of the ordered domains and observe changes with La or Ti doping. The agreement within the symmetry equivalent peaks was best for the larger pure PMN crystals at 7.8%. For 3% La-PMN, it was 14.1%, for 10% La-PMN it was 18.1%, and for 6% PMN-PT it was 8.1%. The larger errors are most likely due to the smaller crystal size and ill defined faces in the La-PMN which introduced errors through the absorption correction.

The general shape of the raw data agrees with that of Zhang et al [13], in that it appears to show a sinusoidal variation with $|q|$ (Figure 4.3). This suggests a displacement ordering model. However, there are important corrections needed to deduce structure factors from the raw data which change the conclusions significantly. The absorption of the beam as it passes through the Pb-rich sample must be accounted for. The size of the beam (~ 1 mm) is slightly smaller than the pure PMN crystals and larger than the La-doped

samples. At angles above a threshold incidence angle, the entire beam hits the pure PMN crystal. This is the extended face regime in which the integrated intensity is shown by Warren [23] to be proportional to:

$$\int_{z=0}^{\infty} e^{-2\mu z/\sin\theta} \frac{A_0 dz}{\sin\theta} \quad (6)$$

This assumes an “infinitely” thick crystal and a beam whose footprint is smaller than the crystal’s horizontal dimension. Here μ is the absorption coefficient, A_0 is the area illuminated, θ is the incident angle, and z is the penetration of the beam into the crystal. The integral evaluates to $1/2\mu$, so the effect of absorption is just a constant factor because even though it increases with increasing path length at smaller incidence angles, the illuminated area of the crystal also increases.

However, below that threshold angle (and at all angles for the smaller crystals), the extended face geometry is no longer valid because the beam footprint is now larger than the crystal. The absorption must be accounted for by adjusting for the fraction of the beam that is illuminating the crystal which depends on the incidence angle, α_i . This illumination correction is given by $1/\sin(\alpha_i)$, or $1/\sin(\theta)\sin(\chi)$, which is the footprint of the beam on the sample following the angle convention of Busing and Levy [21] when the flat face of the sample is perpendicular to the phi axis. This correction is significant for structure factors measured at low incidence angles and mostly affects the low $|q|$ reflections. The extended face absorption correction has to be adjusted because some fraction of the beam never hits the crystal. This illumination correction is only valid for crystals with a flat face, and when the x-rays that reach the detector enter and exit through that face symmetrically as was the case in these measurements. Because of the

large absorption of PMN, most radiation entering a side of the crystal would not contribute to the intensity anyway. Initially, the smaller 10% La-PMN crystals were studied in their as-grown, jagged state. Large errors were found in the scattering intensities in that symmetrically equivalent peaks had very different intensities. By polishing the crystal down to a flat face, this problem was largely eliminated.

The width of an X-ray peak is inversely proportional to the size of the domain that is contributing to that particular scattering event as given by the Scherrer formula:

$$L = 0.94 \frac{2\pi}{\Delta q_{\text{FWHM}}} \quad (7)$$

where L is the characteristic length of the ordered region and Δq_{FWHM} is the peak width measured in reciprocal space. By measuring the widths of half-order superstructure peaks, it is therefore possible to estimate the size of the ordered region. The average size of the domains that caused the superstructure peaks was 48 Å for both pure PMN samples, based on an average width of 0.12 Å⁻¹. The peak widths for various reflections were constant when measured in momentum transfer units (rather than angle) which indicated that the width was entirely a finite-size effect and had little contribution from the sample mosaic spread.

For the La-doped case, there was a dramatic increase in ordered domain size with increasing La doping (Table 4.1). The 10% La concentration produced ordered domains of approximately 900 Å. The peaks were so narrow that they were close to the limits of resolution, which is why the θ -scan integration method was used. In the 6% PMN-PT sample, the opposite effect was seen and the ordered domains were only on the order of 30 Å per side. Very faint superstructure reflections were also observed in 10% PMN-PT

but were too weak to do a complete analysis. This is closer to the morphotropic phase boundary where PMN-PT changes from a relaxor to a normal ferroelectric and the chemically ordered domains disappear.

4.4.3 Results

The absorption corrected data show a very different q -dependence from the raw data (Figure 4.5). The graph of structure factor vs. $|q|$ follows the monotonic decay (similar to the shape of atomic form factors) that is characteristic of the chemical ordering models. This was true for all the crystals that were studied. Using a simple chemical

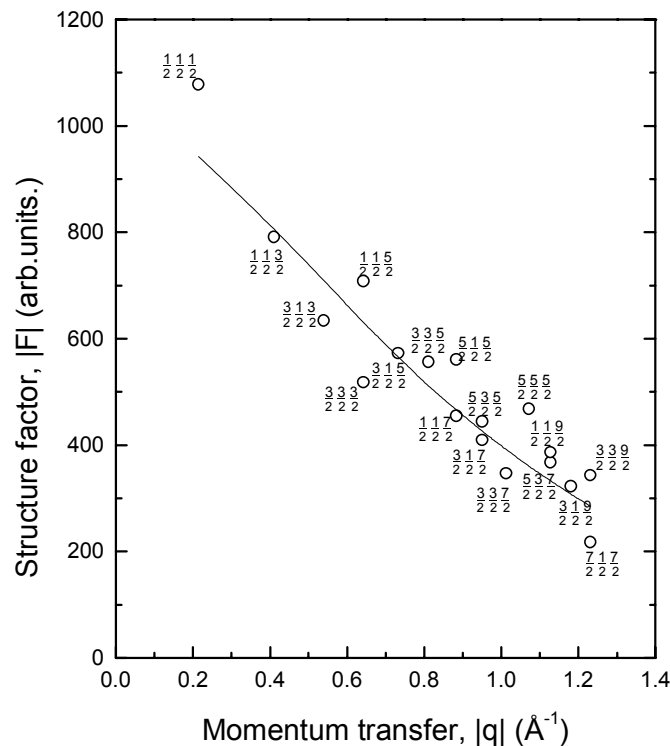


Figure 4.5. Structure factors (after corrections) vs. momentum transfer for superstructure reflections of pure PMN. The fit is to a simple chemical ordering model with no displacements..

ordering model, it is possible to fit the general shape of the data (line in Figure 4.5). However, chemical ordering alone gives the smooth line of the form factor difference between Mg^{2+} and Nb^{5+} (eqn. 2), and is not able to explain the small, systematic variations seen in the data. For example, certain pairs of reflections, with different indices but the same magnitude of $|q|$, have different structure factors. This simple fit results in a large chi-squared of 3.6.

By varying the position or shape of the oxygen octahedra that surround the B sites, it was possible to fit the deviations from the smooth curve. One such model, with $R\bar{3}m$ symmetry, was suggested by Husson et al [24] in a study of other perovskites, and a similar model was used to fit the data presented here. For the sake of simplicity, complete 1:1 chemical ordering between the B-site ions within each ordered domain (“space charge” model) was assumed, but the model would apply equally well to the charge balanced random layer model since the structure factors only differ by a multiplicative factor as explained above. Because there is no absolute scale factor in the model and the oxygen displacement is a small perturbation of the structure, the degree of 1:1 ordering on an absolute scale could not be measured. In the $R\bar{3}m$ model, the oxygen atoms move towards the smaller Nb^{5+} ions along a $\{100\}$ axis (and hence move away from the Mg^{2+} ions) (Figure 4.1). This oxygen displacement enabled the model to fit variations in structure factor for reflections that have the same magnitude of $|q|$, for example reflections (1.5, 1.5, 1.5) and (0.5, 0.5, 2.5). By fitting only the size of this oxygen displacement and assigning Debye-Waller factors to the Mg/Nb and O atoms, an optimal oxygen displacement of 0.044(3) Å for pure PMN was found. The improved fit (Figure 4.6) has a

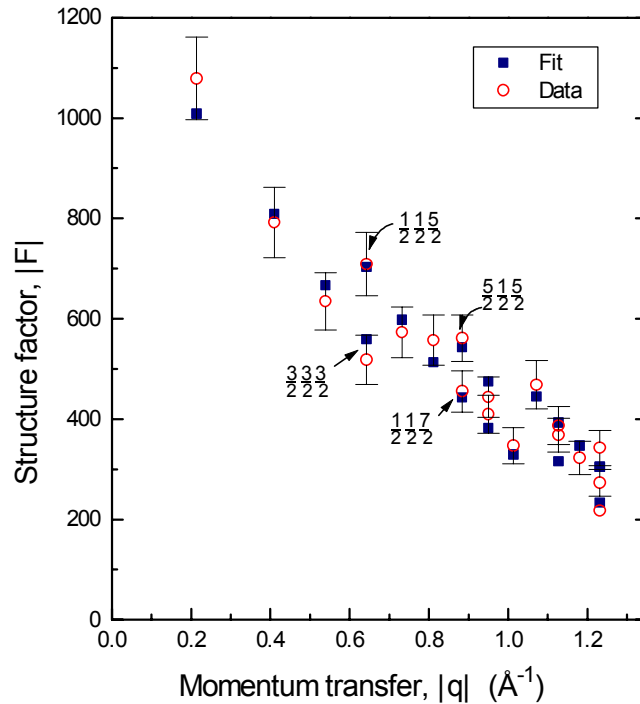


Figure 4.6. Improved fit using the $R\bar{3}m$ model and an oxygen displacement of 0.044 Å. This same model was also used to fit the doped PMN samples.

χ^2 of only 0.6. Models involving rotations of the oxygen octahedra were also attempted but they did not improve the fit. The same model was used to fit the data for the doped crystals. The resulting oxygen displacements are graphed in Figure 4.7 together with the lattice constant dependence. The chi-squared values were 0.9 for 3% La-PMN and 1.2 for 10% La-PMN. The 6% PMN-PT had an oxygen displacement of 0.024 Å, similar to 10% La-PMN, with a chi-squared of 1.4. The direction of the displacement in each case is in the direction towards the smaller Nb ions, as expected. Due to the low sensitivity of x-

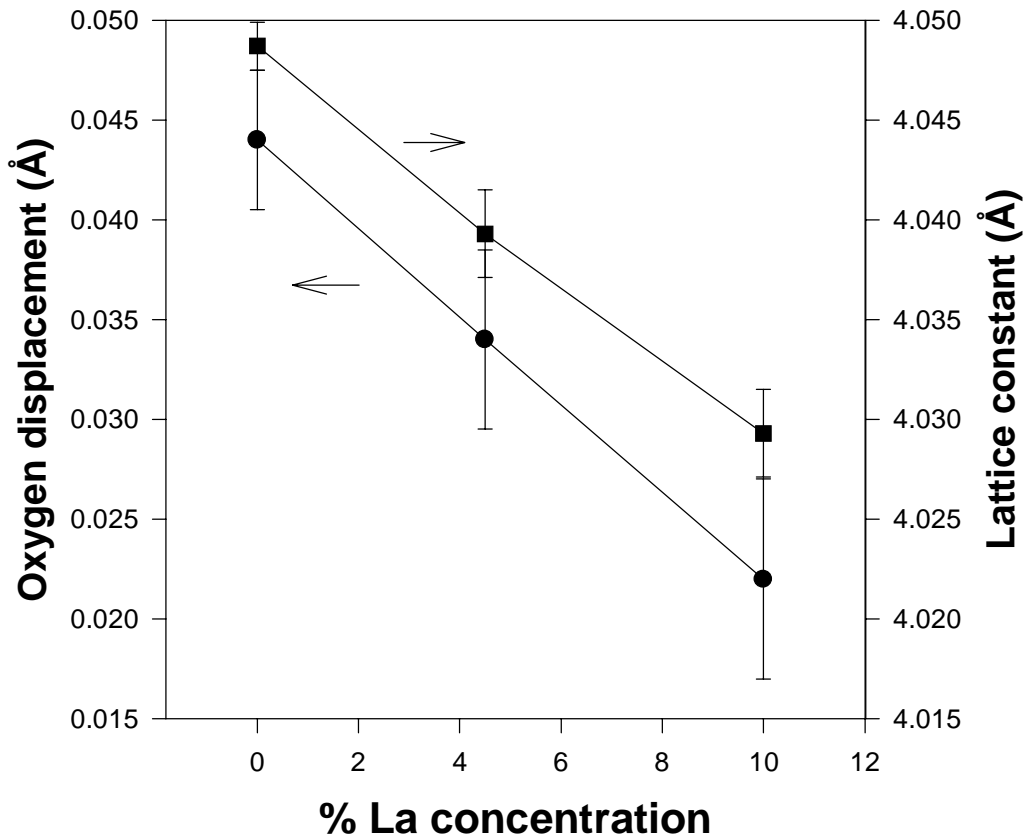


Figure 4.7. Oxygen displacement and lattice constant as a function of La doping. The displacement was found by fitting to the $R\bar{3}m$ model and is towards the Nb or B'' site.

rays to oxygen, additional oxygen rotations cannot be ruled out. However, the important result is the observed shrinking of oxygen displacements with increasing La doping.

These results indicate that chemical ordering is the dominant cause of PMN's superstructure peaks. The ordered domains have an average size of 48 Å per side and were not strongly anisotropic, so it is assumed they are roughly cubic in shape. These chemically ordered domains are believed to be distinct from PMN's nanopolar domains because they have different characteristics. The superstructure peaks that arise from the ordered domains showed no response to applied electric fields up to 2 kV/cm in our experiments, and they are also unaffected by temperature up to 1325°C [25]. The nanopolar domains, which appear when PMN is cooled, grow in size when temperature is

lowered and are responsible for PMN's ferroelectric properties. Chemically ordered domains are not affected by temperature, increase with La doping and their growth causes a decrease in the dielectric response (Figure 4.4). Doping with Ti (Section 4.2) causes the volume of polar domains to grow as PMN becomes more like a normal ferroelectric. This growth is accompanied by a decrease in the ordered domain size, again showing the competition between two different types of nanodomains in PMN.

Contrary to experiments on other mixed B-site relaxors [26], the increased B-site ordering in PMN results in more relaxor-like behavior as seen in the increased dispersion and broader peak of dielectric constant. It appears that PMN's relaxor behavior is not dependent on the heterogeneity of the B-site but rather the interference caused by the two types of nanodomains. The polar nanodomains' inability to coarsen into larger domains gives PMN its relaxor behavior. As the chemically ordered domain size increases (through La doping), the separation between the polar domains must also increase. The added frustration then increases the relaxor behavior, as observed in the dielectric measurements. In addition, the increase of ordered domains occurs at the expense of the total volume of polar domains as seen in the reduced maximum dielectric constant. Conversely, as Ti is added, it is observed that the maximum dielectric constant increases while the ordered domain size decreases. The result is that PMN begins to behave more like a normal ferroelectric as the interference of the chemically ordered domains is removed. Thus, the relaxor behavior can be understood as resulting from frustration of the polar nanodomains caused by the domains of chemical ordering. Increasing the chemically ordered domain size results in increased relaxor behavior, while decreasing it leads to decreased relaxor behavior. For lead titanate concentrations above 30%, PMN-PT transforms to a normal ferroelectric and the superstructure peaks are no longer present.

4.4.4 Charge imbalance models

In this section, the question of “space charge” vs. “random layer” model will be considered. The space charge model of complete chemical ordering is only possible for limited domain sizes because there is in fact twice as much Nb as Mg in the chemical composition of PMN. More importantly, the 1:1 Mg:Nb stoichiometry leaves a net charge per unit cell of $-0.5e$. Assuming the domain shape is cubic, the net charge of the cube can be calculated:

$$\text{Volume} = h^3 \quad Q = \left(\frac{h}{a_0}\right)^3 (-0.5e) \quad (8)$$

This net negative charge can be balanced by a surface layer of positive charge on the unit cells that enclose the ordered region. If such a layer were made up of unit cells of PbNbO_3 , then each surface unit cell would have a net positive charge of $+e$. By setting the surface layer charge equal to the volume charge, it is seen that 12 unit cells along each cube dimension are needed to achieve charge balance:

$$\left(\frac{h}{a_0}\right)^3 (0.5e) = 6\left(\frac{h}{a_0}\right)^2 (1.0e) \quad \frac{h}{a_0} = 12 \quad (9)$$

With a lattice constant of 4.048 \AA , this region would be 48.6 \AA per side. Thus, the observed domain size of 48 \AA in pure PMN is the minimum necessary so that one monolayer of unit cells of PbNbO_3 will counterbalance it. If this model is correct, then it can be concluded that these domains do not grow larger because they are strongly restricted by Coulombic forces.

The amount of electrostatic energy contained in such a charge imbalanced region of a crystal can be calculated in a straightforward manner [27]. Consider a spherical

volume of radius R containing a total charge Q uniformly distributed in a medium of relative dielectric constant ϵ_r . Again, a skin charge which counterbalances the volume excess charge and hence cancels all fields outside the sphere is assumed. The electrostatic energy is given by:

$$U = \frac{1}{10} \frac{Q^2}{4\pi\epsilon_r\epsilon_0 R} \quad (10)$$

Now, if there are N unit cells in the volume, each with an excess charge q , then $Q=N^3q$ and $R=Na_0$. Substituting gives:

$$U = \frac{1}{10} \frac{(N^3q)^2}{4\pi\epsilon_r\epsilon_0 (Na_0)} = \frac{1}{10} N^5 \frac{q^2}{4\pi\epsilon_r\epsilon_0 a_0} \quad (11)$$

The energy per unit cell is then given by:

$$u = \frac{U}{N^3} = \frac{1}{10} \frac{N^2}{\epsilon_r} \left(\frac{q}{e}\right)^2 (3.6eV) \quad (12)$$

This gives $(13/\epsilon_r)$ eV per unit cell in pure PMN, assuming $N = 12$ unit cells in the ordered region and complete chemical ordering ($q=0.5e$). Considering ϵ_r may be quite large, this energy is certainly not unreasonable on the scale of typical cohesive energies of ionic solids. The actual value of ϵ_r , which is the dielectric constant of the ordered region, is not known, but an approximation of about 100 can be made by extrapolating the Curie Weiss law to PMN's growth temperature. This results in $u \sim 0.13$ eV/unit cell for full chemical ordering in pure PMN.

It was proposed [10] that doping the Pb^{2+} sites with La^{3+} provides enough additional positive charge to allow these domains to become larger. However, at the quantitative level, doping with La does not provide enough positive charge to account for the rapid increase in the ordered domain size. Assuming that the La is distributed evenly

on the A-sites, then the net charge for one formula unit of $\text{La}_x\text{Pb}_{1-x}\text{Mg}_{0.5}\text{Nb}_{0.5}\text{O}_3$ is $(x-0.5)$ electrons per unit cell. As above, the number of unit cells per side of the ordered region is:

$$\left(\frac{h}{a_0}\right)^3 (0.5 - x)e = 6\left(\frac{h}{a_0}\right)^2 (1.0e) \quad \frac{h}{a_0} = \frac{6}{0.5 - x} \quad (13)$$

which has a weak dependence on x , giving only 15 unit cells, or 61 Å for 10 % La doping, which is nowhere near the observed 900 Å. It is possible that La goes preferentially into the ordered domains during growth, but no evidence for this was seen in comparing lattice constants of bulk and superstructure peaks.

The conclusion is that the “random layer” model is valid for sufficient La concentrations when the ordered domains are very large, but the “space charge” model is possible in the range below a few percent. Also, it is possible that the anomalous variation of lattice constant for La concentration less than 10% in the measurements of Lin and Wu [17] may indicate a transformation from “space charge” to “random layer” ordering.

4.4.5 Strain effect

A comprehensive explanation for why PMN chemically orders has not yet been given. The structural results presented above indicate that strain plays an important role. In perovskites, there is a delicate balance between ionic contacts at the A and B-sites. The relevant ionic radii, which vary with effective ionic charge and coordination number, are given in Table 4.2 [28]. In pure PMN, the lattice constant is 4.048 Å which, after accounting for two oxygen radii of 1.35 Å, leaves enough room to accommodate a B-site ion of radius 0.674 Å or smaller. Thus, the Nb⁵⁺ ion fits easily, but the Mg²⁺ ion is too large. However, by constructing a linear array of Nb⁵⁺ and Mg²⁺ ions (as in a 1:1 chemically ordered model) and displacing the oxygen atoms towards the smaller Nb ion, the Mg ion can be comfortably accommodated. The measurements of oxygen displacements are entirely consistent with this model. The combination of chemical ordering, with the associated oxygen displacements, may lower the total energy by reducing the strain and thereby drive the 1:1 chemical ordering. Doping with La³⁺ decreases the lattice constant, thereby increasing the internal strain by increasing the packing forces. This could make the chemically ordered state even more advantageous in

Table 4.2. Ionic radii from Shannon [28].

	Charge	Coord.	Radius (Å)
Pb	+2	12	1.50
La	+3	12	1.32
Mg	+2	6	0.72
Nb	+5	6	0.64
Ti	+4	6	0.60
O	-2	2	1.35

energy and result in increased ordering in La-PMN. In Chapter 5, an external strain is applied to PMN by growing thin films on a substrate that has a smaller lattice constant. In those measurements, the external strain also had the effect of increasing the ordered domains without having to dope with La.

As the overall lattice constant decreases with increased La^{3+} content, the size of the oxygen displacement also decreases (Figure 4.7). Both curves are on the same vertical scale, so it is seen that the two values change at an approximately equal rate. Using a hard sphere model and the ionic radii (Table 4.2), O-Nb-O requires 3.98 Å and O-Mg-O requires 4.14 Å. In pure PMN, using the measured oxygen displacement, the O-Nb-O bond length is 3.96 Å, and the O-Mg-O bond length is 4.14 Å, so that the Nb ion is being squeezed slightly, but the Mg ion fits exactly. As La is added, the data indicate that the measured O-Nb-O bond length remains approximately constant at 3.97 Å, while the O-Mg-O bonds become progressively more compressed. The displacements are such that the O-Nb-O distance is roughly constant, and all of the strain is concentrated in the O-Mg-O bond (Figure 4.8).

This result makes little sense in the context of a fully 1:1 Mg:Nb chemically ordered model. It makes more sense if the B', or 'Mg,' site is showing a change of composition with La doping. The smaller bond length may force the larger Mg out of the B' site, increasing the amount of Nb on B'. This brings the ordered domains closer to neutral charge because of the additional positive charge carried by Nb^{5+} on the B' site. In other words, the ordered domain changes from complete Nb:Mg ordering in pure PMN and becomes closer to random layer ordering of $\text{Nb}:(\text{Mg}_{2/3}\text{Nb}_{1/3})$ in 10% La-PMN. By this mechanism, the domain size is no longer limited by "space charge" and can grow larger. Also, because of the quadratic dependence of u on N (eqn. 12), the electrostatic

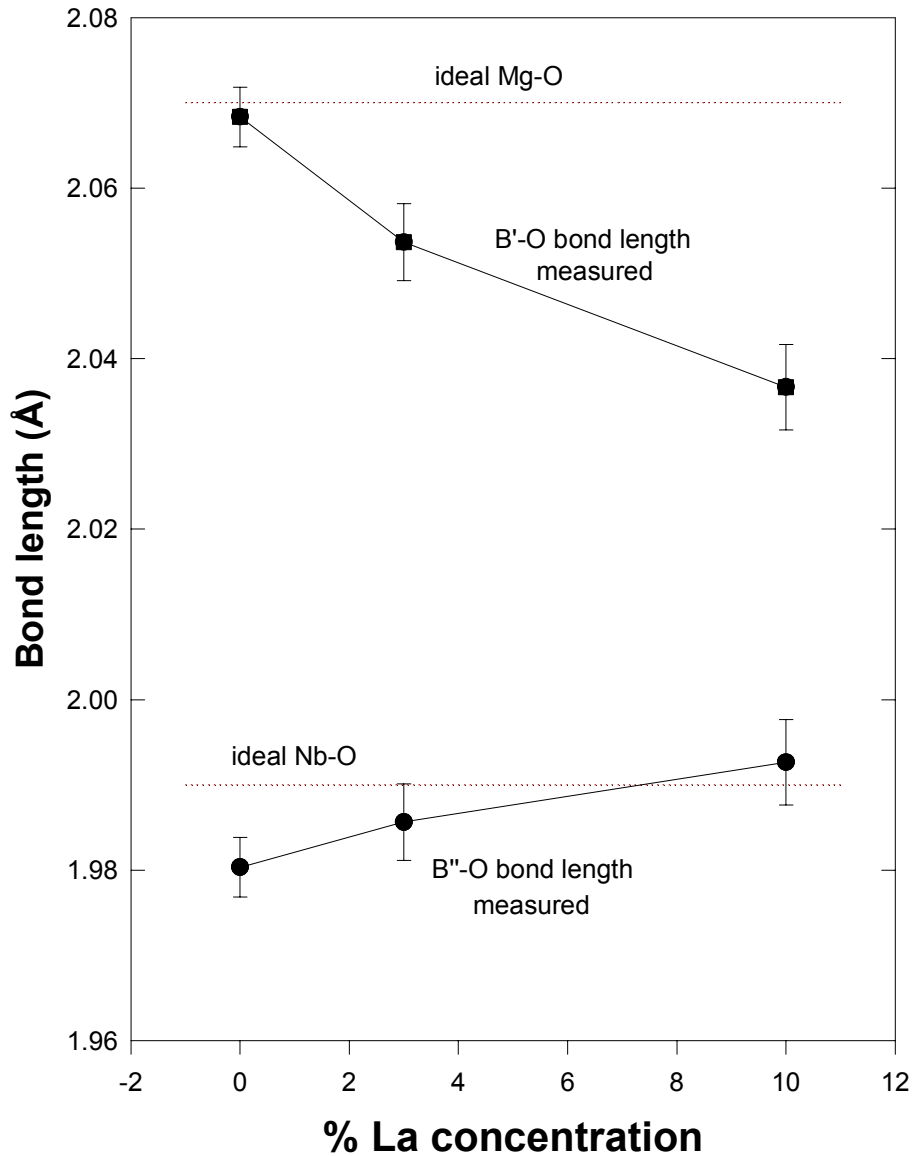


Figure 4.8. Calculated bond lengths of B'-O and B''-O as a function of La doping. In pure PMN, both Mg on the B' site and Nb on the B'' site can be accommodated, but as La is added, the B' site is squeezed suggesting a change in occupancy from pure Mg to a mixture of Mg and Nb.

energy becomes prohibitively large when N becomes larger. Hence, the charge redistribution on the B-sites is necessary to accommodate the large ordered domains in La-PMN.

The data can be interpreted using the model of changing stoichiometry to accommodate the shrinking B' site. Using the measured lattice constants, a_0 , and oxygen displacements, D_{Oxy} , the space allowed for the B' ion, R_B , is simply:

$$R_B = a_0/2 - R_{Oxy} + D_{Oxy} \quad (14)$$

where R_{Oxy} is taken from Table 4.2. A linear combination of the ionic radii, R_{Mg} and R_{Nb} , results in an effective radius. An independent estimate of the B' occupancy is made by calculating the fractions of Mg and Nb that result in an ion that matches the measured size:

$$R_B = y R_{Mg} + (1-y)R_{Nb}, \text{ giving } y = \frac{R_B - R_{Nb}}{R_{Mg} - R_{Nb}} \quad (15)$$

The results (Table 4.3) show good agreement for the pure PMN and 3% La-PMN, which have Mg occupancies of 0.98 and 0.79 respectively. For the 10% La-PMN, the Mg occupancy actually drops below the random layer model value of 2/3 (which would make the domain positively charged) but the value of 2/3 is still within the error estimate.

Table 4.3. R_B is the measured ionic radius that would fit in the B' site. The fraction of Mg, in combination with Nb, that corresponds to that size and the resultant excess charge per unit cell are shown.

% La in PMN	R_B measured (eqn. 16)	Mg fraction on B' site, y calc. (eqn. 17)	charge/unit cell q/e calculated
0	0.718±0.003	0.98±0.04	-0.46±0.06
3	0.704±0.004	0.79±0.06	-0.19±0.08
10	0.688±0.005	0.60±0.08	+0.10±0.12

Alternatively, the change in bond length could be due to the effects of the La dopant and/or the increased Mg:Nb ratio.

4.5 Titanium doped PMN

In the 6% PMN-PT crystals, the measured lattice constant was $4.033(2) \text{ \AA}$. This crystal was cut from a larger crystal and had a large polished face. Very good agreement of 6.7% was found within the symmetry equivalent peaks after making the corrections as described above for PMN. The same model was used to fit the data with a resulting oxygen displacement of $0.024(5) \text{ \AA}$. These measured values give a B' site that is 0.69 \AA and a B'' site that is 0.64 \AA . These values are also consistent with a “random layer” model with a Mg occupancy on the B' site of 63%. Apparently, the perturbation introduced by the Ti dopants (and the increased disorder on the B-sites) encouraged a random layer ordering, but over a smaller domain size. In the work of Davies et al [11], it was also found that small dopant levels led to greatly increased ordered domains after annealing and hence random layer ordering (the only type possible in large domains). Apparently the random layer ordering is preferred or more stable in these systems, but it must be induced by adding a dopant. It is possible that the ordered domains in PMN-PT could be increased in size by annealing to very high temperatures as was seen in [11].

In the as-grown crystals studied here, the ordered domain size was only about 30 \AA . This again suggests the competition between polar nanodomains and chemically ordered domains. As lead titanate is added to PMN, it becomes more like a normal ferroelectric with a larger dielectric response. This occurs at the expense of the ordered domains which in pure PMN interfere with the polar domains and give it the relaxor

behavior. The growth in dielectric constant and reduced relaxor behavior with the addition of PT is clearly seen in Figure 4.9 from Colla et al [29]. In Figure 4.9a, the transition region becomes narrower with increasing PT content, and Figure 4.9b demonstrates the reduced frequency dispersion with increased PT.

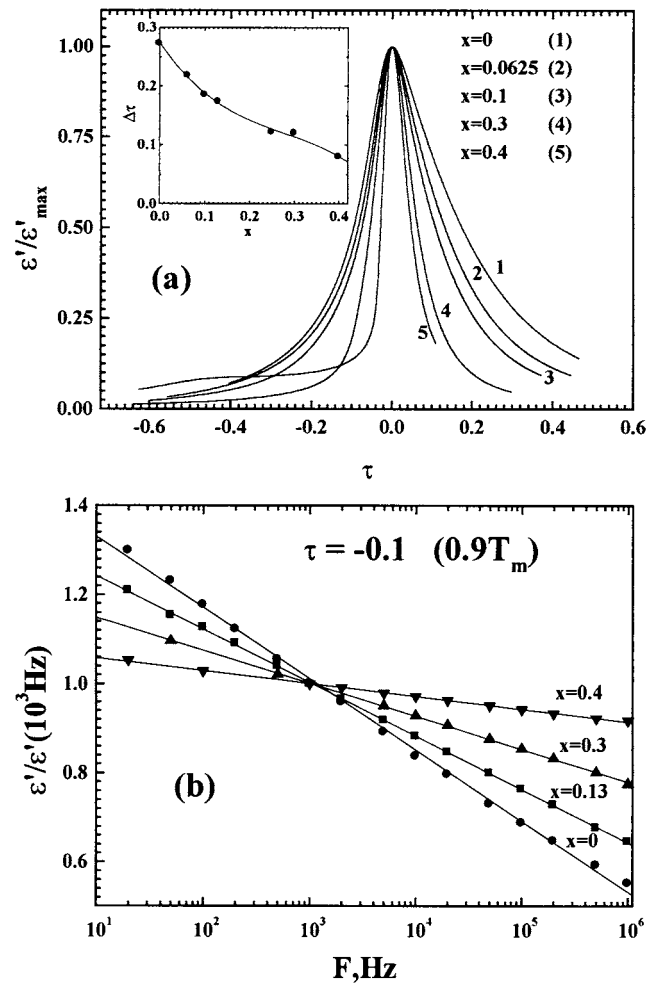


Figure 4.9. Dielectric behavior of PMN-PT for increasing amounts of lead titanate [30]. In a), the transition is seen to become narrower, and in b), the dispersion amount is reduced with increasing PT--becoming less relaxor like. τ is the reduced temperature, or $(T-T_C)/T_C$.

4.6 Lead zinc niobate

Dielectric data were measured for PZN and 10% La-PZN crystals using the same setup discussed above, and the results are presented in Figure 4.10. By doping with La, the $\epsilon'(T)$ peak again became broader and its maximum value decreased significantly. The La also caused the peak in the dielectric constant to move to lower temperatures. Typical

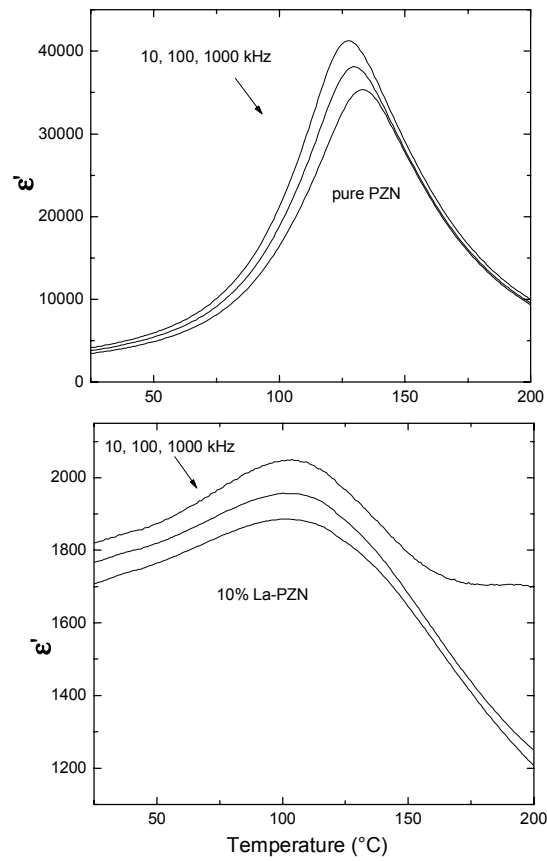


Figure 4.10. Dielectric constant behavior of PZN and 10% La-PZN. As with PMN, La doping leads to larger chemically ordered domains, reduced dielectric constant and increased dispersion (more relaxor like).

of relaxors, as the measurement frequency increased, the peak maximum decreased and shifted to higher temperatures. Again, the La dopant caused more relaxor-like behavior as

seen in the broader transition and greater frequency dispersion. The refined lattice parameters were 4.062(2) Å for pure PZN, and 4.049(2) Å for 10% La-PZN.

Integrated intensities of the (h+1/2, k+1/2, l+1/2) superstructure peaks of 10% La-PZN crystal were measured using theta scans. For 10% La-PZN, 90 such reflections were measured which resulted in 15 crystallographically distinct reflections after averaging symmetrically equivalent peaks. As with PMN, the observed drop off in structure factor with increasing momentum transfer indicated that chemical ordering was the dominant cause of the superstructure peaks in both PZN and 10% La-PZN. However, since the structure factor of chemical ordering superstructure peaks is proportional to the atomic form factor difference (eqn. 2), the PZN peaks from similar domain sizes would be seven times weaker compared with PMN (the form factor difference is 11 electrons between Zn and Nb versus 29 for Mg and Nb).

Using the Scherrer formula, the domain size of PZN was measured to be 25 Å versus the 50 Å found in PMN. This eight times smaller domain volume (without a significant increase in the number of domains), together with the smaller form factor difference, resulted in much weaker superstructure peaks for PZN compared to PMN. As a result, it was not possible to measure enough peaks to do a reliable crystallographic analysis. For the La-doped crystals, there was again a dramatic increase in ordered domain size, so it was possible to model the 10% La-PZN structure. The average ordered domain size of 10% La-PZN was 1200 Å, slightly larger than the 900 Å found for 10% La-PMN.

For 10% La-PZN, the $R\bar{3}m$ model was again used to fit the data. An oxygen displacement of 0.050(6) Å was found, considerably larger than the 0.022(3) Å that was

measured for 10% La-PMN. This larger displacement is expected given that Zn has an ionic radius that is 0.03 Å larger than Mg [28].

Analogous to PMN, it is possible to lend insight to what might be driving the chemical ordering in PZN by considering atomic size. As discussed above, only the random layer model is possible in the highly ordered La-doped crystals because of electrostatic considerations. In the random layer model for 10% La-PZN, the B' site of $Zn_{2/3}Nb_{1/3}$ has an average radius of 0.72 Å, and the B'' site (Nb) has an ionic radius of 0.64 Å. The measured lattice constant and oxygen displacement result in an allowed B' site of 0.72 Å and an allowed B'' site of 0.62 Å. Thus, the measured oxygen displacement was within 0.01 Å of a “perfect fit,” and the system could reduce internal strain by chemically ordering and displacing the oxygen ions.

PZN crystals doped with lead titanate were also grown and measured. As with PMN, the addition of lead titanate to PZN destroys the chemical ordering on the B-sites. Compositions near PZN-9% PT exhibited no half-order peaks. This composition sits on the morphotropic phase boundary above which PZN-PT behaves like a normal ferroelectric. As with PMN-PT, it was observed that the transition from relaxor to normal behavior is accompanied by the disappearance of the half-order peaks and hence the chemically ordered domains. Attempts were made to dope the PZN-PT with La to see if the superstructure could be restored. La dopants of 5, 10 and 20% were added to PZN-9% PT, and in each case the superstructure peaks were still found to be absent. This is further evidence that the drive to chemically order is related to strain effects. Adding smaller Ti ions frees up more space for the larger Zn and Nb ions. So, by reducing the internal packing strain, the drive to chemically order is reduced. Further, this also shows that chemical ordering is not necessarily enhanced by doping with extra positive charge.

4.7 Conclusion

PMN's superstructure peaks give an X-ray diffraction pattern that, when corrected for absorption and illumination, show decreasing structure factors with increasing $|q|$. Hence, chemical ordering is the dominant feature in PMN that causes its superstructure. The positions of the oxygen atoms were further refined, and it was shown that their displacements are towards the Nb ions and away from the Mg, or $(\text{Mg}_{2/3}\text{Nb}_{1/3})$, ions. The "space charge" model is possible in pure PMN, but the "random layer" model must be present in La doped PMN. While the increase in positive charge that La provides may facilitate the growth of 1:1 chemically ordered domains, it appears that strain effects are more important. These strain effects will be considered in a different fashion in the next chapter.

The increase of chemically ordered domains caused by La doping caused more relaxor-like behavior in PMN. The increase in ordered domains also caused a much lower ferroelectric response in La-PMN, demonstrating that the chemically ordered domains are not ferroelectrically active and are distinct from the polar domains. Conversely, a decrease in ordered domain size from Ti doping caused PMN to behave less relaxor-like with a larger dielectric constant. The interference between PMN's chemically ordered and polar nanodomains is believed to be responsible for its relaxor behavior.

4.8 References

[1] G A Smolenskii, A I Agranovskaya, *Sov. Phys. -- Tech. Phys.*, **3**, [7] 1380-82 (1958).

- [2] J Kuwata, K Uchino and S Nomura, *Jpn. J. Appl. Phys.* **21**, 1298, 1982.
- [3] N de Mathan, E Husson, G Calvarin, J R Gavarris, A W Hewat and A Morell, *J. Phys.: Condens. Matter* **3**, 8159-71 (1991).
- [4] M Mulvihill, L E Cross, W Cao and K Uchino, *J. Am. Ceram. Soc.* **80**[6], 1462, (1997).
- [5] N de Mathan, E Husson, G Calvarin, J R Gavarris, A W Hewat, A Morell, *J. Phys.: Condens. Matter*, **3**, 8159-71 (1991).
- [6] A Verbaere, Y Piffard, Z G Ye, E Husson, *Mater. Res. Bull.*, **27**, 1227-34 (1992).
- [7] S G Zhukov, V V Chernyshev, L A Aslanov, S B Vakhrushev, H Schenk, *J. Appl. Cryst.*, **28**, 385-91 (1995).
- [8] G A Smolenskii, *J. Phys. Soc. Jpn.* **28**, 26-37 (1970).
- [9] G A Smolenskii, A I Agranovskaya, *Sov. Phys. -- Tech. Phys.*, **1**, 1429 (1959).
- [10] J Chen, H M Chan and M P Harmer, *J. Am. Ceram. Soc.* **72** [4], 593-98 (1989).
- [11] M A Akbas and P K Davies *J. Am. Ceram. Soc.* **80** [11], 2933 (1997).
- [12] H B Krause, J M Cowley, J Wheatley, *Acta Crystallogr., Sect. A*, **35**, 1015-17 (1979).
- [13] Q M Zhang, H You, M L Mulvihill, S J Jang, *Solid State Communications*, **97** [8], 693-98 (1996).
- [14] A D Hilton, C A Randall, D J Barber, T R Shrout, *Ferroelectrics*, **93**, 379-86 (1989) and L A Bursill, H Qian, J-L Peng, X-D Fan, *Physica B*, **216**, 1 (1995).
- [15] D D Viehland, J-F Li, *Ferroelectrics*, **158**, 381 (1994).
- [16] A D Hilton, D J Barber, C A Randall and T R Shrout, *J. Mater. Sci.* **29**, 3461 (1990).
- [17] L-J Lin, T-B Wu, *J. Am. Ceram. Soc.*, **73** [5], 1253-56 (1990).
- [18] Commercially purchased.
- [19] S L Swartz, T R Shrout, *Mater. Res. Bull.*, **17**, 1245-50 (1982).
- [20] Z-G Ye, P Tissot, H Schmid, *Mater. Res. Bull.*, **25**, 739-48 (1990).
- [21] The standard angle conventions for a 4-circle diffractometer are given in Busing and Levy, *Acta Cryst.* **22** 457 (1967).

- [22] N de Mathan, E Husson, A Morell, *Mater. Res. Bull.*, **27**, 867-76 (1992).
- [23] B E Warren, *X-Ray Diffraction*, (Addison-Wesley, Massachusetts, 1969).
- [24] E Husson, M Chubb, A Morell, *Mater. Res. Bull.*, **23**, 357-61 (1988).
- [25] A D Hilton, D J Barber, C A Randall, T R ShROUT, *J. Mater. Sci.*, **29**, 3461-66 (1990).
- [26] L E Cross, *Ferroelectrics*, **76**, 241 (1987).
- [27] D J Griffiths, *Introduction to Electrodynamics*, (Prentice-Hall, New Jersey, 1989).
- [28] R D Shannon, *Acta Cryst.* **A32**, 751, (1976).
- [29] E V Colla, N K Yushin, D Viehland, *J. Appl. Phys.*, **83** [6] 3298 (1998).

Chapter 5

PMN Thin Films

5.1 Introduction

In order to better understand what was driving the 1:1 chemical ordering, experiments on PMN thin films were performed. In chapter 4, it was demonstrated that PMN's superstructure is due to chemical ordering on the B-sites. However, those experiments could not distinguish between complete chemical ordering of the Mg and Nb ions (space charge model) and ordering between Nb and a mixture of $(\text{Nb}_{2/3}\text{Mg}_{1/3})$ known as the random layer model. As proposed by Harmer et al [1], the space charge model was widely adopted and pretty much unquestioned until recently [2]. In that model, the small size of the ordered domains is limited by the charge imbalance and Coulombic forces, and doping with La^{3+} restores enough positive charge to allow those domains to grow.

From the experiments discussed in Chapter 4 using both La and Ti dopants, it appeared that internal strain or packing effects may also play an important role. Because La ions have a smaller radius than Pb atoms, their substitution produces additional constraints on the system. By reducing the lattice constant, the effect of the La is to generally shorten the bond lengths. Considering the ionic radii, it was shown that the Mg ion was slightly too large for the unit cell. By chemically ordering in a 1:1 fashion and displacing the oxygen ions away from the Mg ion, the system could better accommodate

the larger Mg ion and reduce the overall strain. Our crystallographic data confirm that this type of displacement was occurring. As more La was added, the bond lengths were further constricted, and the ordered domain size increased. Kim et al [3] found that doping the B-site of La-PMN with Cd induced large chemically ordered domains while doping with smaller Ni ions did not. They attributed this behavior to the larger ionic size difference of the B-site ions in the Cd doped sample, again suggesting that the desire to accommodate both large and small ions on the B-site is driving the chemical ordering.

In the space charge model, it is believed that the non-stoichiometric ordering of Mg and Nb ions occurs only in very small domains because of the Coulombic forces that develop in the net charged region. It was proposed that the La^{3+} dopant on the Pb^{2+} site provides additional charge to overcome those Coulombic forces and hence the ordered domains grow. This does not consider what effect the smaller ionic size of La has on the system. In this work, by depositing thin films of PMN on a substrate that has a slightly smaller lattice constant, it was possible to force PMN into a smaller unit cell volume via interfacial strain. Thus, the effects that reduced cell volume and constrained packing have on the ordering could be studied without simultaneously introducing extra charge.

In order to separate the question of the effects of higher valence from ionic radius, thin films of PMN were grown on a substrate which had a smaller lattice constant than bulk PMN. Hence a strain could be placed on the films and the bond lengths constricted (as in La-PMN) without adding dopants. Studying the resultant crystal structure and size of ordered domains would reveal what effect compressive strain has on B-site ordering. The base substrate used was MgO upon which a layer of SrRuO_3 was grown. MgO has a lattice constant of 4.19 Å, and good quality epitaxial SrRuO_3 films can be grown on it. SrRuO_3 has a lattice constant of 3.92 Å which is 3.2% smaller than bulk PMN's lattice

constant of 4.048 Å. It also has the perovskite structure and is one of the best substrates for growing epitaxial ferroelectric thin films (in contrast to platinum as discussed in Chapter 7). As in any thin film experiment, the effect of the substrate is most easily observed in thinner films, but this must be balanced with the need to grow stoichiometric, epitaxial films. Hence, a series of thicknesses were grown on SrRuO₃ and one film was grown on MgO to check the effects of tensile strain.

5.2 Film growth

Films of 50, 100, 200 and 1500 Å were grown using pulsed laser deposition. This technique uses a ceramic target of PMN which is synthesized in the standard columbite process [4]. A KrF laser is then focused onto the target and pulsed at 6 Hz, ejecting small quantities of the target material. The film deposition then takes place on a MgO substrate which is kept at a temperature of 625° C to promote crystallization. The oxygen pressure during deposition is a crucial variable for achieving stoichiometric films and it was varied between 0.1 and 0.2 mbar [5]. Deposition time varied from 1 to 20 minutes. The substrate for most films was MgO with {100} orientation covered with a 1000 Å layer of SrRuO₃ which was also deposited at 625° C. One film of 5 nm thickness was grown directly on the MgO substrate.

The resulting films were well oriented with the perovskite structure and the <001> direction perpendicular to the substrate. Through careful control of the deposition conditions, the pyrochlore structure was avoided. The x-ray diffraction scans and plan-view transmission electron microscopy [4] both showed strong in-plane orientation of the films, suggesting epitaxial growth of the perovskite phase. Pulsed laser deposition is a

very effective technique for growing crystalline thin films of complex perovskites. Since it involves a ceramic target of known composition, the cation composition of the film is conserved.

As expected, the dielectric response of the films was considerably lower than bulk ceramics or single crystals. Figure 5.1 shows the dielectric constant and loss as a function of temperature for 3 measuring frequencies. The data were taken on the 1500 Å film, and the maximum in dielectric constant is only about 1000 versus 30,000 for single crystal PMN. Also, larger frequency dispersion was observed which is also characteristic of thin films and understood to be due to the relatively greater influence of space-charge fields at the interface with the electrode [6].

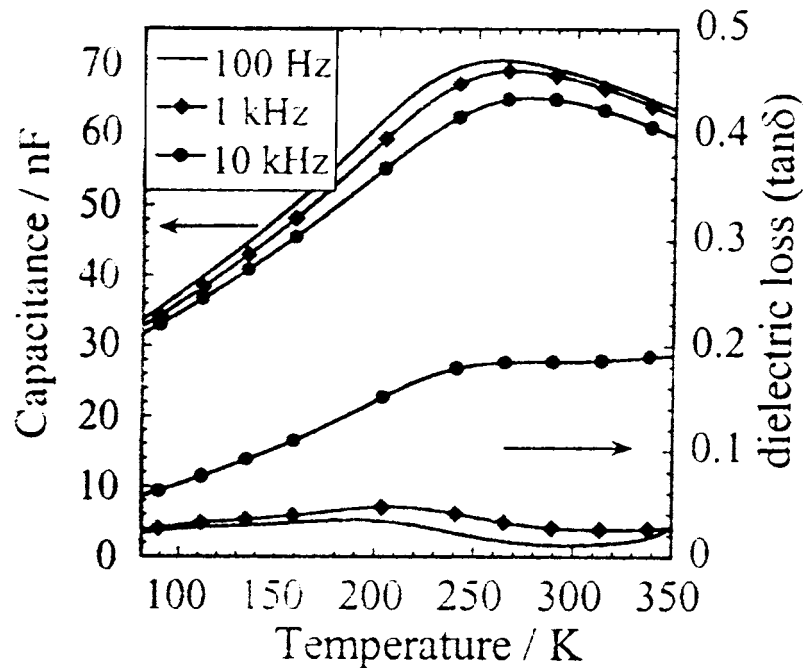


Figure 5.1. Dielectric properties of the 1500 Å PMN thin film taken from [5]. The dielectric constant is proportional to “Capacitance” and has a peak of only 1000.

5.3 X-ray measurements

Due to the limited scattering power of very thin films, x-ray measurements were performed at the National Synchrotron Light Source at Beamline X16C. Each film was oriented with a $\langle 001 \rangle$ direction perpendicular to the surface which made it easy to find peaks and align the samples. The substrate peak from the MgO single crystal dominated the diffraction pattern and the SrRuO₃ peaks were also clearly visible. However, since they all had slightly different lattice constants, the PMN peaks could be clearly separated. Figure 5.2 shows the two substrate peaks as well as the (111) peak of the 100 Å PMN film.

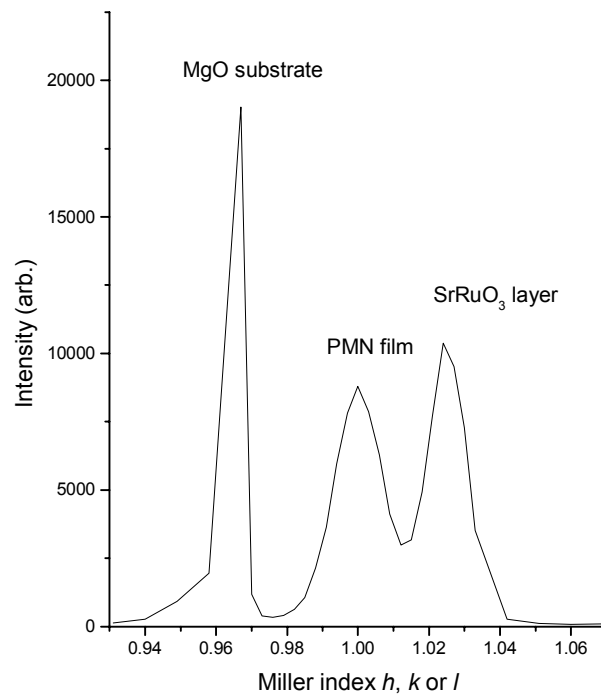


Figure 5.2. Scan through the (111) peak of the PMN thin film in the $\langle 111 \rangle$ direction clearly shows the single crystalline MgO substrate and the SrRuO₃ intermediate layer.

After aligning each sample in the diffractometer, about five bulk Bragg peaks were measured to determine the lattice constants. Reflectivity measurements were also made by scanning θ / 2θ at very low angles. If there is a “clean” interface between film and substrate, then the reflectivity measurement will reveal an interference pattern of maxima and minima. However, only smooth curves were found for each film, indicating that the interface was either too rough or not well defined. Epitaxial alignment with the substrate was found for each of the films. For the thinnest films, however, the limited size in the perpendicular direction caused their peaks to be very broad, so their positions, and hence lattice parameters, could not be measured as accurately. When fringes are not visible, the Scherrer formula is used to determine film thickness. For sufficiently thin films, the resulting diffraction peak becomes broader than the detector resolution. Using the Scherrer formula, the width of a peak scanned in the l direction (perpendicular to the substrate) gives an estimate of the film thickness. For the 1500 Å film, the l scan was resolution limited, but for the other films, the estimated thicknesses using the Scherrer formula roughly agreed with the nominal thickness determined by the deposition time.

Although the epitaxial quality of the films was quite good compared to similar films [4], and much better than the sol gel films discussed in Chapter 7, they were still significantly affected by mosaic broadening. This is the effect where neighboring domains in the film are slightly tilted with respect to each other, and it introduces an artificial width to every diffraction peak. In these films, the mosaic broadening was most noticeable in the transverse directions which would represent rotation of the domains in the plane of the surface with respect to one another. The signature of mosaic broadening is that peaks of higher order originating from the same q direction (e.g. (111) and (222)) have a fixed width in θ while non-mosaic broadened peaks have narrower θ widths

for higher order reflections. As shown in Figures 5.3a and b, the 1500 Å film was not affected by mosaic broadening. The peaks became narrower in the theta scans at higher order and are roughly constant in index scans. The 100 Å film was mosaic broadened, however, as seen by the constant peak width in the theta scan (Figure 5.3c) and the broadening of the index scan when higher order reflections are measured (Figure 5.3d).

In the radial direction, there is no mosaic broadening because radial scans are a direct measure of planar spacings. Transverse scans indicate that the thin film geometry allowed tilting of domains in the plane of the film (about an axis perpendicular to the film). In the 200 Å film, scans of the (101) and (202) peak show mosaic broadening when scanned along the $\langle 010 \rangle$ direction (Figure 5.4a) but not along the radial $\langle 101 \rangle$ direction (Figure 5.4b). In the thinner films, the size effect became significant, so the l scans became broader than the h and k because of the shrinking dimension of the film perpendicular to the substrate. Since it depends on direction, the mosaic resolution function can be estimated by comparing its effect on different reflections, so its effects can be distinguished from domain size broadening.

5.4 Results

The lattice constants for each film are given in Table 5.1, along with the average lattice constant for comparison with bulk PMN (which is 4.048 Å). In each case, the unit cell volume is reduced from the bulk value by approximately 0.9%. Also evident in each sample is a shift from simple cubic to tetragonal with the longer c -axis occurring perpendicular to the film. This is expected for a substrate with a smaller lattice constant

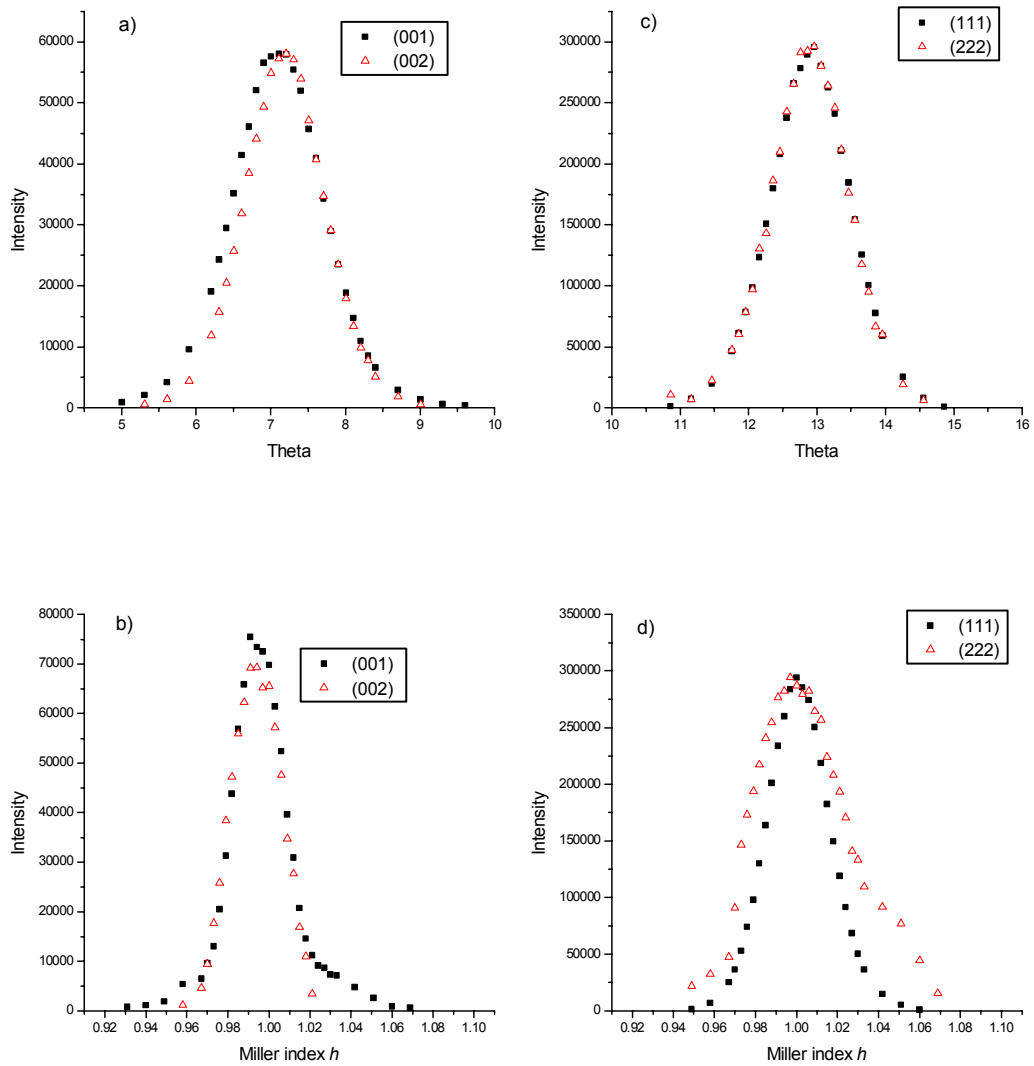


Figure 5.3. Mosaic broadening. In the 1500 Å film (a and b), the theta scans get slightly narrower and the index scans are roughly constant for higher order peaks. For the 100 Å film, mosaic broadening causes the theta scans to have equal widths and the index scans to have increased widths for higher order peaks.

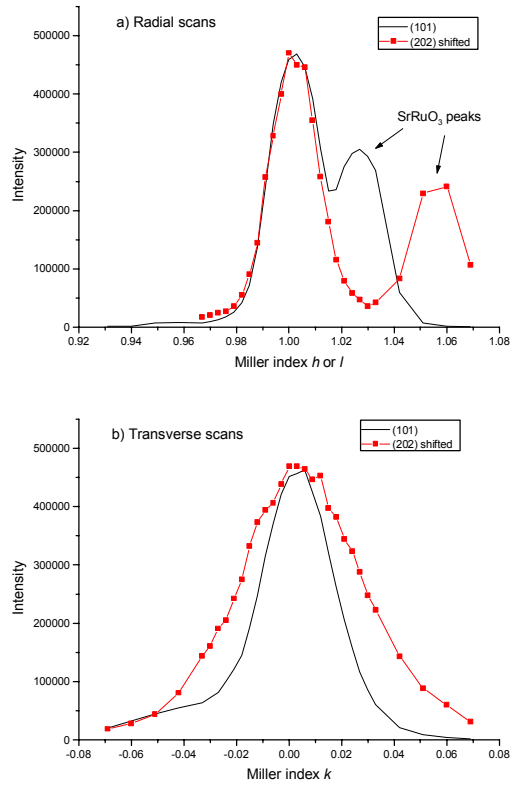


Figure 5.4. The (101) type peaks show mosaic broadening when measured in the transverse $\langle 010 \rangle$ direction but not in the radial $\langle 101 \rangle$ direction.

Table 5.1. Measured lattice constants of each film. The c direction is perpendicular to the film, and the average is the cubed root of the volume.

nominal thickness (Å)	a (Å)	b (Å)	c (Å)	Avg. (Å)
1500	4.00	4.00	4.06	4.02
200	4.00	3.97	4.032	4.00
100	3.99	3.99	4.042	4.01
50	3.98	4.00	4.025	4.00
50 (no SRO)	3.99	4.01	4.063	4.02

than the film. Thus, the strain of the smaller substrate is taken up by the film in two ways: reduced volume and tetragonality. The reduced volume became more pronounced in the thinner films.

Half order peaks were observed in all the films on the SrRuO₃ layer. This was especially surprising in the thinner films as the ordered domain size in some cases approached the film thickness as seen in Figure 5.5 which shows a (202) bulk peak superimposed over a (0.5, 0.5, 0.5) superstructure peak. The width of the bulk peak is due to the size effect of the mosaic blocks that are present in the film because the film is not single crystalline but is broken up into grains. The broadened (0.5, 0.5, 0.5) peak is the result of the size effect of the chemically ordered superstructure domains. Using the Scherrer formula, the bulk grain size in the thickest film was 170 Å and the superstructure ordered domain size was 90 Å, considerably larger than the 50 Å found in single crystal PMN. The intensity of the superstructure peaks compared to the Bragg peaks was relatively stronger in the films than single crystal PMN at low q values. However, the peak intensity quickly dropped off at higher q values due to the mosaic spread of the films which cuts the intensity of higher order reflections. The limited volume of the thin films in addition to the increased background caused by the substrate made it difficult to observe the weaker superstructure peaks at higher q values. The widths of the superstructure peaks in the thinner films were roughly equivalent to the bulk peaks, suggesting that entire domains were chemically ordered (Table 5.2). In contrast, the superstructure peaks in single crystal PMN are about 30 times wider than the bulk peaks.

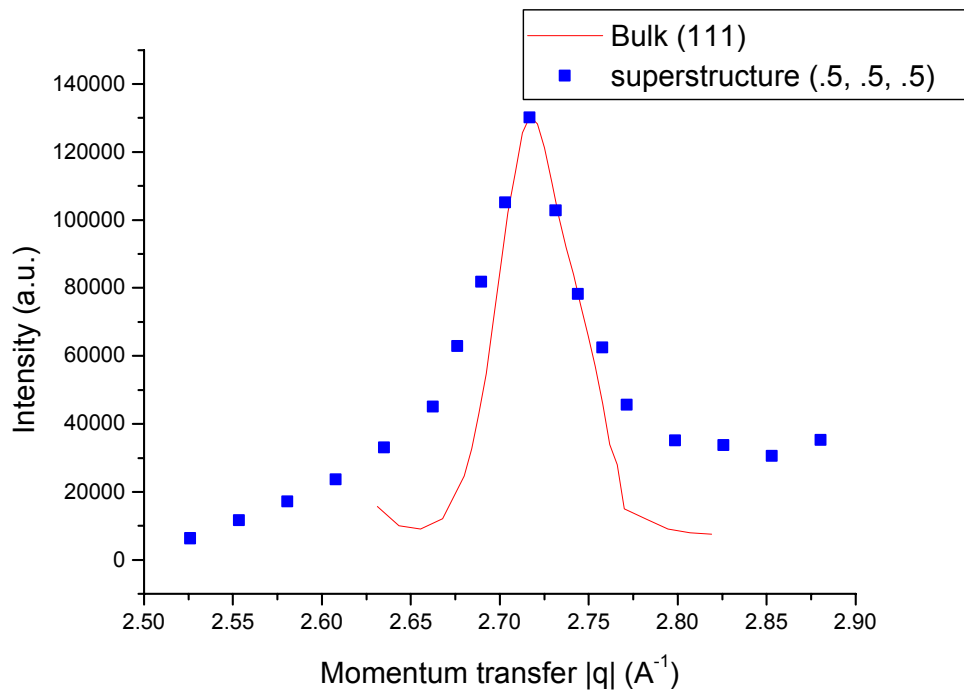


Figure 5.5. Enhanced chemical ordering in the films led to superstructure peaks with widths almost as narrow as the bulk peaks in all films grown on the MgO/SrRuO₃ substrate. The 200 Å film is shown.

Table 5.2. Bulk and ordered domain size of each film. Bulk domains are the result of the film breaking up into mosaic blocks to better accommodate the misfit with the substrate. The ordered domains result from the chemical ordering of Mg and Nb.

nominal thickness (Å)	bulk domain size (Å)	ordered domain size (Å)
1500	170	110
200	80	60
100	100	70
50	70	70
50 (no SrRuO ₃)	50	none

5.5 Discussion

In all the thin films grown on MgO/SrRuO₃, the chemically ordered domains were larger than in bulk PMN. Thus, it is not necessary to dope with extra positive charge to increase the ordered domain size. This is evidence to support the view that strain plays an important role in the 1:1 chemical ordering found in PMN. The presence of the SrRuO₃ substrate produced an average compressive strain of 0.9%. Additionally, there was a misfit of 2.2% between the strained PMN film and the SrRuO₃ substrate. The biaxial interfacial strain and the misfit caused the thin films to break up into smaller domains with the mosaic structure as discussed. A large number of dislocations thus occurred between the domains. In the out of plane direction, the PMN films stretched their *c*-axes relative to the *ab* plane to partially relieve strain while trying to maintain the bulk crystal volume. In the film grown directly on MgO (with a larger lattice constant than bulk PMN), no half-order peaks were found, indicating that tensile strain does not induce chemical ordering in PMN.

Because La is smaller than Pb, it also changes the cell volume thus affecting the packing forces as seen in Chapter 4. The effective strain produced by the SrRuO₃ substrate in these experiments would be the structural equivalent of doping with 25% La, as far as cell volume is concerned. However, using the SrRuO₃ substrate to strain the system does not provide additional charge as when actually doping with La. The effect of this strain is difficult to accurately compare with the bulk because the film was broken up into grains. However, the fact that bulk and superstructure peaks have roughly equal widths suggests that the desire to order was greatly enhanced by the added strain. Also, the ordered domain sizes in all the thin films were larger than the 50 Å ordered domains in single crystals of pure PMN, as seen in Table 5.2. In addition, measuring the structural

aspects of the thin films helped to understand the dielectric properties. The breaking up of the film into domains and the increased B-site ordering led to decreased dielectric constant values and more relaxor-like behavior. Similarly, the increased ordering in La-PMN led to decreased dielectric constant and increased relaxor behavior.

5.6 Conclusion

Substrate induced strain encouraged nearly complete ordering on the B-site in thin films of PMN, although the crystal grains were limited in size. The strain was accommodated in the film by a shift to tetragonality, a reduced unit cell volume and the breaking up of the film into smaller domains as seen by mosaic broadening in the h and k directions. Further experiments on better quality films with larger domain sizes would confirm the effect of strain on increased B-site ordering. However, this is more evidence that strain plays an important role in inducing the 1:1 chemical ordering in PMN. It appears that the random layer model is present in these thin films of pure PMN based on the degree of ordering and the electrostatic considerations discussed in Chapter 4.

The added charge provided by the La is not required to increase chemical ordering, so the main argument in support of the space charge model is invalid. The substrate induced strain was enough to increase the chemically ordered domain size, and the random layer type of ordering was present. However, conclusions about the ordering in single crystal PMN can not be made based on the results of thin films. Instead these results suggest that the random layer ordering can be induced in pure PMN when a substrate strain is present, and that La is not needed to increase the ordered domain size. In the second half of the next chapter, evidence supporting the random layer model is presented

based on resonant analysis of the composition of the ordered regions in single crystal PMN.

5.7 References

- [1] J Chen, H M Chan and M P Harmer, *J. Am. Ceram. Soc.* **72** [4], 593-98 (1989).
- [2] M A Akbas and P K Davies *J. Am. Ceram. Soc.* **80** [11], 2933 (1997).
- [3] B K Kim, S B Cha, J H Park, S J Park, *Jpn. J. Appl. Phys., Part I*, **37**, 5249 (1998).
- [4] S L Swartz, T R Shrout, *Mater. Res. Bull.*, **17**, 1245 (1982).
- [5] G Catalan, M H Corbett, R M Bowman, J M Gregg, *Appl. Phys. Letters*, **74**[20], 3035 (1999).
- [6] Y Fukuda, K Numata, K Aoki, A Nishimura, *Jpn. J. Appl. Phys., Part I*, **35**, 5178 (1996).

Chapter 6

X-ray Resonance

6.1 Diffraction anomalous fine structure

6.1.1 Background

The extended x-ray absorption fine structure (EXAFS) technique is a powerful probe of short range structure. It exploits the tunability of synchrotron sources to produce an incoming beam with energies that are near a given atom's atomic excitation level. Since each atom has different excitation energies, it is possible to study the chemical environment surrounding selected atoms. This can be especially helpful in mixed B-site relaxors in which several atoms are present because the environment around each atom can be studied separately.

A brief description of EXAFS will be given to better introduce the diffraction anomalous fine structure technique, or DAFS. The standard EXAFS procedure involves passing the incoming beam through a thinned sample and measuring the amount of radiation that passes through the sample. The photon energy is varied from just below the absorption edge of one of the atoms within the sample to several hundred eV above the edge. The resulting absorption spectrum gives information about the environment surrounding the chosen atom. As the photons are absorbed by the atom, photoelectrons are

emitted. The outgoing photoelectron wave scatters from neighboring atoms. These scattered waves then interfere with the original photoelectron wave causing quantum mechanical interference. The resulting oscillations in the absorption spectrum (Figure 6.1) can be analyzed to determine the structure surrounding the absorbing atom. Because the path length of the photoelectrons is small (typically a few nearest neighbors), EXAFS only probes the local structure. Since EXAFS is a short range order probe, a crystalline sample is not required.

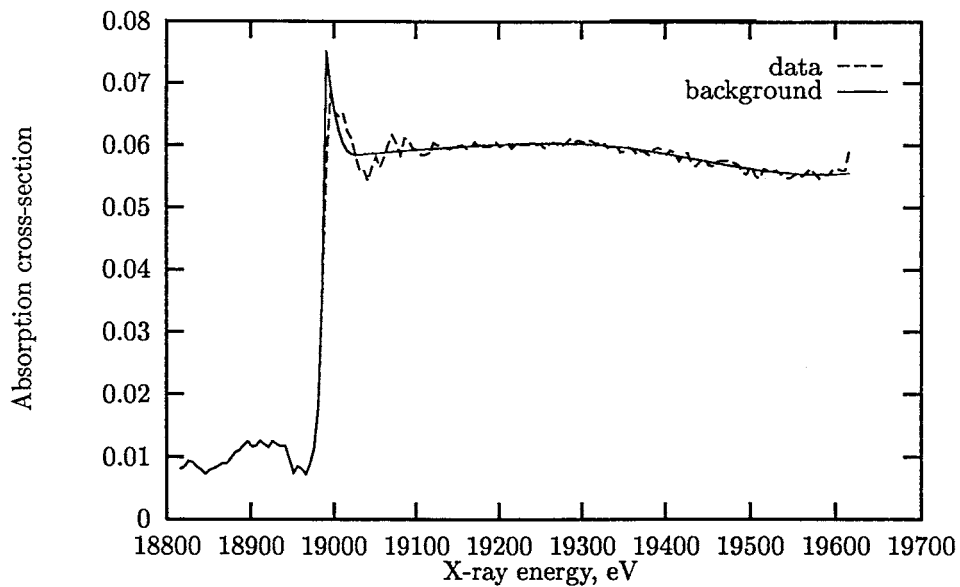


Figure 6.1. The EXAFS signal oscillates about the smooth absorption cross-section background of the bare atom. The oscillations are due to interactions and scattering from neighboring atoms.

The periods of these oscillations roughly correspond to interatomic distances. Data analysis proceeds by measuring the absorption of x-rays as energy is varied and then extracting the EXAFS function:

$$\chi(k) = \frac{\mu(k) - \mu_0(k)}{\mu_0(k)} \quad k = \frac{2\pi\sqrt{2m(E - E_0)}}{h} \quad (1)$$

where $\mu_0(k)$ is the smooth absorption function of the bare atom, k is the wavenumber of the virtually scattered photoelectron, E_0 is the absorption edge energy, m is the electron mass, and h is Planck's constant. Thus, $\chi(k)$ is the oscillating part that differs from the bare atom absorption function because of the photoelectron's interactions with neighboring atoms. The measured $\chi(k)$ function can be fit to the EXAFS equation to determine structural information [4]:

$$\chi(k) = \frac{S_0^2 N}{kr^2} f(k) \exp(-2k^2 \sigma^2) \sin(2kr + \delta(k)) \exp(-2r / \lambda(k)) \quad (2)$$

where S_0^2 is the passive electron amplitude reduction factor, N is the coordination number of the Nb-O bonds (6), r is half the total scattering path length, σ^2 is the mean square deviation of r , $f(k)$ and $\delta(k)$ are the effective scattering amplitude and phase shift, respectively, and $\lambda(k)$ is the photoelectron mean free path.

The DAFS technique is fundamentally very similar to EXAFS with the exception that the detector is placed at a diffraction angle of the crystal being studied. So, instead of measuring changes in the absorption of the incoming beam, changes in the diffracted intensity of a given peak are measured. Because of the connection through the structure factor, this allows one to select a particular crystallographic site. For example, in magnetite (Fe_3O_4) the iron atoms can be on either a tetrahedral or octahedral coordinated site and contain Fe^{3+} or a mixture of Fe^{3+} and Fe^{2+} ions, respectively. Using EXAFS, the

absorption spectrum would give structural information surrounding the average environment of both types of iron. Using DAFS, however, either type of iron atom can be isolated because a diffraction peak such as (222) involves scattering from the octahedral site while the (022) peak involves scattering from the tetrahedral site [1]. Thus, the site selectivity allows one to study the local structure surrounding either type of iron atom separately.

6.1.2 EXAFS on PMN

Prouzet et al [2] conducted an EXAFS study of PMN at the Nb K edge. By collecting data from the entire powder sample, they were unable to distinguish between behavior of the chemically ordered domains and the rest of the crystal. They found two distinct Nb-O bond lengths of 1.95 Å and 2.15 Å, which would represent the polar shift of Nb ions along a $\langle 111 \rangle$ direction which occurs in the polar domains of PMN. By fitting coordination numbers, they estimated that there were 2 long bonds and 4 short bonds. They interpreted this as the combination of two regions: a rhombohedral phase in the bulk of the crystal having 3 short and 3 long bonds and a chemically ordered region containing only short Nb-O bonds. However, their indirect evidence could not conclusively determine the structure in the ordered domains.

6.1.3 DAFS experiment

In this work, a DAFS study was performed in which superstructure peaks of PMN were used to study the structure of only the ordered domains of the crystal. The 1:1 chemically ordered domains of PMN produce superstructure peaks at the $(h+1/2, k+1/2,$

l+1/2) positions. The size of the ordered domains is very small (50 Å) and they make up only a fraction of the overall crystal volume. As described in Chapter 4, it is important to contrast the structure of the ordered domains of PMN with the rest of the crystal, so DAFS was used as a secondary technique to compare with the crystallographic study. In the EXAFS experiment described above, the absorption signal was collected from the entire crystal, so the resulting structure is an average of both the ordered and non-ordered regions. By sitting on a superstructure peak and performing a DAFS experiment, the non-ordered regions of the crystal were essentially disregarded and data from only the ordered domains was collected. However, because the ordered domains are so small, the subsequent counting rate was very low compared to the EXAFS experiment.

The DAFS technique is quite similar to EXAFS as both involve a photoelectron which scatters from neighboring atoms. The interference pattern between the photoelectron wave function and the scattering wave functions provide the information about the neighboring atoms. Both techniques are performed at an absorption edge of a specific atom. In DAFS, one of the crystal's Bragg reflections is used to further select a special superstructure within the crystal or a special crystallographic site. In EXAFS, the photoelectron is an actual electron that is ejected from the atom, while in the scattering process in DAFS, the photoelectron is a virtual electron.

In both techniques, the goal is to measure the oscillations or deviations from the anomalous corrections to the atomic form factor. As described in Chapter 2, the complete atomic form factor can be written as:

$$f(\mathbf{q}) = f_0(\mathbf{q}) + f'(E) + if''(E) \quad (3)$$

where f_0 is the smoothly varying portion (Figure 2.5), and $f'(E)$ and $f''(E)$ represent the anomalous scattering corrections (Figure 2.6). In practice, since f'' is proportional to the

absorption times energy, it is easier to measure, and f' is then calculated using the Kramers-Kronig equation which relates the two functions over a suitable frequency range [3]:

$$f''(\omega_0) = -\frac{2}{\pi} \int_0^{\infty} \frac{\omega_0 f'(\omega)}{\omega^2 - \omega_0^2} d\omega \quad (4)$$

This optical relation represents the interdependence of the absorption and scattering processes which are causally related.

A brief description of the DAFS theory will be given, and the detailed analysis can be found in [3]. The anomalous contribution to the atomic form factor can be written as:

$$\Delta f(E) = f'(E) + if''(E) = f_a'(E) + if_a''(E) + f_c''[\chi'(E) + i\chi''(E)] \quad (5)$$

where E is the photon's energy. The subscript a refers to the smoothly varying form factor of a bare atom, while the subscript c denotes the oscillating terms that result from the atom being in condensed matter. The first two terms will give the general shape and can be fit using known functions. Then the difference between the bare atom fit and the actual data can be used to learn about the atom's local environment. By analogy with EXAFS experiments[4], the corresponding DAFS function that needs to be extracted is the imaginary part of the above equation:

$$\chi''(k) = \frac{f''(k) - f_a''(k)}{f_c''(k)} \quad k = \frac{2\pi\sqrt{2m(E - E_0)}}{h} \quad (6)$$

Again, k is the wavenumber of the virtually scattered photoelectron, E_0 is the absorption edge energy and h is Planck's constant. As with the EXAFS function, χ represents the part of the function that oscillates about the bare atom form factor. The f'' is proportional to the x-ray absorption cross section times the x-ray energy. Once f'' is known, then f' is found using the Kramers-Kronig relation. It has been shown [3] that the EXAFS function

$\chi(k)$ is identical to the DAFS function $\chi''(k)$, so the well-developed EXAFS analysis can be applied to DAFS measurements.

However, unlike EXAFS, DAFS does not directly measure $f''(E)$. Instead, it measures diffracted peak intensity I which is proportional to the square of the structure factor F . Neglecting Debye-Waller factors, the structure factor is given by:

$$F(q, E) = \sum_j [f_0(q) + \Delta f(E)] \exp(iq \cdot R_j) \quad (7)$$

where f_0 is the atomic form factor, Δf is the anomalous correction ($f' + if''$), q is the momentum transfer, E is the photon energy and the R_j are the atomic positions within the unit cell. The f'' must be extracted from the $|F|^2$ function. This expression can be simplified by several experimental conditions. As seen in Chapter 4, the structure factor for the half-order superstructure reflections in PMN is simply $f_{Mg} - f_{Nb}$ (or two-thirds of that) so that the Pb and O atoms do not contribute to the scattering. Since experiments were performed near the Nb absorption edge, Δf for Mg is zero. Then,

$$F = f_{Mg}^0 - f_{Nb}^0 - f_{Nb}' - if_{Nb}'' \quad (8)$$

is the structure factor for the 1:1 ordering superstructure peaks when the photon energy is near a Nb edge. Taking the square gives:

$$|F|^2 = (f_{Mg}^0 - f_{Nb}^0)^2 - 2f_{Nb}'(f_{Mg}^0 - f_{Nb}^0) + (f_{Nb}')^2 + (f_{Nb}'')^2 \quad (9)$$

where the resonant terms (prime and double prime) depend on energy, and the non-resonant terms (f^0) are known.

6.1.4 Data retrieval

Scans were taken at the (0.5, 0.5, 2.5) superstructure peak near the Nb K-edge which is at 18.968 keV. This energy is near the upper limit of the monochromator at beamline X16C which made it difficult to accurately focus the beam throughout the energy scans and also limited the intensity. The L_{III} edge of Pb at 13.035 keV is also accessible, but it did not have a significant EXAFS signal there. This is most likely due to the structural disorder on the A-site. Due to the weakness of the superstructure peaks, it was necessary to collect about 20 energy scans of three minutes each to improve the counting statistics. Off-peak data was also collected to measure the fluorescence background which was then subtracted from the data. The fluorescence background comes from the radiated photons that are emitted when the core shell electron levels are filled. The resulting data after correcting for absorption and fluorescence are shown in Figure 6.2. The separation of f' and f'' was accomplished using computer programs developed at the University of Washington [5]. Bare atom f' and f'' calculated using the Cromer-Lieberman [6] method were used for initial guesses (dashed lines in Figure 6.3). Then the iterative Kramers-Kronig (equation 4) procedure was applied to fit equation 9 to the measured intensity. After varying f'' , the Kramers-Kronig relation was used to solve for a new f' and these new estimates were substituted back into equation 9. The cycle is repeated until a best fit is found. The resulting f'' function is then converted into an absorption function by dividing by energy so it can be analyzed using standard EXAFS procedures. The resulting measured f' and f'' are the solid lines in Figure 6.3.

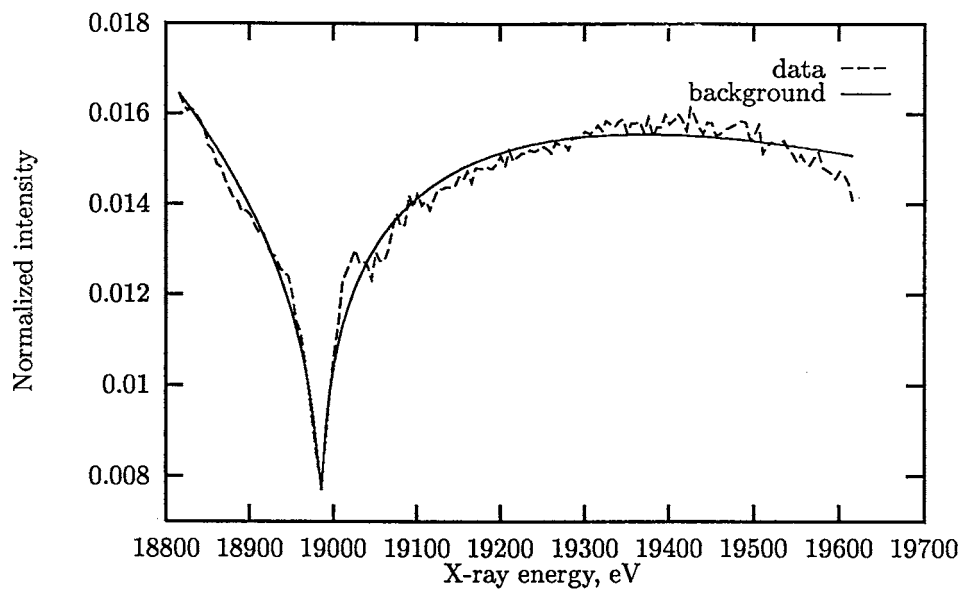


Figure 6.2. Normalized DAFS signal (dashed) after correcting for absorption and fluorescence, and a smooth background (solid) from equation 9.

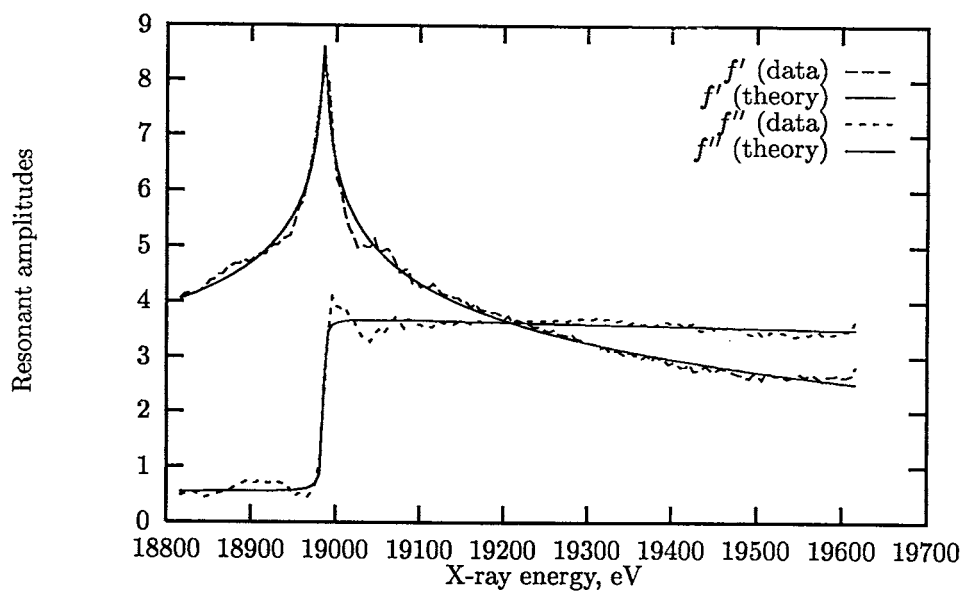


Figure 6.3. Resulting $f'(E)$ and $f''(E)$ by iterative fit to Kramers-Kronig. The theoretical bare atom response functions, $f'_a(E)$ and $f''_a(E)$, used as starting approximations are shown for comparison.

6.1.5 EXAFS/DAFS analysis

The software packages UWXAFS and AUTOBK [7] were used to remove the smooth atomic contributions, leaving the EXAFS function $\chi(k)$ which is related to the structure via equation 2:

$$\chi(k) = \frac{S_0^2 N}{kr^2} f(k) \exp(-2k^2 \sigma^2) \sin(2kr + \delta(k)) \exp(-2r / \lambda(k)) \quad (2)$$

The functions $f(k)$, $\delta(k)$ and $\lambda(k)$ were calculated with an *ab initio* FEFF6 [8] code for the Nb-O bonds using the cubic perovskite structure as a starting model.

Equation 2 was fit in r space by Fourier transforming the data and theory within a k range between 2 and 7 \AA^{-1} which is equivalent to a real space range of 1.1 to 2.2 \AA . Because of the low counting statistics and subsequent noisy data, a limited data region was used. As shown in Figure 6.4a, the data fit well to the first two or three oscillations in k space. The Fourier transformed data and fit in Figure 6.4b indicate that only the first nearest neighbor distance can be accurately derived from the limited data. However, this is an important parameter in the structure of the ordered domains of PMN as discussed in Chapter 4. By fixing S_0^2 to 0.9 as measured previously for the Nb edge [9] and assuming harmonicity in the Nb-O bonds, equation 2 was fit with three variables: the zero of the photoelectron energy, ΔE_0 , the Nb-O bond length, Δr , and the mean square disorder in the bond lengths, σ^2 .

A value of 1.973(10) \AA was found for the Nb-O bond length which compares favorably with the value of 1.981(5) from Chapter 4 which was measured using

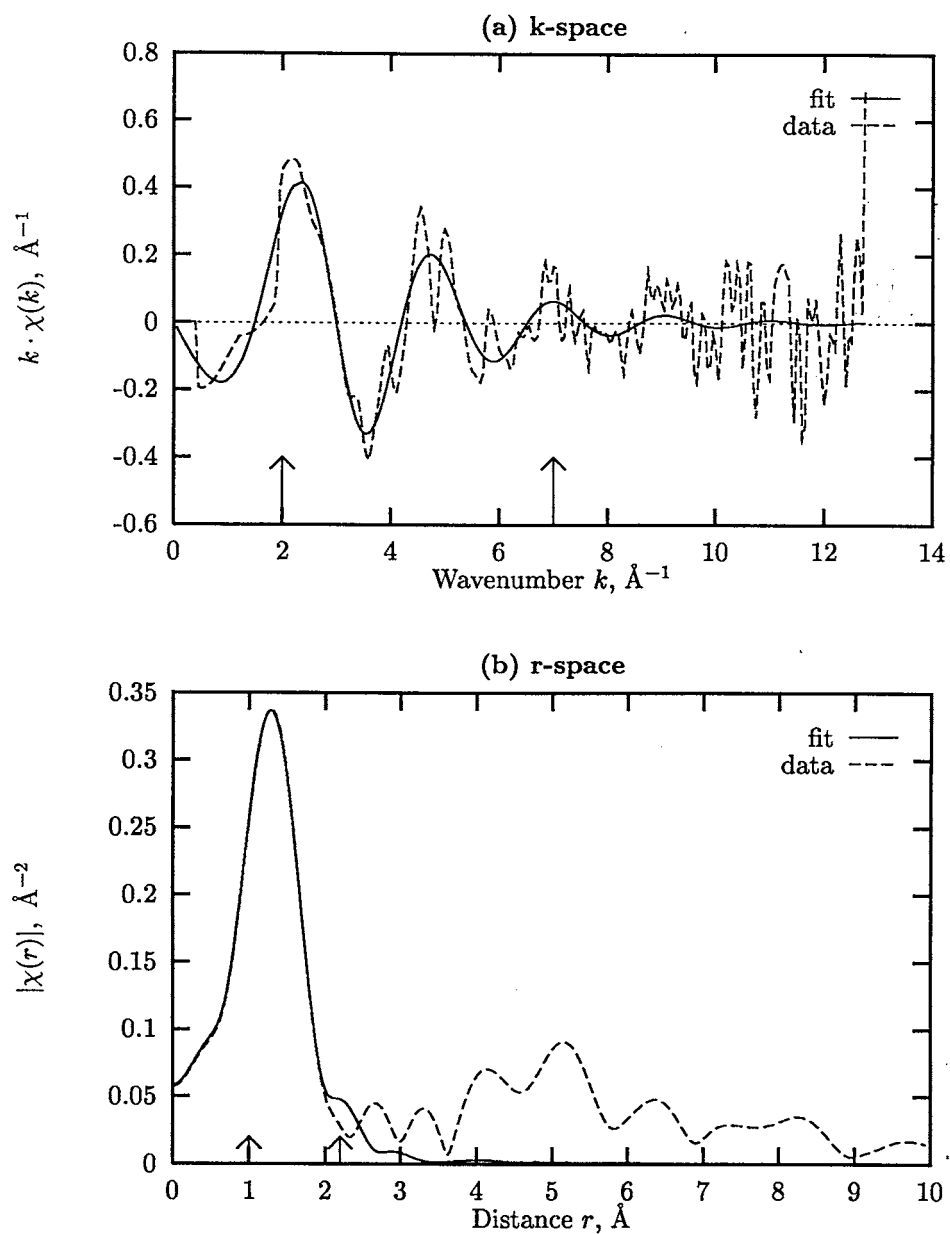


Figure 6.4. Fit of equation 9 using FEFF6 theory [8] (dash) to the data (solid) in a) k -space and b) r -space.

conventional crystallography. The DAFS measurement gives an oxygen displacement of $0.052(10) \text{ \AA}$ as compared to $0.044(5) \text{ \AA}$ from the diffraction experiment, confirming that the Nb ions are in fact squeezed by the oxygen ions in the ordered domains. The value of σ^2 was fit to be $0.0087(3) \text{ \AA}^2$ which is significantly greater than the EXAFS measurement of PMN [2] which found 0.0036 \AA^2 . The discrepancy may represent a larger disorder in the ordered domains of PMN compared to the average, or it may reflect the inherently noisy data caused by the low counting rates in this DAFS measurement.

In conclusion, DAFS is a useful technique for probing short range order. It allows one to study selected regions that have additional ordering compared to the rest of the crystal. However, when such regions are very small in extent, the subsequent low counting rates make performing the experiment and analyzing the data difficult. Nonetheless, an independent confirmation of the previous crystallographic measurements was made and an important structural parameter--the Nb-O bond length exclusively within the ordered domains--was extracted.

6.2 Resonant scattering

6.2.1 Background

Resonant x-ray diffraction also exploits the energy dependent terms in the atomic form factor. As discussed in Chapter 2, f' is sharply peaked and negative near an absorption edge. f'' also changes but less dramatically, and it can be accounted for by a step function absorption correction. In the case of Nb's K edge at 18.968 keV, f' has a maximum negative value of minus 13 electrons (Figure 6.5) which can be compared to f_0

for Nb which is roughly 34 electrons for the $|q|$ values in these experiments. Since intensity is proportional to the square of the structure factor, this resonant contribution is quite significant.

Different Bragg reflections have different structure factors, so the resonant effect will depend on which reflection is being studied. In centro-symmetric crystals, the phase of the scattering atoms is either zero or pi. Using resonant techniques it is possible to determine the relative phase of a given atom compared to the other scatterers. For example, evaluating the structure factor of the (001) peak gives:

$$F = f_{Pb} - f_{Oxy} - (\frac{2}{3} f_{Nb} + \frac{1}{3} f_{Mg}) \quad (10)$$

while the (011) peak has a structure factor of:

$$F = f_{Pb} - f_{Oxy} + (\frac{2}{3} f_{Nb} + \frac{1}{3} f_{Mg}) \quad (11)$$

Since the photon energy is near the Nb edge only, the simple f_0 form factors for Pb, Mg and O can be used but f_{Nb} must be given by the full $f_0 + f' + if''$. For the (001) peak, f_{Nb} is approximately 37 electrons off resonance and 24 electrons on resonance, f_{Pb} is 76 electrons, $f_{Mg} = 10$ and $f_{Oxy} = 7$. For the (001) peak the resonant contribution will increase F and the amount of scattering by making the difference between f_{Pb} and f_{Nb} greater. However, for the (011) peak, the resonant contribution will decrease the amount of scattering because it is negative. Also, the resonant contribution will have a greater effect on the (001) peak because the structure factor involves the difference between Pb and Nb instead of the sum, so its proportional contribution will be larger.

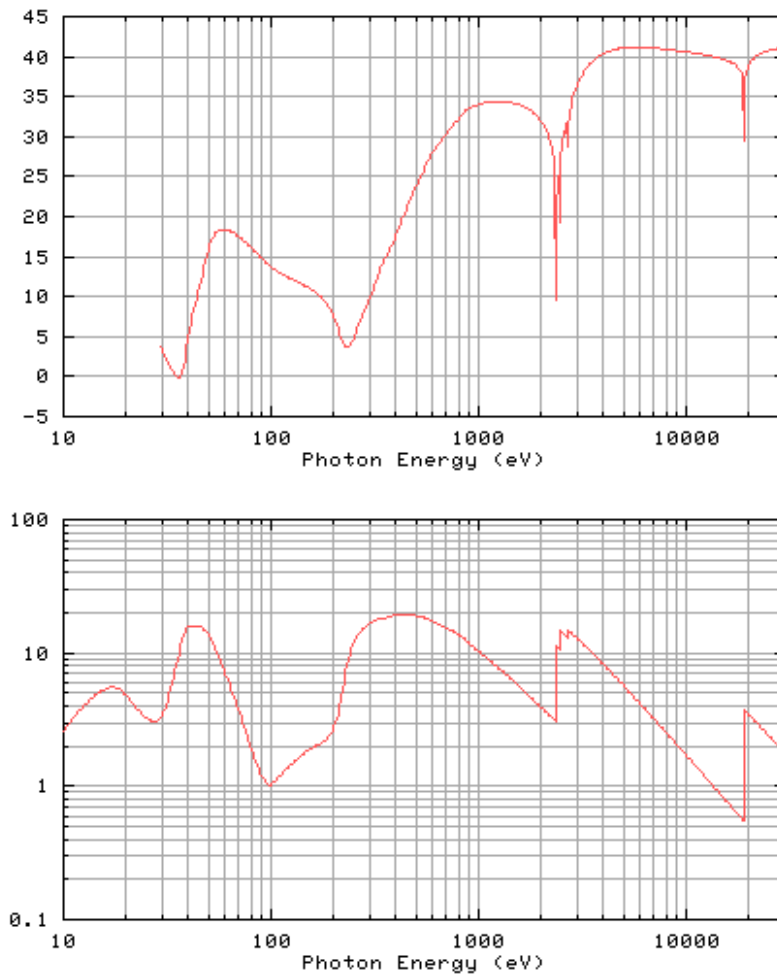


Figure 6.5. Anomalous scattering factors, $f'(E)$ and $f''(E)$, for Nb [10].

Our goal was to search for the Nb-deficient domains predicted by the space charge model. It is necessary to measure bulk reflections because the Pb contribution to the structure factor can then be used as a reference from which the changing Nb contribution can be measured. If superstructure peaks were measured, then the structure factor is given by $f_{\text{Mg}} - f_{\text{Nb}}$ for the space charge model and two-thirds of that for the random layer model. By measuring on the Nb resonance condition, the structure factor is changed by the same amount in both cases, and the only difference between the models is just an absolute scale factor. The Pb contribution provides a fixed background that is known. The scattering from the small ordered domains produces intensity at both integer order and half-order positions. In Chapter 4, the half-order peaks were measured because they are not hidden beneath the much stronger Bragg peaks that are produced by the entire crystal. In this chapter, since integer order peaks must be used, it is necessary to look for changes in the wings of the peaks where the broad contribution from the small ordered domains will be visible.

6.2.2 Space charge vs. random layer

In PMN, since the basic structure is known (and hence the phases), resonant scattering can be used to gain information about occupancies. As discussed in Chapter 4, the ordering of PMN can be attributed to two types. The “space charge” ordering model involves 1:1 ordering between Nb and Mg ions. That makes the ordered domains Nb-deficient compared to the average crystal in which two-thirds of the B-sites are Nb. The “random layer” ordering model involves 1:1 ordering between Nb on one site and a mixture of $(\text{Mg}_{2/3}\text{Nb}_{1/3})$ on the other. Hence, the ordered domains have the same average

chemical composition as the bulk. By measuring the intensities of various peaks both on and off the resonance condition, the relative amount of scattering from Nb ions can be deduced. The goal is to determine whether or not the small ordered domains have a different Nb composition than the average crystal.

One method is to look at the shape of bulk reflections. These peaks are very sharp and will have a central peak which comes from the entire crystal. This peak must have a stoichiometric contribution from Nb because the entire crystal has to be stoichiometric (and charge neutral). However, it will also have contributions from the smaller ordered domains. The scattering will be much weaker, but it will also be much broader since it originates from domains of only about 50 Å in size. Using the Scherrer formula, its diffraction peak will be spread out in reciprocal space with a half-width of about 0.05 reciprocal lattice units compared to the resolution limited value of about 0.005 for the central peak.

If one assumes that space charge ordering is present, then the ordered domains have less Nb than the average crystal. In that case, for a bulk reflection such as (001), the effect of the resonance is to increase the overall amount of scattering as discussed above (see equation 10). However, the scattering contribution from the ordered domains (the weak but broad peak) will not increase as much because there is less Nb in those regions. Hence, the diffraction profile should have tails that are lowered for the on resonant scattering if the space charge model is present. For the space charge model, the structure factor of the ordered domains would be:

$$F = f_{Pb} - f_{Oxy} \pm (\frac{1}{2}f_{Nb} + \frac{1}{2}f_{Mg}) \quad (12)$$

where the plus sign is for the (011) type peaks and the minus sign is for (001) type peaks. Since the intensity of the scattering from the ordered domains compared to the entire crystal is known from measurements of the superstructure peaks, the expected change can be calculated. In the case of the (001) peak, the bulk scattering should increase by 46%, while the scattering from the ordered domains should increase by only 30% if the space charge model is present. Hence, in the tails of the peak, a decrease of up to 12% should be observed for the on resonance scan compared to the off resonance scan. The difference would become noticeable starting at about ± 0.05 r.l.u. away from the peak and would fade into the background beyond about ± 0.10 r.l.u. If the random layer model is present, then the structure factor of the ordered domains will be the same as equations 10 and 11 above, and the entire peak profile will be uniformly increased by the same amount.

Conversely, for a reflection such as (011), the resonant effect is to decrease the amount of scattering. But it will decrease it less for the space charge ordered domains that are Nb deficient. The tails of those peaks would then be greater on resonance than the tails of the off resonance peaks. However, due to the lower contrast of the (011) peak, the expected change is only about 4%. Note that if the random layer model is present, no change should be observed as the stoichiometry of the ordered domains does not change in that model, so the entire peak profile would be decreased by the same factor.

6.2.3 Data collection

Scans were made along reciprocal lattice directions through the (001), (101) and (111) peaks at various energies both on and off resonance. The (111) peak has a structure factor very similar to the (001) peak, and both will be referred to as (001) type peaks. As

discussed in the DAFS experiment, the fluorescence background is again significant and accounts for the increase in intensity as the edge is reached. A combined fluorescence and absorption correction was made by measuring the intensity away from a Bragg peak.

Figure 6.6 shows two corrected scans for the (111) peak on a semi-log plot to emphasize the features in the tails. The data represent below resonance and on resonance. There is not a significant decrease in the tails for the on resonance scan. The region of interest is plus or minus 0.05 r.l.u. from the peak. The lack of a change in the tails for the on resonance condition indicates that there is no Nb deficiency in the ordered domains within the error limits of this measurement. The expected change of 12% for (001) which would appear is shown by the dotted line in the figure. For the (101) peak, where the Nb scattering is in phase with the Pb, a slight increase (up to 4%) is expected in the tails if the

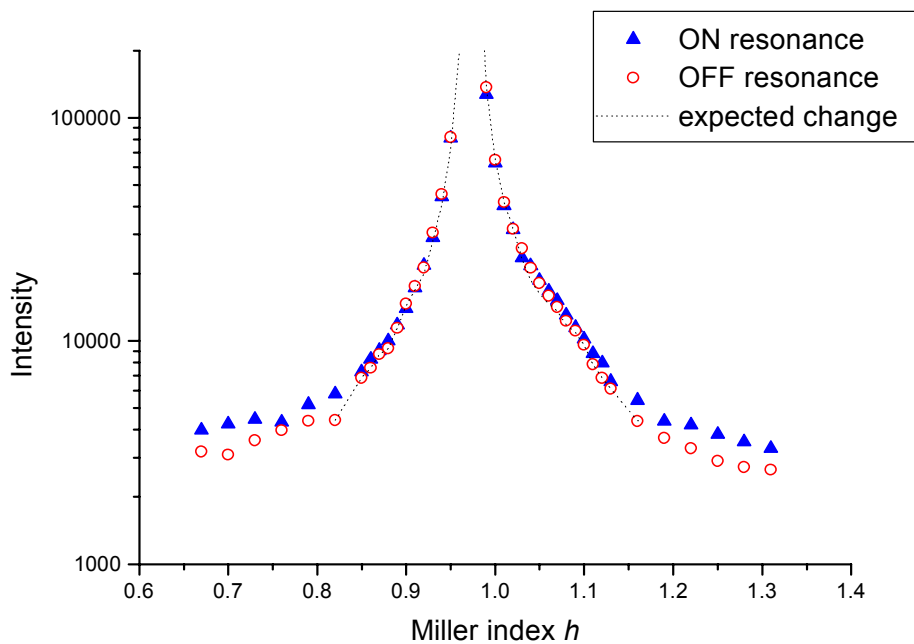


Figure 6.6. Scan through the (111) peak ON and OFF resonance. The expected change due to the space charge model is shown by the dotted line.

space charge model were present. However, no significant difference was observed.

These sensitive measurements are complicated by their proximity to very strong Bragg peaks, so an alternate measurement was performed. A more sensitive measurement was made by varying the energy while sitting at different points along the slope of a Bragg reflection. Energy can be scanned more reliably, and the full effect of the resonance is then measured as the change in the scattering as the photon energy is scanned. The energy scans adjust the diffractometer angles so that $|q|$ is held constant. The resonant effect (after corrections) results in a peak (for (001) type peaks) or a valley (for (110) type peaks) in the energy scans. By scanning the photon energy through the resonance condition, it was possible to measure the resonant fraction of the scattering after again correcting for fluorescence and absorption. The resonant fraction was measured at different points in reciprocal space surrounding the Bragg peak. Plotting this resonant fraction as a function of Miller index shows if the resonant scattering fraction increased or decreased in the wings of the peak.

For the random layer model, the resonant fraction should be constant as a function of Miller index since in that model the ordered domains have the same chemical composition as the bulk. For the space charge model, the effect of the Nb deficient domains would become apparent in the tails of the Bragg peak where the broader but weaker peak is not dwarfed by the central peak. For the (001) type peaks, the scattering from Nb deficient domains would increase less, so the amount of resonant scattering in the wings would be less than directly on the peak, and the opposite for (011) peaks. The region of interest is again approximately ± 0.05 reciprocal lattice units away from the Bragg peak. If the space charge model is present, a graph of resonant fraction versus

Miller index would show a decreasing resonant fraction away from the Bragg peak for the (001) peaks and an increasing resonant fraction for the (011) peaks. Again the change in resonant fraction is expected to be a 12% decrease for (001) and a 4% increase for (011) at ± 0.05 reciprocal lattice units.

Energy scans were made at various points in reciprocal space near the Bragg peak. Figure 6.7a shows the raw data of an energy scan through the Nb K-edge while sitting at the (001) peak. As discussed in the above section on DAFS, fluorescence and absorption corrections had to be made. The fluorescence correction curve (Figure 6.7b) was taken by scanning at an off-peak position--(0.9, 0, 0.9). By measuring the abrupt change in intensity, the absorption correction factor μ was determined (Figure 6.7b dashed line).

The correction can be expressed as:

$$I_{\text{corr}} = \mu (I_{\text{measured}} - I_{\text{fluorescence}}) \quad (13)$$

After making these corrections, the resonant peak is clearly seen in Figure 6.7c, even though the low counting rates have resulted in noisy data. The relative phase of the Nb ion is positive or negative depending on the reflection. The corrected peaks for scans near (001) were similar except their resonant contribution was positive. The resonant fraction was then calculated by fitting the peak to a fixed Lorentzian shape and taking the height divided by the background level. The fixed Lorentzian shape had a width of 41 eV in agreement with known resonance data. It was determined by taking an average of several scans of half order peaks where the shape of the Nb resonant contribution was more easily measured. The amount of resonant contribution to the superstructure peaks together with the known structure factor ($f_{\text{Nb}} - f_{\text{Mg}}$) was used to determine a value of 10 electrons for f' in PMN. This is slightly smaller than the bare atom value of 13 electrons

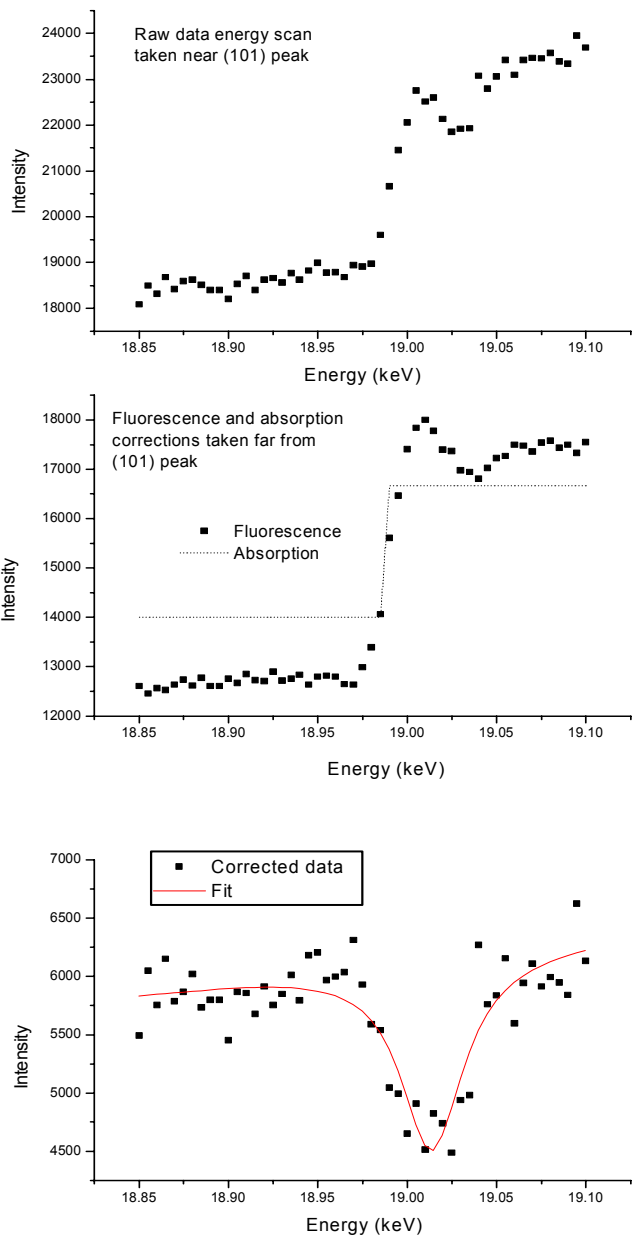


Figure 6.7. Data collection procedure:
 a) Raw data collected by scanning energy while sitting on the slope of a Bragg peak--at (0.96, 0, 0.96) in this case.
 b) Fluorescence contribution correction measured far from Bragg peak--(0.9, 0, 0.9) and step absorption correction.
 c) Corrected data are fit to a Lorentzian and the resonant fraction is the height divided by the background level.

because of measurement rounding and condensed matter effects.

6.2.4 Results

The plot of resonant fraction vs. Miller index for the (001) peak is shown in Figure 6.8 together with the expected curves for the space charge and random layer models. The exact positions along the y-axis of the expected curves depend on the value of f' that is used. From superstructure measurements, a value of 10 electrons for f' was obtained. Within the error estimate, it appears that the Nb composition of the ordered domains is the same as the bulk of the crystal. The expected deviations in the space charge model are represented by the lines in each figure. These were calculated using the peak profiles of the ordered domains which are known from the superstructure peaks. The basically straight line and its position indicate that the ordered domains are not Nb deficient as they would be for the space charge model. Similarly for the less sensitive (011) peak (Figure 6.9), there is not a significant deviation in resonant fraction, though it would be harder to measure the smaller effect. A future experiment with longer counting times and more data points would reduce the error bars and make the conclusions more definite. In addition, using ion chamber detectors instead of scintillators would allow points closer to the Bragg peak to be measured where the expected curve from the space charge model has a distinctly different behavior. Measuring these central points would enable a definite conclusion to be drawn based on the shape of the data.

Although these results point to the random layer model in pure PMN, they are not conclusive due to the large error bars which resulted from both the difficulty of the

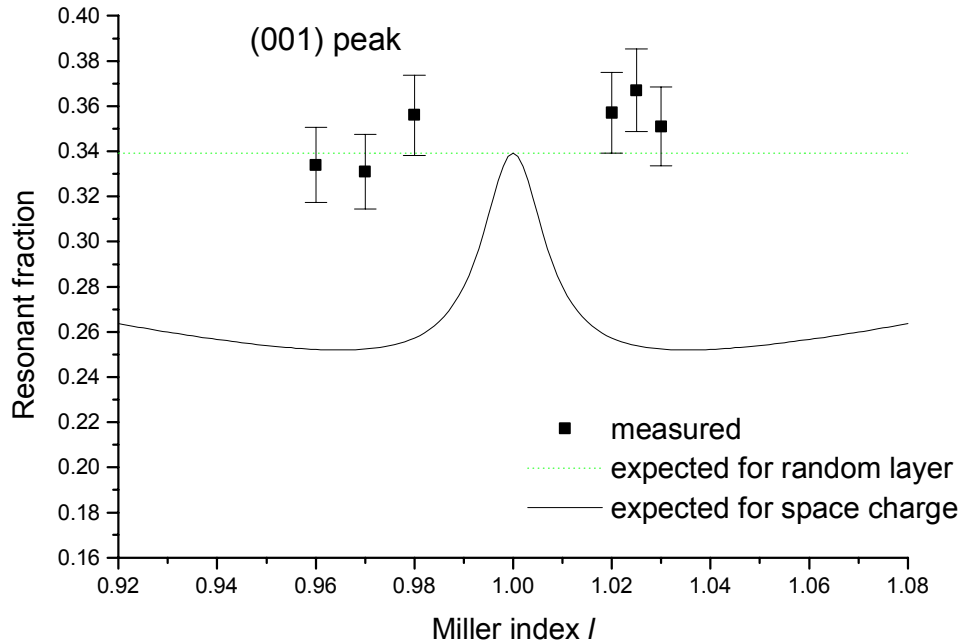


Figure 6.8. Resonant fraction measured at different points near the (001) Bragg peak. Data appear consistent with random layer model, but placement of the expected curves on the y-axis is dependent on the size of f' that is measured.

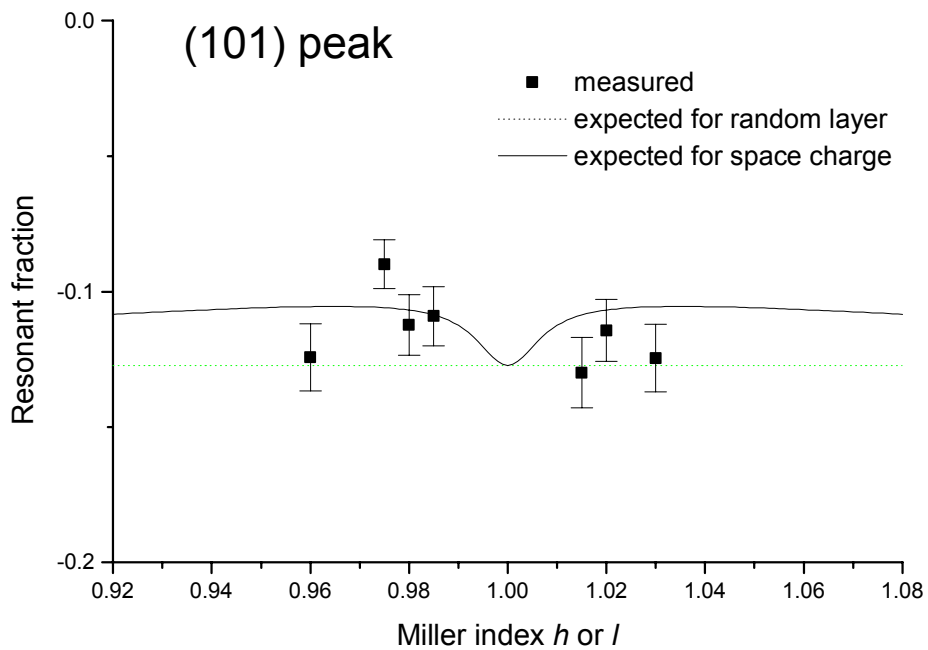


Figure 6.9. Resonant fraction measured at different points near the (101) Bragg peak.

measurement and the sensitivity that is required to see a small compositional change (from two-thirds to one-half) in very small domains within the crystal.

6.3 References

- [1] A I Frenkel, D M Fanning, I K Robinson, J O Cross, *J. Synchrotron Rad.*, **6** [3] 332 (1999).
- [2] E Prouzet, E Husson, N de Mathan, A Morell, *J. Phys.: Condens. Matter* **5** 4889 (1993).
- [3] H J Stragier, Ph.D. Thesis, University of Washington, (1993).
- [4] E A Stern and S M Heald, in *Handbook on Synchrotron Radiation*, edited by E E Koch, (North-Holland, New York, 1983), Chapter 10.
- [5] J O Cross, Ph.D. Thesis, University of Washington, (1996).
- [6] D T Cromer, D Liberman, *J. Chem. Phys.*, **53**, 1891 (1970).
- [7] E A Stern, M Newville, B Ravel, Y Yacoby, D Haskel, *Physica B*, **208**, 117 (1995).
- [8] S I Zabinsky, J J Rehr, A Ankoudinov, R C Albers, M J Eller, *Phys. Rev. B* **52**, 2995 (1995).
- [9] A I Frenkel, F M Wang, S Kelly, R Ingalls, D Haskel, E A Stern, *Phys. Rev. B* **56**, 10869 (1997).
- [10] B L Henke, E M Gullickson, J C Davis, *Atomic Data and Nuclear Data Tables*, **54** [2] (1993).

Chapter 7

Lead Zirconate Thin Films

7.1 Introduction

As discussed in Chapter 3, thin film ferroelectrics are rapidly becoming very important for applications while also providing a unique vantage point to study surface effects on ferroelectrics. The modification of a film's properties compared to the bulk is both a fundamental and technologically interesting problem. In addition, understanding phase transitions is a fundamental and important challenge in physics. The presence of a free surface adds to the complexity but can also lend insight to bulk behavior. Binder and Landau have reviewed the effects of surfaces on critical phenomena in a number of systems[1]. Monte Carlo simulations of surface critical behavior using Ising and XY models with nearest-neighbor interactions have been successful in identifying critical exponents and amplitudes and separating the bulk and surface contributions.

Generally speaking, in the case of thin films, the surface effects are not expected to be as important as in ultra-high vacuum experiments involving only single atomic layers. Instead, thin films add additional parameters to the problem in the form of lattice strain, the possibility of dislocations and electrostatic effects such as free surface charges. These surface effects usually modify the film's structure and properties within a certain length scale away from the surface.

In the field of ferroelectrics, thin films are also important because grain size or particle size directly affects the ferroelectric and electrostatic properties [2]. As film or grain size decreases, depolarization fields become significant and tend to lower the Curie temperature and maximum polarization values [3]. There have also been reports of a critical grain size below which ferroelectricity disappears [2]. In contrast to ferromagnets, ferroelectrics involve the long-range dipole interaction which is not present in very small grains. Also, the depolarizing surface effects become more pronounced as the volume is decreased. The effects of added strain and reduced ferroelectric activity can significantly alter the phase transition behavior of thin films compared to bulk samples. Binder et al have described some surface effects on phase transitions in ferroelectric thin films and the smearing of singularities due to finite size effects [4]. One consequence of thin films is the presence of free surface charges that partially compensate the polarization discontinuity. They also consider the variation in polarization near the surface which exists over some critical length that diverges at the Curie temperature. The polarization variations create electric fields that have the effect of gradually reducing the net polarization near the surface as studied via Monte Carlo simulations.

Scott et al [5] developed a Landau mean field theory to describe the behavior of thin films in their experiments on ferroelectric KNO_3 . This material exhibits a first order phase transition in the bulk but a second order transition in thin film form [6] as seen in the polarization dependence on temperature. For specific cases, their theory shows that the first order phase transition can be modified as in Figure 7.1 to be two first order phase

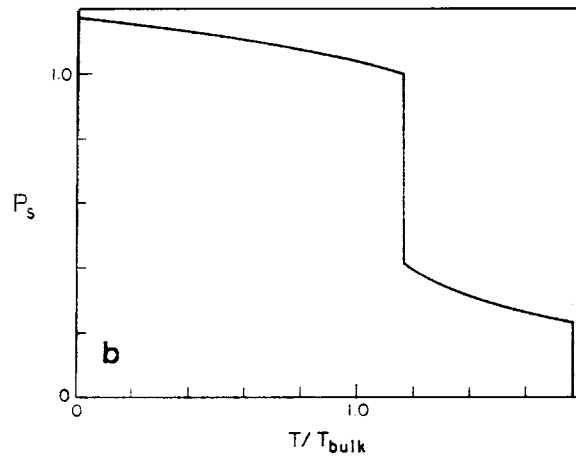


Figure 7.1. Scott et al [4] found that in thin film form, ferroelectrics can have their phase transition behavior modified. In KNbO_3 , a first order phase transition in polarization vs. temperature is changed to two first order phase transitions.

transitions--going from paraelectric to an intermediate surface-pinned ferroelectric state before switching to the bulk ferroelectric state. In an experiment these two transitions near the Curie temperature may appear as a gradual second order transition instead of two first order transitions depending on the film thickness. They also account for the decrease of the Curie temperature that is observed in the thin film form.

In this work, an apparent change to a second order phase transition in thin films of lead zirconate was observed. In addition, the transition temperature was also lowered compared to the bulk. Here, the order parameter is the degree of tetragonality of the crystal structure. However, this parameter is tied to the lead displacements which result in lead zirconate's dielectric behavior, and are the anti-ferroelectric equivalent of the polarization, P . The surface effects are strong enough to modify the dielectric behavior compared to the bulk.

7.2 Lead zirconate background

Lead zirconate is anti-ferroelectric below 230°C. Understanding lead zirconate, especially in thin film form, is important for future development of the technologically important materials based on solid solutions of lead zirconate and lead titanate (PZT). It is very difficult to grow single crystals of lead zirconate, so it is most often studied and used as a ceramic, powder or thin film. The bulk behavior and structure of PZ was first identified by Sawaguchi et al [7] who measured the first order anti-ferroelectric to paraelectric phase transition. The structure was studied via detailed x-ray and neutron measurements by Jona et al [8] and more recently by Tanaka et al [9] who assigned the space group $Pb\bar{m}$.

The basic structure of lead zirconate, or PZ, is pseudo-tetragonal and consists of Pb atoms on the perovskite cube corners, Zr atoms in the body center, and O atoms on the body faces. It belongs to the space group $Pb\bar{m}$ and is technically orthorhombic with $a = 4.153 \text{ \AA}$, $b = 4.156 \text{ \AA}$, and $c = 4.101 \text{ \AA}$ [10]. A pattern of alternating Pb displacements along the $\langle 110 \rangle$ directions gives PZ its anti-ferroelectric character (Figure 7.2) and the ab plane is defined as the plane containing these displacements. These displacements result in a unit cell that is four times larger than the conventional perovskite unit cell. The enlarged unit cell is depicted in the figure and it has the effect of adding superstructure peaks to the diffraction pattern. The shorter c -axis points out of the page. As temperature is increased past its Curie temperature (T_C) of 230°C, bulk PZ goes through a first-order phase

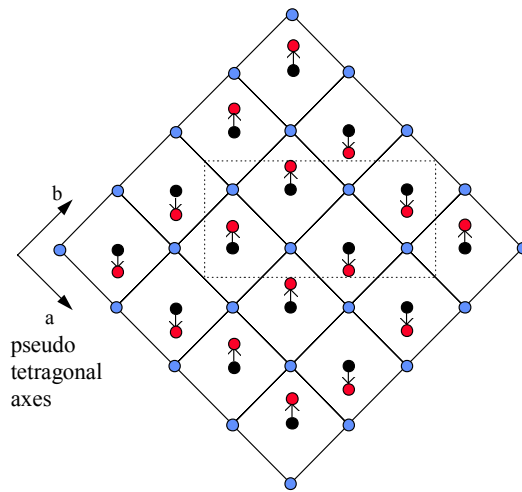


Figure 7.2. Lead zirconate structure. Zr atoms on the corners in the $z=0$ plane and Pb atoms in the centers in the $z = 0.5$ plane. The alternating Pb displacements along $\langle 110 \rangle$ directions make PZ an anti-ferroelectric and increase the unit cell by a factor of four.

transition to the paraelectric cubic state and the Pb displacements disappear. Also, a ferroelectric state can be induced below T_C through application of an electric field. These phase transformations cause strains to develop as the structure changes, and may lead to applications of PZ or related materials as thin-layer actuators.

In this experiment, x-ray diffraction and dielectric measurements were made on thin films of lead zirconate grown by T. Tani in the lab of D. A. Payne of the Department of Materials Science and Engineering [11]. Films were deposited on electroded silicon wafers using the sol gel, or chemical solution deposition, method. By controlling the growth conditions, both (100) and (111) preferred orientation films were grown. Thus, it was possible to study the differences in behavior of the two orientations as well as the differences between bulk PZ and thin film PZ.

7.3 Growth

The sol gel method is a relatively inexpensive and quick method for depositing thin films. More details on the growth of lead zirconate via sol gel can be found in [12]. In general, it involves starting materials of the metal cations dissolved in aqueous or organic solvents. For lead zirconate, the precursors were: $\text{Pb}(\text{Ac})_2 \cdot 3\text{H}_2\text{O}$ in $\text{CH}_3\text{OC}_2\text{H}_4\text{OH}$ and $\text{Zr}(\text{O-nPr})_4$ in $\text{CH}_3\text{OC}_2\text{H}_4\text{OH}$. These were mixed and then partially hydrolyzed to form inorganic polymers of the metal ions. Next, condensation polymerization turned these polymers into longer chains, and developed networks that “gel” together. The solution was then deposited onto the substrate by spin casting. A low temperature bake-out removed the organic components, and finally the film was crystallized by firing at 700°C for one to five minutes. A schematic depicting the growth process is in Figure 7.3.

By carefully controlling the substrate chemistry, both (100) and (111) preferred thin films were grown. A diagram of the substrate is shown in Figure 7.4. The silicon wafers were (100) oriented with a small oxide layer. A layer of titanium was then deposited to encourage adhesion of the platinum electrode layer. Approximately 2000 \AA of platinum were deposited and then heat treated at 400°C to increase the grain size of this polycrystalline layer. Preferential (111) orientation was achieved by depositing a thin layer of TiO_2 , so the entire substrate consisted of: $\text{TiO}_2/\text{Pt}/\text{Ti}/\text{SiO}_2/\text{Si}$. Formation of Pt_3Ti alloy encouraged growth of (111) domains because of the closer matching of the lattice constants. In contrast, self-textured growth of crystals with preferred (100) orientations

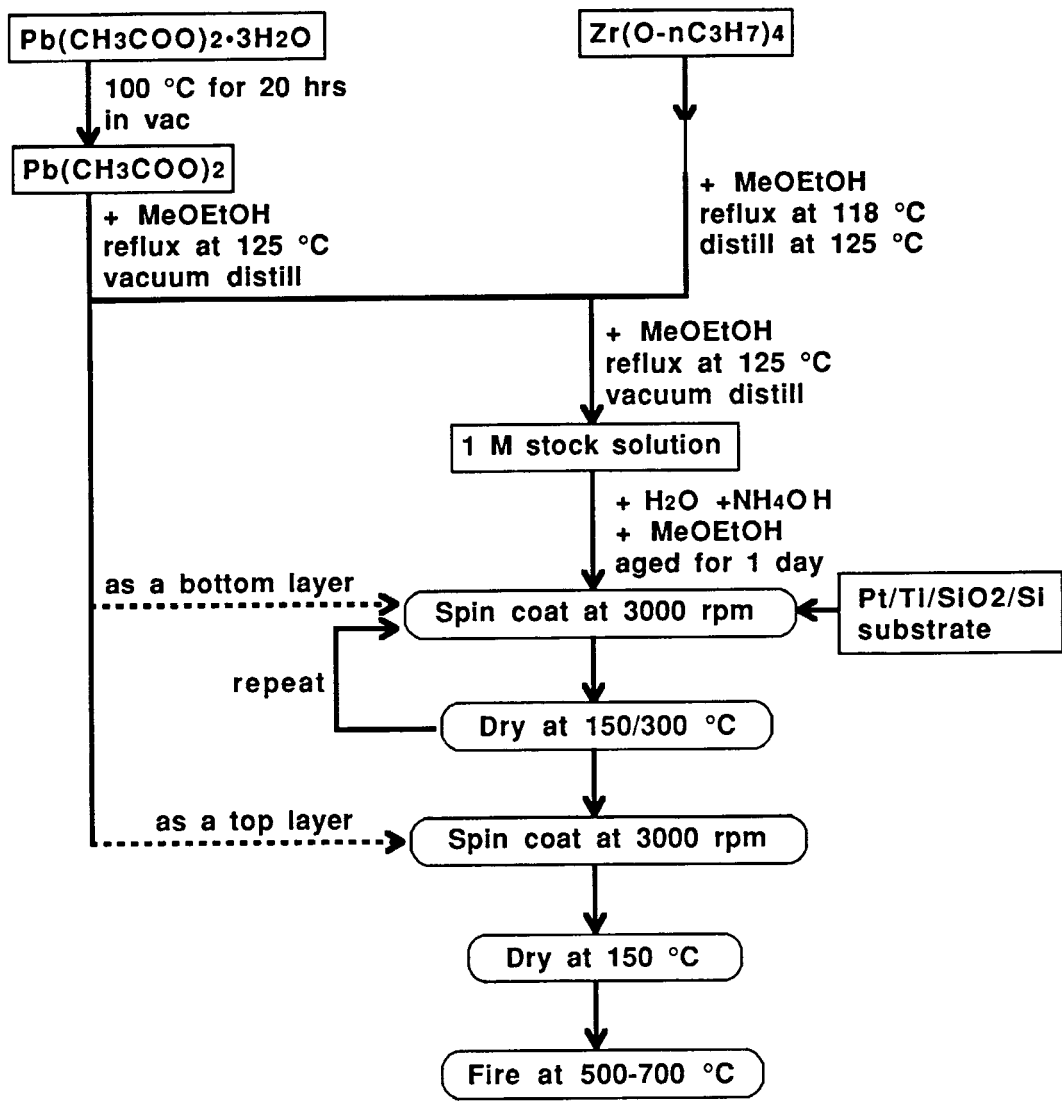


Figure 7.3. Procedure for depositing thin films via the chemical solution deposition, or sol-gel, method [11].

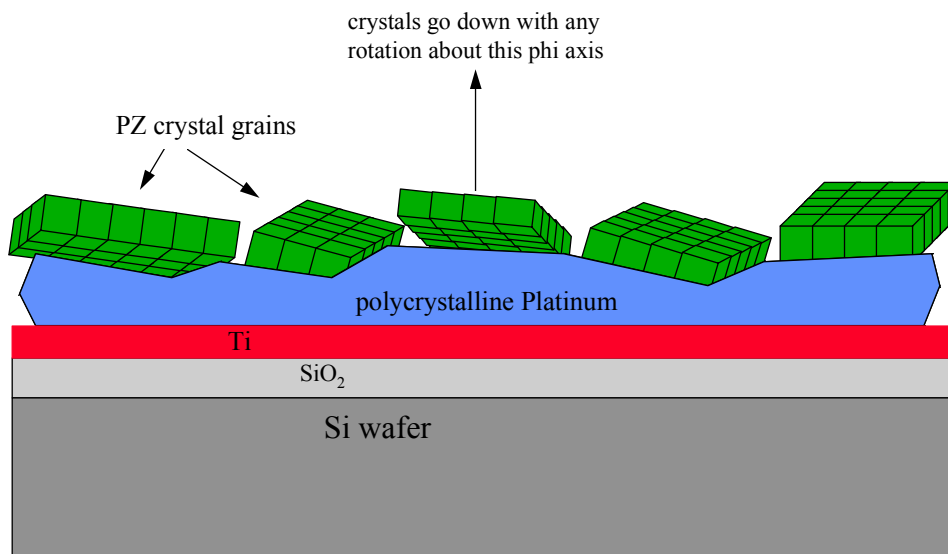


Figure 7.4. The substrates were platinized Si wafers. The (111) films also had a TiO₂ layer. The polycrystalline nature of the Pt electrode caused the film to break up into domains that could have any orientation about the phi axis.

was obtained on TiO₂ free surfaces, in accordance with minimum surface energy conditions for flat-faced surfaces [11]. Partially hydrolyzed lead zirconate solutions were deposited on the substrates by spin casting at 3000 rpm. Eight to ten layers of the PZ precursor solution were deposited for a total thickness of approximately 3300 Å. A final coating of PbO layer was added to prevent pyrochlore formation due to lead loss. Crystallization occurred by heating to 700°C for 1-5 minutes. Strong (111) oriented films were grown easily on the TiO₂ modified electrodes. In general, the (111) films had more uniform orientation than the (100) preferred films.

7.4 Dielectric and polarization measurements

Dielectric measurements were made using the set-up described in Chapter 4. Not only were the (111) films better oriented, but their dielectric properties and hysteresis curves were also more robust. The polarization versus electric field graphs (Figure 7.5) show higher maximum polarization for (111) films. This graph also demonstrates the field forced transition to the ferroelectric phase, as seen in the hysteresis loops that occur at large enough positive and negative applied field. The nearly straight line close to zero electric field demonstrates ferroelectric behavior and is similar to a normal dielectric. The fact that the loop is not completely closed suggests some grains are trapped in a ferroelectric state which may be due to the thin film nature of these samples. Also, the maximum in the saturation polarization of 40 $\mu\text{C}/\text{cm}^2$ for PZ (111) is just short of the bulk value of 43 $\mu\text{C}/\text{cm}^2$ [13]. The (100) oriented film had a maximum polarization of ~ 30 $\mu\text{C}/\text{cm}^2$.

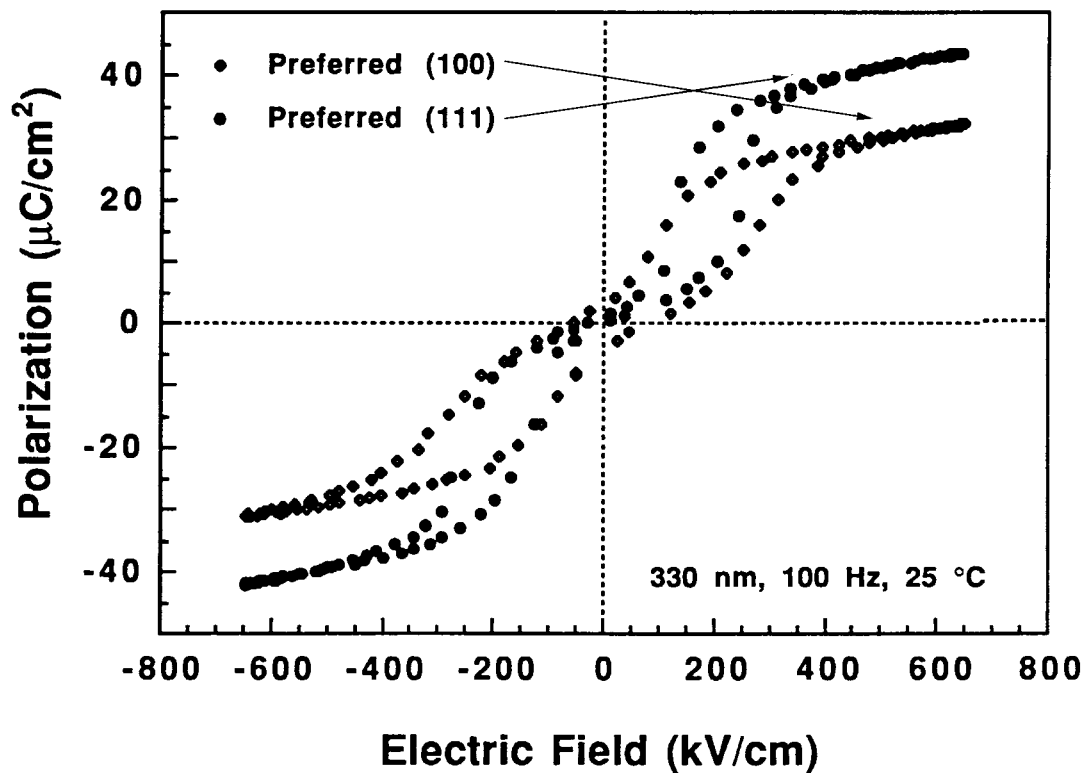


Figure 7.5. Polarization vs. electric field for preferred (100) and (111) thin films. The hysteresis loops are present at high fields where lead zirconate is forced into a ferroelectric state.

The dielectric measurements as a function of temperature are shown in Figure 7.6. Maxima occur at 225°C on heating and 220°C on cooling and the curve is similar to bulk behavior. However, the temperature of the maximum in dielectric constant is considerably less than the bulk value of 232° C [12] for both thin film orientations.

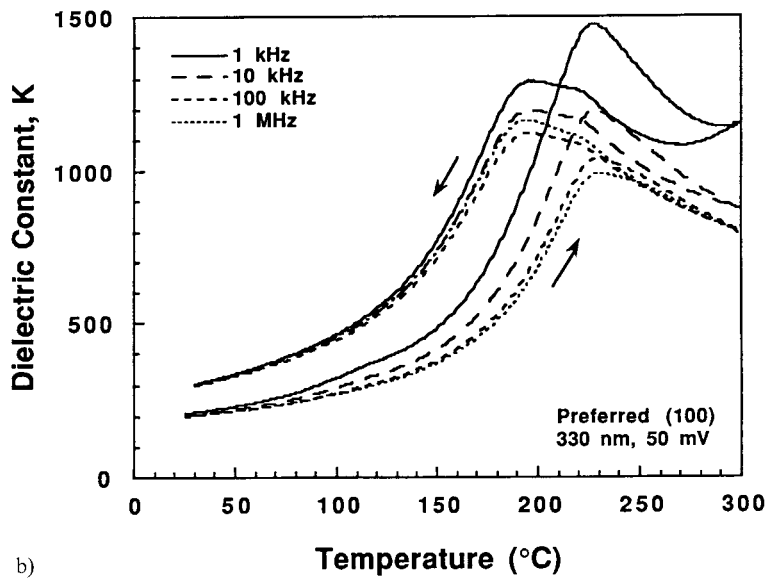
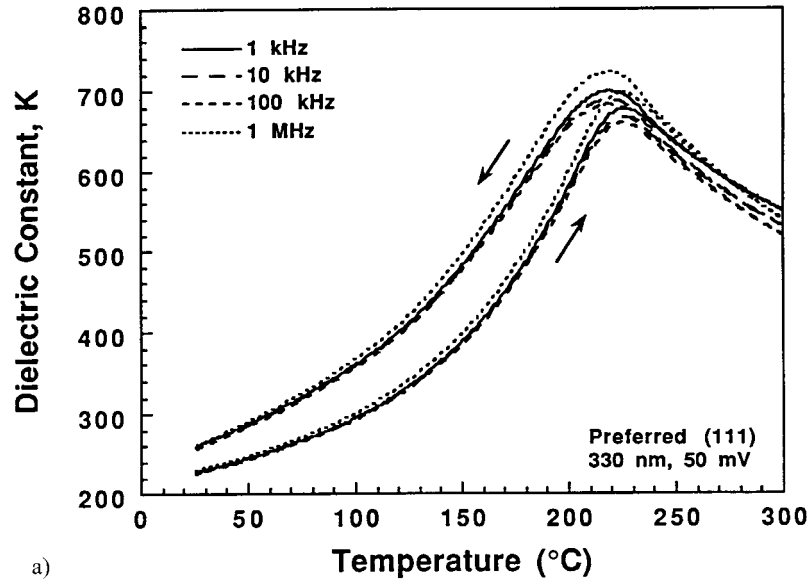


Figure 7.6. Dielectric constant behavior for the (111) and (100) lead zirconate films [11]. Compared to bulk PZ (Figure 3.6) the dielectric constant of the films is lower by a factor of 4 for the (111) film and a factor of 8 for the (100) film.

7.5 X-ray measurements

X-ray diffraction experiments were performed at Beamline X16C of the National Synchrotron Light Source. The incoming X-ray beam was tuned to 10.0 keV and focused onto the center of the lead zirconate film. The film was placed with its surface aligned perpendicular to the phi axis. For diffraction measurements, this direction was also defined as the Miller index l .

Because the PZ films were grown on polycrystalline platinum electrodes, the various grains were not completely aligned. The substrate allowed the thin films to attach with any orientation with respect to an axis perpendicular to the film (phi axis). This is a common result when using platinum electrodes and is known as “textured” growth. As a result, the crystallographic peaks lie in rings around the axis of the surface normal, and the diffraction pattern has “fiber texture”. That is, there is continuous intensity instead of a peak when rotating the crystal via the diffractometer’s phi axis. Figure 7.7 illustrates this effect for the superstructure reflections. Each grain is crystalline but has a different phi orientation. This lowers the number of degrees of freedom in the experiment and makes it harder to extract precise crystallographic information. It also has the effect of making some bulk reflections appear quite close to superstructure peaks. Nonetheless, crystallographic information can still be measured, and grains in a textured film are not completely randomized as in a powder sample. Instead of three-dimensional peaks, the diffraction pattern exhibited two-dimensional peaks in reciprocal space. Because of the fiber texture, off-specular reflections (those that result from planes that are closer to perpendicular to the surface) and the inherently weak superstructure reflections required

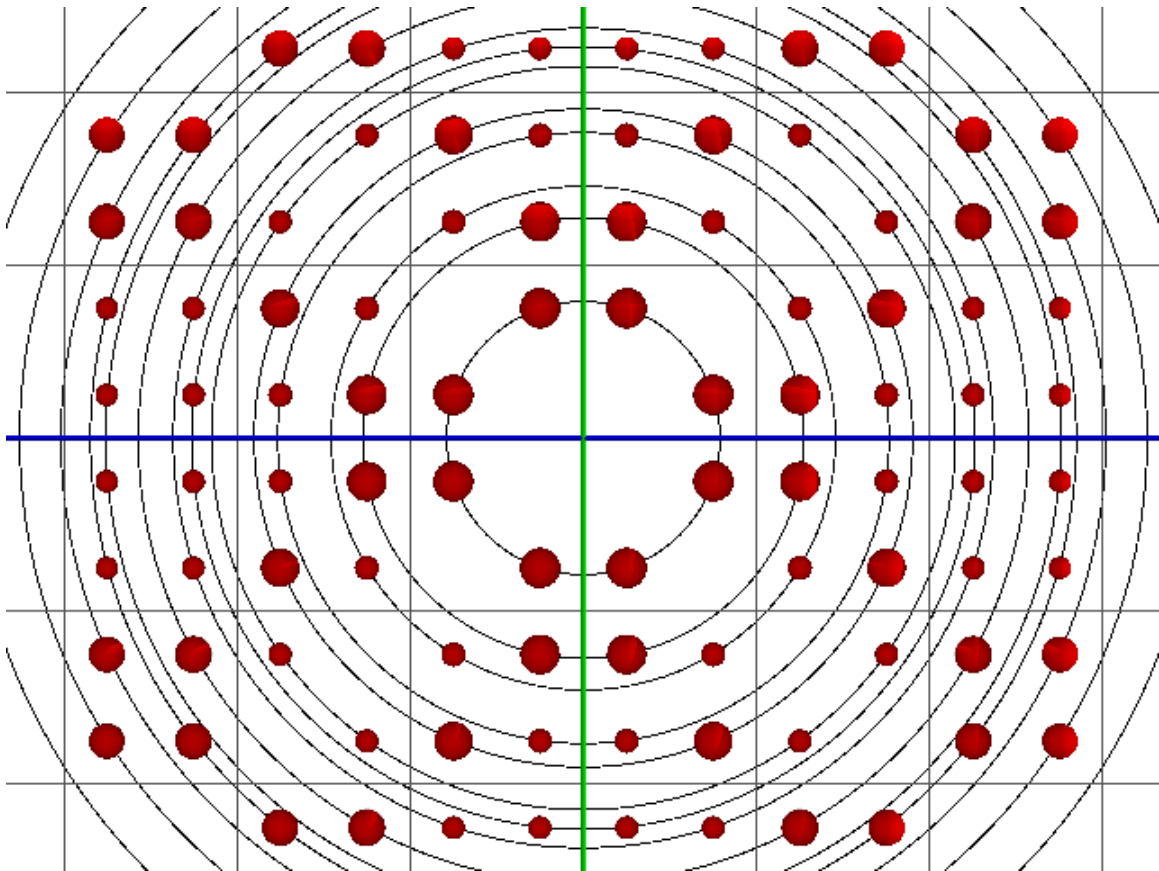


Figure 7.7. The superstructure diffraction peaks are shown as dots with radii proportional to magnitude. Due to the fiber texture, however, the peaks are smeared into rings of intensity in the hk diffraction plane (with $l=1$). Bulk peaks would be at the grid line intersections.

synchrotron radiation to get an appreciable signal. Peaks coming from diffraction planes in the same plane as the film were quite strong, as the phi orientation problem is not significant for these reflections.

To further complicate matters, the crystallized grains were also slightly tilted by varying amounts with respect to the surface of the film. This was due to the faceting and non-uniform surface of the polycrystalline Pt electrode. The jagged surface of the deposited Pt was made up of grains pointing in different directions. This caused the peaks to be broad in the transverse (chi) direction. Fortunately, the range of orientations was limited to about 10 degrees, so that peaks could still be identified. If this tilting extended all the way to 90 degrees, then the film would technically be a complete powder. This would have the adverse result of many peaks overlapping, and would limit the crystallographic information that could be extracted.

At least two bulk reflections were measured in order to orient the crystal in the diffractometer. Lattice constants were calibrated by measuring the very intense peak arising from the platinum electrode. Radial scans were used to determine lattice constants, tetragonal splitting, superstructure peak intensities and information on the size and shape of domains. For the temperature studies, an evacuated chamber was mounted on the diffractometer. This chamber had Kapton windows to allow the beam to enter and was pumped out using a roughing pump to allow for higher temperatures to be reached. A small cartridge heater of 1/8 inch diameter was mounted inside a specially designed sample holder. Using a thermocouple, the temperature was continuously recorded during each run. This configuration was capable of reaching temperatures of 235°C, so that the paraelectric cubic state could be obtained.

For the preferentially (100) oriented film, the films grew almost entirely with their c axis oriented perpendicular to the substrate. Since the tetragonal phase is almost cubic, this was best seen by measuring the difference between the (002) and (200) peak positions. The (200) reflection was grazing incidence and hence gave the lattice spacing of planes perpendicular to the film. The (002) was normal incidence and gave the spacing of planes parallel to the film. At room temperature, the c -axis (002) peak was found to be 4.114 Å and the a -axis (200) peak was 4.153 Å. In the (002) measurement, very little contribution at the (200) spacing was detected (and vice versa), indicating that most of the domains were oriented with their c axis perpendicular to the film, making it a (001) film based on the convention of defining Miller index l perpendicular to the film surface. The preferred c -axis direction was confirmed in superstructure peak measurements. Since the Pb displacements occur within a [110] plane, they produce superstructure peaks at the $(h+\frac{1}{4}, k+\frac{1}{4}, l)$ positions, where h , k and l are integers and can be permuted. The c -axis orientation of a particular domain defines which of h , k and l remains an integer. For example, with Pb displacements along the specific $\langle -1, 0, 1 \rangle$ direction, the superstructure peak would occur at $(h+\frac{1}{4}, k, l+\frac{1}{4})$. Reflections of the $(h+\frac{1}{4}, k+\frac{1}{4}, l)$ variety gave about 10 times the intensity of a $(h, k+\frac{1}{4}, l+\frac{1}{4})$ type peak, indicating again that the crystals mainly chose their c -axis perpendicular to the film.

For the films with their (111) axis perpendicular to the film, no preferred c -axis direction was observed. Contributions from the different domains caused reflections such as (200) and (002) to occur next to each other, resulting in a split peak (Figure 7.8). At room temperature, the lattice constants were: $a = 4.158$ Å and $c = 4.123$ Å. Compared to

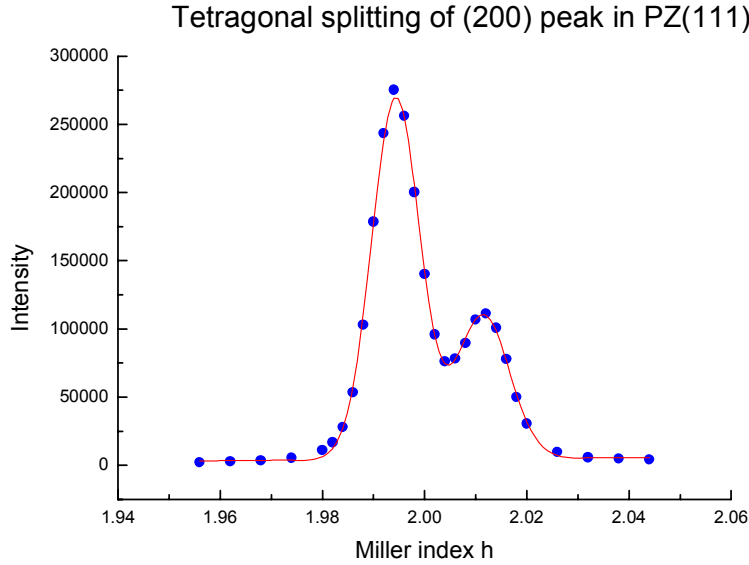


Figure 7.8. Raw data of the (200) peak scanned in the h direction showing the tetragonal splitting caused by the shorter c -axis lattice constant (right peak). Fit to two Lorentzians.

the bulk values, c is strained by 0.5%, which may also explain the large mosaic in the crystal structure.

By measuring the widths of both superstructure and bulk peaks, the respective domain sizes were estimated, again using the Scherrer formula. For the (111) film, the bulk domains were approximately 370 Å, while the superstructure domains were only about 220 Å. The (100) film had similar results with 400 Å for the bulk and 210 Å for the superstructure. The bulk domain size indicates that each separate sol gel layer completely crystallized into one domain (recall that ten layers were deposited for a total thickness of 3300 Å). The fact that the superstructure domains are approximately half as large as the bulk suggests that within each bulk domain, there is a single anti-phase boundary. Phase nucleation, where the Pb displacement direction is chosen, probably

occurred at the top and bottom surfaces of each grain, resulting in the superstructure domains that were half the size of the bulk domains.

The basic structure of these thin films and the size of the Pb displacements in the (111) film were determined by crystallographic analysis of several superstructure peaks. A value of 0.15(4) Å was found for the Pb displacement. The large error was due to the poor crystal quality of the films, but the result is in agreement with the study by Fujishita [14] which found 0.18 Å for bulk PZ.

7.6 Temperature measurements

The integrated intensity of the (0.25, 0.75, 1) superstructure peak was measured as a function of temperature for both types of film (Figure 7.9). Their intensities gradually diminished until disappearing at about 220°C in the (111) oriented films and 225°C in the (100) films. This is in contrast to the bulk crystal behavior where the phase transition is definitely first-order and occurs at 232°C on heating and 229°C on cooling [10]. At the level of temperature accuracy, the data do not show such a hysteresis, but the peak was slightly weaker and broader on the cooling cycle, suggesting a permanent rearrangement of anti-ferroelectric domains caused by annealing. It should be noted that the preparation conditions involved a single cycle of heating to 400° C and then a long rest period before these measurements were performed. It is interesting that the (100) preferred film shows a more gradual transition than the (111). In the dielectric studies [11], the (111) preferred

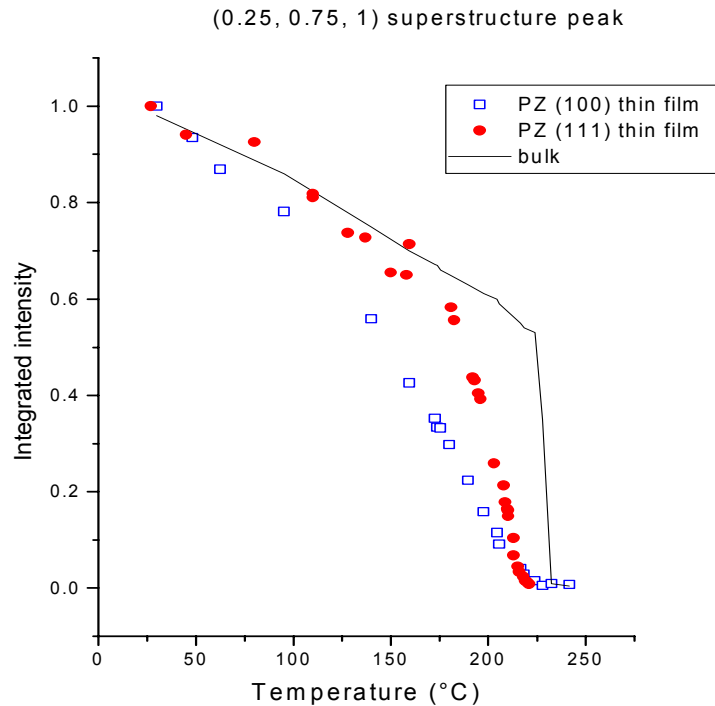


Figure 7.9. Integrated intensity of the (0.25, 0.75, 1) superstructure peak vs. temperature. In both thin films, the transition is much more gradual than the bulk first order phase transition taken from [14].

films were found to be of higher quality, or more bulk-like, with a 33% greater polarization saturation value.

The temperature dependence of the lattice constants, a and c , are shown in Figures 7.10 and 7.11 for the (100) and (111) films, respectively. Again the transition is not as sharp as the bulk data measured by Sawaguchi [10]. The data for the (111) preferred films were taken from the splitting of the (200) peak, while the data for the (100) were derived from the positions of the (200) and (002) peaks. The tetragonal splitting of the (111) data was fit to a power law:

$$I = I_0 \left(1 - \frac{T}{T_C} \right)^x$$

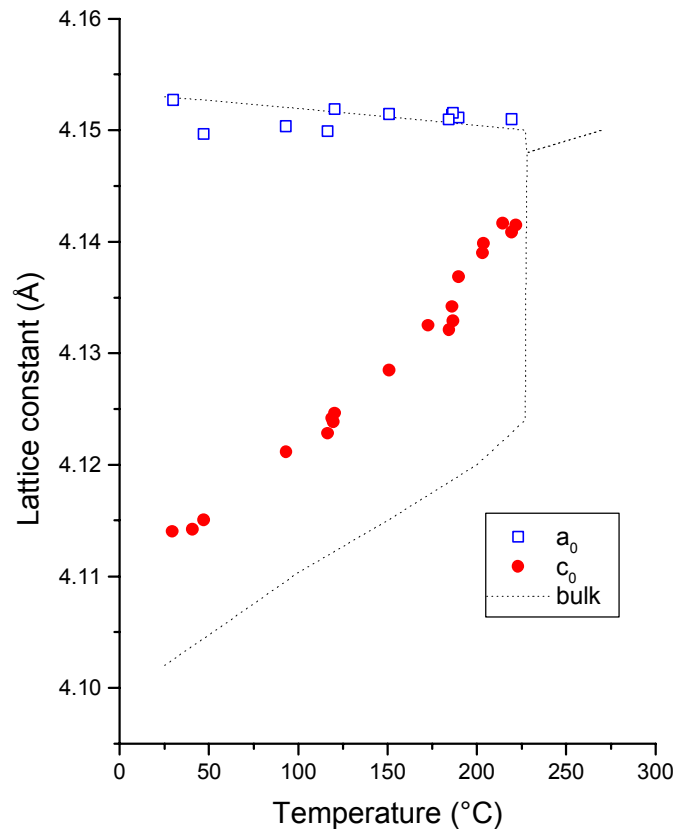


Figure 7.10. Dependence of a and c lattice constants vs. temperature for the (100) type lead zirconate films. The transition in the film is more gradual than the bulk behavior measured in [10].

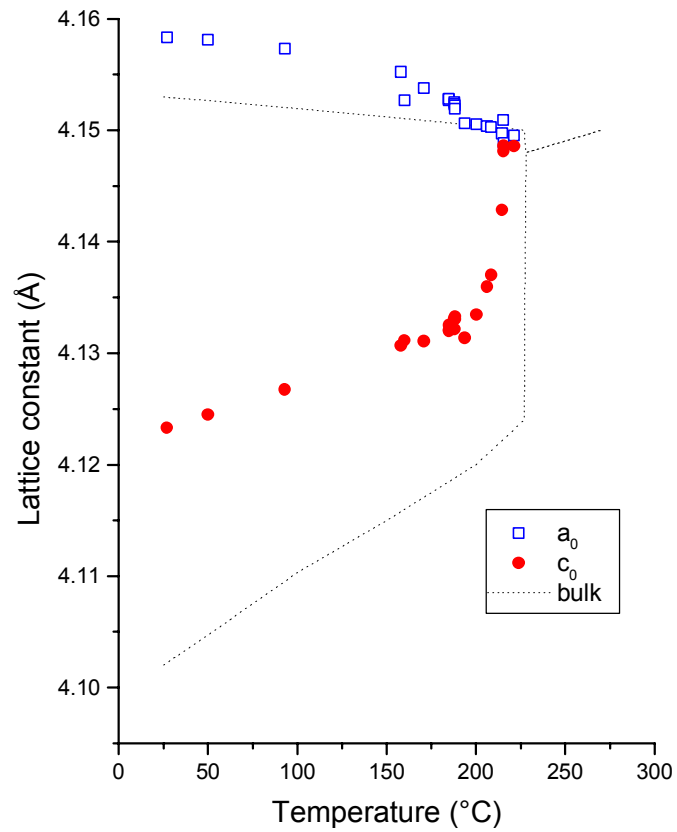


Figure 7.11. Dependence of a and c lattice constants vs. temperature for the (111) type lead zirconate films compared to bulk [10]. The (111) films had behavior closer to the bulk than the (100).

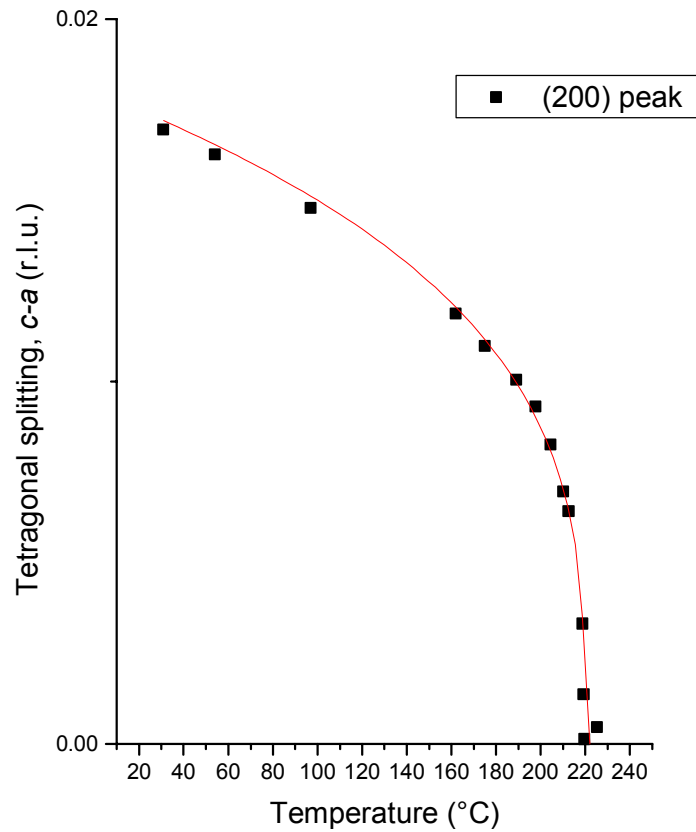


Figure 7.12. Tetragonal splitting in the (111) film vs. temperature fit to a power law.

resulting in an exponent $x = 0.30 \pm 0.03$ and Curie temperature of $220 \pm 1^\circ\text{C}$ (Figure 7.12).

The fit is not intended to represent agreement with critical behavior over such a large temperature, but is provided as a guide to the shape of the data. As seen in other ferroelectrics, the thin film form of lead zirconate reduced both the Curie temperature and maximum spontaneous polarization, in addition to the change in phase transition behavior from first to higher order.

7.7 Electric field

By sputter depositing a thin layer of gold on top of the lead zirconate film, electric field measurements were performed. The layer of gold was thin enough to still pass the x-rays and the lattice constant ensured that the gold peaks would not overlap with the platinum or PZ peaks. Electrodes were attached to the underlying Pt layer by scratching away part of the thin film. A very thin wire was carefully attached to the gold layer and connected to a high voltage power supply. Silver epoxy was used to secure both electrodes. The threshold voltage for field forcing the ferroelectric state was found to be 220 kV/cm in the polarization measurements. In the x-ray measurements, the field could not be controlled as easily, but a large enough field was applied to observe the transition from anti-ferroelectric to ferroelectric. This was determined by observing the disappearance of the 1/4-order superstructure peaks, and its re-appearance upon turning off the electric field.

7.8 Conclusion

The main result here is the clearly broadened phase transition behavior in thin films of lead zirconate. In the bulk there is a first order phase transition from cubic to tetragonal accompanied by the appearance of Pb displacements. Both measures of ordering were probed in these experiments: the intensity due to the anti-ferroelectric Pb displacements and the change in lattice parameters. It is conceivable that there are two phase transitions associated with two independent order parameters, although our data could not resolve a difference between the tetragonal splitting and superstructure transition temperatures.

The ability to control crystalline orientation on the same substrate is important for applications. It was observed that better lattice matching and reduced strain as in the (111) films led to improved dielectric properties. Also, the (111) films had domains with varying c axis direction as found in bulk PZ. The (100) films, in contrast, had preferred c -axis orientation and had lower dielectric behavior and a more gradual phase transition than the (111) films.

For thin films, in which the surfaces have an enhanced role, there is the possibility of a surface anti-ferroelectric state which may explain the change from a sharp to a gradual phase transition as seen in KNO_3 by Scott [5]. Alternatively, the more gradual phase transition in the thin film may simply be due to surface effects whereby the structure is modified over some depth from the surface; the distribution of film thickness (or grain sizes) naturally occurring in the preparation would just broaden the transition. Any structural phase transition whose order parameter couples to the lattice parameter is expected to have its behavior modified when attached to a substrate because of interfacial strain. The first-order bulk phase transition could be changed to higher order, or the phase transition singularity could be smeared out due to the finite size of the film.

7.9 References

- [1] K Binder, D P Landau, *Physica A*. **163** 17 (1990).
- [2] A M Glass, K Nassau, J W Shiever, *J. Appl. Phys.* **48** 5213 (1977).
- [3] K Binder, *Ferroelectrics* **35** 99 (1981).
- [4] R Kretschmer, K Binder, *Phys. Rev B*, **20**[3] 1065 (1979).
- [5] J F Scott, H M Duiker, P D Beale, B Pouligny, K Dimmler, M Parris, D Butler, S Eaton, *Physica B*. **150** 160 (1988).

- [6] E Rapoport, G C Kennedy, *J. Phys. Chem. Solids*, **26**, 1995 (1965), and J P Nolta, N W Schubring, R A Dork, *J. Chem. Phys.*, **42**, 508 (1965).
- [7] E Sawaguchi, H Maniwa, S Hoshino, *Phys. Rev.*, **83** 1078 (1951).
- [8] F Jona, G Shirane, F Mazzi, R Pepinsky, *Phys. Rev.*, **105** 849 (1957).
- [9] M Tanaka, R Saito, K Tsuzuki, *J. Phys. Soc. Jpn*, **51** 2635 (1982).
- [10] E Sawaguchi, *J. Phys. Soc. Jpn*, **8** [5], 615 (1953).
- [11] T Tani, Ph.D. thesis, University of Illinois at Urbana-Champaign, (1993).
- [12] T Tani, J Li, D Viehland, D Payne, *J. Appl. Phys.* **75** [6], 3017 (1994).
- [13] F Wang, K K Li and G H Haertling, *Optical Letters*, **17** [16], 1122 (1992).
- [14] H Fujishita, S Hoshino, *J. of Phys. Soc. of Japan*, **53** [1], 226 (1984).

Curriculum Vitae

David Michael Fanning was born in Chicago, Illinois on June 10, 1971, to the parents John and Margaret Fanning. He graduated Salutatorian from Marist Brothers High School of Chicago in 1989. Next, he enrolled at the Massachusetts Institute of Technology where he majored in physics and was fortunate to study under the guidance of Nobel laureate Jerome Friedman. His undergraduate thesis was titled “Light induced phase transitions in copolymer gels” with Prof. Toyochi Tanaka as thesis advisor. While an undergraduate, he was selected to participate in the Summer Institute in Applied Physics at Lawrence Livermore National Laboratory.

After receiving his B.S. degree in physics in May 1993, David worked at the National Institute for Standards and Technology in Maryland. Under Dr. John Gillaspay, he helped build the electron beam ion trap for atomic physics experiments.

At the University of Illinois, David served as a teaching assistant for introductory physics classes as well as Solid State Physics, and received the Excellence in Teaching Award. In January of 1995, he received his M.S. in physics. He then joined Prof. Ian Robinson’s x-ray diffraction research group and established collaborations with Profs. David Payne and Dwight Viehland in the Department of Materials Science and Engineering to investigate ferroelectric materials using x-ray diffraction. Single crystal

and thin film growth were carried out in Urbana, and x-ray measurements were performed at Brookhaven National Laboratory's National Synchrotron Light Source on Long Island.

After completing his Ph.D. in Physics in 1999, David joined the research and development group of Triquint Semiconductor in Dallas, Texas.

Selected publications:

D. M. Fanning, I. K. Robinson, X. Lu, D. A. Payne, **Superstructure ordering in lanthanum doped lead zinc niobate**, *Journal of Physics and Chemistry of Solids*, in press.

D. M. Fanning, I. K. Robinson, D. A. Payne, D. D. Viehland, S. Jung, E. Colla, **Superstructure ordering in lanthanum doped lead magnesium niobate**, *Journal of Applied Physics*, in press.

D. M. Fanning, I. K. Robinson, D. A. Payne, T. Tani, **Phase transitions in lead zirconate thin films**, *Ferroelectric Thin Films VII*, Ed. R. E. Jones, *Materials Research Society Proc.*, **541**, (1999).

A. I. Frenkel, D. M. Fanning, I.K. Robinson, J. O. Cross, **DAFS analysis of magnetite**, *Journal of Synchrotron Radiation*, **6**(Part 3), 332, (1999).

A. I. Frenkel, D. M. Fanning, I.K. Robinson, D. L. Adler, J. O. Cross, **DAFS study of local structure in ordered nanodomains in $\text{Pb}(\text{Mg}_{1/3}\text{Nb}_{2/3})\text{O}_3$** , "First-principles calculations for ferroelectrics", ed. R. E. Cohen, AIP (Woodbury, NY), 238 (1998).